PRIMARY COSMIC RAY ELECTRONS AND ALBEDO ELECTRONS IN 1967 AT ENERGIES BETWEEN 12 AND 1000 MEV

Thesis by

Martin Henry Israel

In Partial Fulfillment of the Requirements

For the Degree of

Doctor of Philosophy

California Institute of Technology

Pasadena, California

1969

(Submitted October 7 , 1968)

ACKNOWLEDGMENTS

I am most grateful to my faculty sponsor, Professor Rochus Vogt, who suggested this research project and offered valuable guidance and support throughout its execution.

It is my pleasure to acknowledge stimulating discussions with Dr. Klaus Beuermann, Professor Leverett Davis, Professor Edward Stone, and Mr. Carl Rice.

The success of the project depended upon the cooperation of numerous personnel of our laboratory. My sincere thanks go to Mr. William Althouse for essential electronic design in the early stages of this project, Mr. William Blodgett for design in the electronic system of the flight instrument, Mr. Carl Rice for valuable assistance in the construction of the detector system and its operation at Palestine, and Dr. Klaus Beuermann for assistance in the Palestine operation. Also, I greatly appreciate the efforts of Mr. Robert Cooper for aid in the construction of the flight system and its operation at Churchill, Mr. Michael Casteel for assistance in the Churchill operation and for writing computer programs used in the data analysis, and Mrs. Myrtle Casale, Messers. John Toomer, Richard Billingsley, and Alton Story for help in the construction of the electronic system.

Thanks are due to Professor Robert Walker for extending us the privilege of using the external electron beam of the Caltech Synchrotron where we calibrated our detector, and to the members of the synchrotron staff who aided us in the operation of the beam.

I also appreciate the skilled work by the personnel of the Bridge Laboratory Machine Shop under Mr. David Vail and the staff of Central Engineering Services.

In addition, I thank the members of the Office of Naval Research and the flight crew of Raven Industries who were responsible for the success of the balloon launch and instrument recovery operations at Fort Churchill, and the staff of the NCAR Balloon Flight Station who were similarly responsible in Palestine.

I am indebted to the National Science Foundation, the National Aeronautics and Space Administration, and the California Institute of Technology for financial aid during my graduate studies. The research described in this thesis was supported by the National Aeronautics and Space Administration under Grant NsG-426.

ABSTRACT

We measured the flux of cosmic ray electrons in a series of high altitude balloon flights. Balloons launched from Fort Churchill, Manitoba, on 17 June, 2 July, 9 July, and 21 July, 1967, floated near 2 g/cm^2 atmospheric depth; and one launched from Palestine, Texas on 7 April, 1967, floated near 5 g/cm^2. The detector system included a threshold gas Čerenkov counter, a digital spark chamber with lead plates, and scintillation counters.

During the flight of 9 July, the detector was pointed toward the nadir to observe the splash albedo. We present the resulting energy spectrum and also the return albedo spectrum observed in the April flight.

In the other three flights, we observed the diurnal variation near the polar cap of the flux of downward-moving electrons with energy $\lesssim$ 100 MeV. The nighttime flux is significantly lower than the splash albedo, while the daytime flux is in good agreement with the splash albedo. This comparison lends strong support to the model in which the low nighttime flux consists of primary electrons and atmospheric secondaries, while in the daytime the primaries are replaced by return albedo. We find that the nighttime geomagnetic cutoff near 68° geomagnetic latitude is below 17 MV, and the daytime cutoff is between 70 and 110 MV.

Making use of our analysis of the diurnal variation, we examine the primary electron spectrum. The observed flux of electrons with energy above the local geomagnetic cutoff and below 350 MeV is consistent with the expected flux of atmospheric secondaries; we derive 2σ upper limits to the primary electron flux of 20, 9,

and 13 electrons/m^2 sec sr in the intervals 17-57, 57-112, and 112-374 MeV respectively. We find 16 ± 14 electrons/m^2 sec sr between 374 and 1060 MeV. Comparison between the observed primary flux and the calculated flux of galactic secondary electrons indicates an absolute solar modulation of electrons below 100 MeV by at least a factor of three.

To Margaret

TABLE OF CONTENTS

LIST OF TABLES

LIST OF FIGURES

I. INTRODUCTION

Knowledge of the primary cosmic ray electron spectrum near the earth bears upon several astrophysical problems. It imposes limitations upon mechanisms of solar modulation of cosmic rays and provides information about the source of cosmic rays. Also, when coupled with observations of the non-thermal galactic radio noise, the observed electron spectrum furnishes information about the galactic magnetic field. In fact, the first evidence for the presence of cosmic ray electrons in the galaxy came from the interpretation in 1950 of the non-thermal radio noise as synchrotron radiation of extremely relativistic electrons in a galactic magnetic field (1).

The first direct observations of primary cosmic ray electrons were made ten years later, in 1960, by Meyer and Vogt (2) and by Earl (3). They detected electrons in the energy ranges of 100 to 1000 MeV and of 500 to 3500 MeV, respectively, but derived only crude spectral information. Since then, the electron spectrum from 200 MeV to 300 GeV has been extensively investigated (4-10). (For a summary of earlier work see reference 11.) Also electrons from 3 to 12 MeV have been observed for several years (12) (13).

In this thesis we present measurements of the electron spectrum between 17 and 1000 MeV. Other observations at the low end of this energy interval, below 200 MeV, have been published only within the past year; and there is wide variation among the results of the various authors (14) (15) (16). Study of these low-energy electrons has bearing upon several astrophysical and geophysical problems.

One question of astrophysical interest is the origin of cosmic rays. For cosmic ray electrons, one source is the collision of cosmic ray protons and alpha particles with nuclei of the interstellar

gas. Such collisions can produce charged pi mesons which in turn produce electrons by $\pi \rightarrow \mu \rightarrow e$ decay. In addition, cosmic ray electrons may be produced by acceleration of electrons from the ambient matter, perhaps in the same sources where cosmic ray nuclei are accelerated.

The electron flux which has been observed at higher energies, above 400 MeV, is significantly larger than the flux expected from the collision source (17) (18) (19); and the small positron/electron ratio observed between 500 MeV and 5 GeV gives further evidence for the dominance of primary electron acceleration at these higher energies (20) (21). In contrast, our results for the low-energy primary electron spectrum, when compared with calculations of the spectrum of collision-source electrons (22), indicate that the collision source may be dominant at energies < 400 MeV.

An additional problem in the study of cosmic rays is the solar modulation of the interstellar cosmic ray spectrum. A cyclical variation in the intensity of cosmic ray nuclei, correlated with the eleven-year solar cycle, has been well established. (A current review of solar modulation is given by Webber [23].) Even at the minimum of solar activity, when the cosmic ray flux is highest, there is a radial gradient of cosmic rays within the solar system, indicating that the flux observed at the earth is always lower than the interstellar flux (24). The residual modulation, which is present at solar minimum, has been estimated for electrons with energy $\gtrsim$ 200 MeV by comparing the observed electron flux with the 10 to 400 MHz non-thermal galactic radio emission (25) (26) (27). At lower energies this comparison is complicated by interstellar absorption of galactic radio noise below 10 MHz. The residual modulation for deuterium and helium-3 with rigidity above 500 MV has also been estimated, by

comparing the observed spectra of these nuclei with spectra calculated assuming that they originate in interactions between cosmic ray nuclei and the interstellar gas (28).

Our results for the low-energy primary electron flux near the earth fall below those of the calculated flux of collision-source electrons in the galaxy. This enables us to place a lower limit upon the residual solar modulation at these lower energies.

In addition to information about the primary cosmic rays, observations of the low-energy electrons provide information about some gross properties of the geomagnetic field. A diurnal variation in the flux of electrons below 220 MeV, near the polar cap, was reported by Jokipii, L'Heureux, and Meyer (29), who attributed it to a diurnal variation in the geomagnetic cutoff resulting from the magnetospheric tail on the night side of the earth. This cutoff variation has also been studied with 1 MeV protons observed on polar orbiting satellites (30) (31). Measurements of electrons have an advantage over those of protons for studying these cutoffs at low rigidity. The cutoff at 20 MV can be observed with 20 MeV electrons, but protons of the same rigidity have energy of only 0.2 MeV and are much more difficult to detect.

We shall present results of several observations of the diurnal electron flux variation. Our data have better energy resolution than the results published by Jokipii et al., and include a measurement of the flux transition in the early evening, which they were unable to observe.

In addition to electrons incident from the zenith, we also observed upward-moving splash albedo electrons. We show in Chapter V that the results of this observation give strong support for the proposed model of the diurnal variation of low-energy electrons. Inde-

pendent knowledge of the splash albedo spectrum is also useful for experiments in which the albedo cannot be directly distinguished from downward-moving primaries (for example, reference 32). We shall present an energy spectrum of the splash albedo between 12 and 1000 MeV.

The data described in this thesis were derived primarily from four high-altitude balloon flights of a detector system designed and constructed in our laboratory. These flights were launched from Fort Churchill, Manitoba, during Summer, 1967.

II. INSTRUMENT

A) Background

We were interested in designing a directional detector system capable of detecting individual electrons and measuring their energy over a wide energy interval. Earlier experiments had shown that only a small fraction of the cosmic rays are electrons. The flux of electrons with energy greater than 300 MeV is less than 4 percent of the proton flux above that energy and less than 30 percent of the alpha particle flux. We therefore required a system which could reliably distinguish electrons from the other cosmic rays, and could also register a sufficient number of events during a balloon flight to enable us to determine an energy spectrum.

The cloud chamber of Earl (3) allowed unambiguous identification of energetic electrons by viewing the cascade showers which the electrons produced. However, because the chamber was expanded randomly, the results suffered from poor statistics. Only eleven electrons were observed in a twelve-hour flight. Nuclear emulsions also offer unambiguous identification of electrons, but they too, generally suffer from poor statistics because of the difficulties associated with scanning large areas of emulsion for tracks of minimum ionizing particles (33).

Counter techniques permit registration of many more events than either cloud chambers or emulsions. The earliest electron observation using counters, that of Meyer and Vogt (2), identified electrons as particles giving minimum energy loss in a scintillation counter, and having range in lead much shorter than that of minimum ionizing protons. One difficulty with this technique is that protons

with energy $\gtrsim$ 500 MeV gave ionization loss which could not be resolved from minimum ionization; these protons could suffer a nuclear interaction in the lead and show a short range, characteristic of an electron.

Our experiment utilizes particle counters and a spark chamber to combine the better statistics afforded by counter techniques with track visualization capability. We use the high velocity threshold of a gas Čerenkov counter to eliminate most of the cosmic ray protons. A narrow gap spark chamber, with lead plates between gaps, detects shower development of energetic electrons or measures the short range of electrons of lower energy.

Other detectors of cosmic ray electrons have also used a combination of a gas Čerenkov counter and a device for detecting electron showers (4) (6). In those experiments, the shower detector was a lead-glass Čerenkov counter. We decided to use a spark chamber because the track visualization is useful for distinguishing electrons from protons, and also because we were interested in developing digital spark chamber techniques in our laboratory for use in other experiments with balloon and satellite-borne detectors.

B) Detector system

1) Overall description

Figure 1 shows a cross-section of our detector system. A triple coincidence of Telescope Counter 1 (T1), Telescope Counter 2 (T2), and the Gas Čerenkov Counter (C), triggers the electronic system which records the event. The scintillation counters, T1 and T2 define an acceptance cone with a geometrical factor of 0.90 ± 0.02 cm^2 sr. The maximum opening angle is 13.2^{o} from the axis.

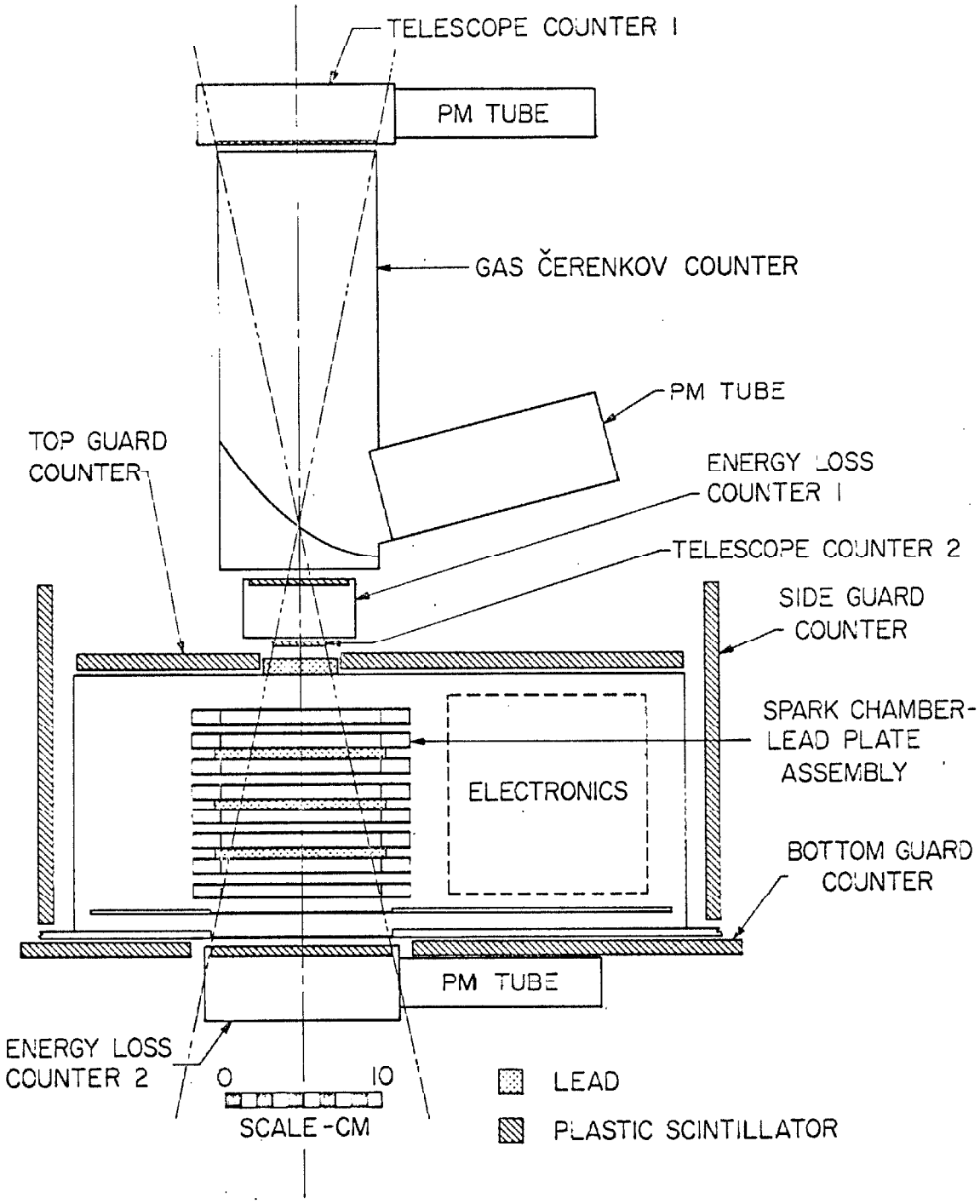

Fig. 1 Cross-section of the detector system.

The Čerenkov counter is filled with sulfur hexafluoride at 2.2 atmospheres absolute pressure (at 25°C). The index of refraction of the gas under these conditions is 1.00157 (34). This gives our counter a velocity threshold of 0.9984 c, which corresponds to a kinetic energy of 8.6 MeV for electrons and 15.8 GeV for protons.

The pulse heights from the scintillation counters Energy Loss 1 and Energy Loss 2 (ΔE1 and ΔE2) are recorded for each event. Pulse height in ΔE1 corresponding to minimum energy-loss establishes that one, singly charged particle traversed the telescope. This low energy-loss also verifies that the particle was relativistic, although it does not set as high a velocity threshold as that of the Čerenkov counter. The counter ΔE2 samples the electron shower independently of the spark chamber.

A high voltage pulse is applied to the spark chamber plates at each T1, T2, C triple coincidence, and the position of each spark is recorded digitally. A lead plate with a thickness of 11.6 g/cm^2 (2 radiation lengths) is above the chamber, and three lead plates, each 5.8 g/cm^2 thick, are inside the chamber; a pair of chamber gaps is below each lead plate.

The chamber shows no sparks for electrons stopping in the first lead plate, indicating their short range. For more energetic electrons, the chamber indicates the development of their cascade shower. These electrons can be distinguished from the protons which penetrate the lead without a nuclear interaction, because the latter leave a single straight track in the spark chamber.

Most protons which do interact in the detector are eliminated by the guard counters. These counters completely surround the chamber, except for apertures for the allowed particle beam. For each event we record whether a guard counter is triggered in coinci-

dence with the telescope counter. An interacting 16 GeV proton has greater than 90 percent probability of sending at least one charged particle through a guard counter. The guard counters also allow us to eliminate charged particles which enter the detector from outside the acceptance cone, but give a triple coincidence by interacting in the lead and sending particles up through the telescope counters.

The detector system configuration described above is the normal one. We used this in all but one flight. For this particular flight we made two modifications. First, we changed the coincidence requirement for triggering the electronics from a T1, T2, C triple coincidence to a T1, T2 double coincidence. However, we did record the output of the triple coincidence circuit. Second, we added four, 5.8 g/cm^2 lead plates to the spark chamber. We placed these in the four spaces between chamber gaps where the normal configuration had no lead. By triggering the electronics on double coincidences, we were able to record low-energy protons and alpha particles which stopped or interacted in the spark chamber. The added lead extended the energy range for which these particles stop in the chamber. In this thesis we concern ourselves with electrons, and so consider only triple coincidence events, except where otherwise noted.

We measure the atmospheric pressure at the detector during flight with a Wallace-Tiernan aneroid barometer (FA160). Every five minutes a 16 mm camera photographs the barometer, a clock, and a thermometer. Calibration of the barometer before and after the flights was reproducible within $\pm$ 0.1 mb at 2 mb, the minimum pressure during the flight.

The entire instrument, with the exception of the photobarograph and the silver-zinc batteries, is enclosed in an aluminum gondola, which is pressurized at one atmosphere. A 0.016-inch

aluminum window above the detector system allows the cosmic rays to penetrate the gondola with a minimum of scattering. The flight equipment has a total weight of 290 pounds.

2) Scintillation counters

All scintillators are NE 102 plastic (Nuclear Enterprises Ltd., Winnipeg, Manitoba) and are viewed with EMI 9524B photomultipliers (Whittaker Corp., Plainview, N. Y.). The dimensions of the scintillators are summarized in Table 1. For counters T1, ΔE1, and ΔE2, the light coupling from the scintillator to the photomultiplier is a hollow chamber painted white inside (Dupont high reflectance white paint, 29-915). The top and bottom walls of these light chambers are 0.010-inch aluminum to minimize scattering and energy loss of the particles. ΔE1 and ΔE2 have resolution of 35 percent and 40 percent respectively, full width at half maximum, for minimum ionizing muons. T1 has 50 percent resolution. T2 is connected to its photomultiplier by a lucite light-pipe which views the scintillator edge-on; its resolution is 35 percent.

The photomultiplier of each guard counter is coupled directly to the large flat side of the scintillator with a thin layer of optical grease (Dow Corning 20-057). With this light coupling technique, the amount of light collected by the photomultiplier varies as much as a factor of two with the location of the particle track in the scintillator. This variation is acceptable because a minimum ionizing particle anywhere in the scintillator gives sufficient light at the photomultiplier to trigger the counter, and the guard counter is used only for coincidence purposes without pulse height analysis.

TABLE 1

SCINTILLATION COUNTERS

Designation	Function	Dimensions (inches)	Connection to photomultiplier
T1	Telescope 1	1/16 x 4 diam.	Air; white chamber
T2	Telescope 2	1/8 x 1.34 x 1.34	Lucite light pipe
ΔE1	Energy Loss 1	1/8 x 2 1/2 diam.	Same as T1
ΔE2	Energy Loss 2	1/4 x 4 1/2 x 4 1/2	Same as T1
Top 1	Top Guard	3/8 x 15 1/8 x 15 1/8[a] with hole 2 x 2	Direct coupling of photomultiplier to scintillator for all guard counters.
Top 2			
Side 1	Side Guard	3/8 x 16 5/8 x 11 1/2	
Side 2		3/8 x 16 5/8 x 8 1/2	
Side 3		3/8 x 16 5/8 x 8 1/2	
Side 4		3/8 x 16 5/8 x 8 1/2	
Bot 1	Bottom Guard	3/8 x 14 7/8 x 18 with hole 5 1/2 x 5 1/2[a]	
Bot 2			

[a] Dimensions are for entire top guard or bottom guard; each consists of two triangular pieces.

3) Gas Čerenkov counter

The sulfur hexafluoride Čerenkov radiator is contained by an aluminum tube of four-inch inner diameter and 10 1/2-inch length. The ends are 0.012-inch aluminum to minimize scattering and energy loss of the particles. The photomultiplier is mounted outside the particle beam to reduce the amount of material in the beam and to eliminate the possibility of producing Čerenkov light as a particle penetrates its quartz window.

The Čerenkov light from the SF_6 is directed onto the face of the photomultiplier by a parabolic mirror in the particle beam. The mirror is 1/8-inch thick Lucite with its upper surface polished and aluminized. Čerenkov light is emitted at an angle θ with respect to the particle trajectory given by (35)

$$\cos \theta = \frac{1}{\beta n} \qquad (1)$$

where β is the particle velocity in units of the speed of light, and n is the index of refraction of the medium. For SF_6 at 2.2 atmospheres, the maximum value for θ is 3.2°. The acceptance cone defined by the telescope counters, T1 and T2, is designed so that all Čerenkov light emitted by a particle whose trajectory is within the cone will fall directly onto the mirror.

The photomultiplier is a low-noise EMI 6255S. This tube has a quartz window, rather than the standard lime soda glass, thereby extending its ultraviolet response from 0.35 micron to 0.17 micron. We thus make use of the strong Čerenkov emission at short wavelengths. The window of the photomultiplier is in direct contact with the SF_6 for maximum light collection.

The detection efficiency of the counter for singly charged particles with β very near one is 96.0 ± 0.2 percent. We measured this with 200 to 1000 MeV electrons from the Caltech synchrotron. This efficiency was independent of the angle of incidence of the electrons within the acceptance cone.

Throughout all flights, the Čerenkov counter noise rate registered less than 100 pulses/sec. The resolving time of the T1, T2, C triple coincidence circuit is 1 μsec, so the probability of an accidental Čerenkov signal accompanying a T1, T2 double coincidence was less than 10^{-4}. A more significant source of false triple coincidences is Čerenkov light emitted from the Lucite mirror. The aluminized front surface of the mirror shields the photomultiplier from this light source; however, this surface does transmit 0.5 percent of incident light. Tests with the counter evacuated show that 0.7 ± 0.2 percent of muons with $\beta \gtrsim 0.9$ produce a false triple coincidence. The false Čerenkov signals produce a contamination of less than 5 percent in the electron measurement. (See page 50.) This problem could be avoided in the future by using an opaque plastic, rather than lucite as the mirror backing, or by constructing the mirror from a sheet of aluminum.

4) Spark chamber

Below the telescope counters and the first lead plate is an eight-gap, digital spark chamber. The digital read-out offers several advantages over conventional photographic read-out. The most obvious is the opportunity for rapid, computerized data analysis, without manual film scanning and measuring. Also, it eliminates the need for carefully aligned optics and the danger that these optics be jarred from their positions during a rough balloon launch. Furthermore, the digital read-out allows us to completely enclose the spark

chambers in an aluminum box which contains the spark noise. This box enables us to operate pulse height analyzers, discriminators, and other sensitive circuits without spark interference. In addition, digital chambers are potentially useful for satellite-borne experiments.

The chamber read-out is digitized with ferrite memory cores. The ground plane of each gap consists of ninety-six parallel conductor strips. Each strip extends out of the gap and connects to a wire which passes through a memory core before being connected to ground. There is one core for each strip. When a spark strikes a strip, the spark current passes through the core and reverses the magnetization direction of the core. After the spark noise dies away, the cores are interrogated and reset to their normal state. The cores set by spark current indicate the positions of the sparks. In our chamber, alternate gaps have ground strips oriented at right angles to one another. We thus have two orthogonal views of each event, with four gaps contributing to each view.

Each gap of the chamber is a self-contained module consisting of a high voltage plane, Lucite spacer, ground plane, and core board (Fig. 2). The planes and spacer together form an enclosure for the chamber gas. The gas is standard "spark chamber neon," a mixture of 90 percent neon and 10 percent helium. The gap width is 1/4 inch, and the sensitive area of each gap is 4 inches square.

The ninety-six conductors of the ground plane are strips of copper 0.02 inch wide on 1/16-inch glass-epoxy board. The strips are uniformly spaced, 24 per inch. They are etched on the copper-clad epoxy board by standard printed circuit techniques. A half-inch wide grounded copper guard strip, adjacent to the outermost wire on each side, extends over the inner edge of the Lucite spacer. The

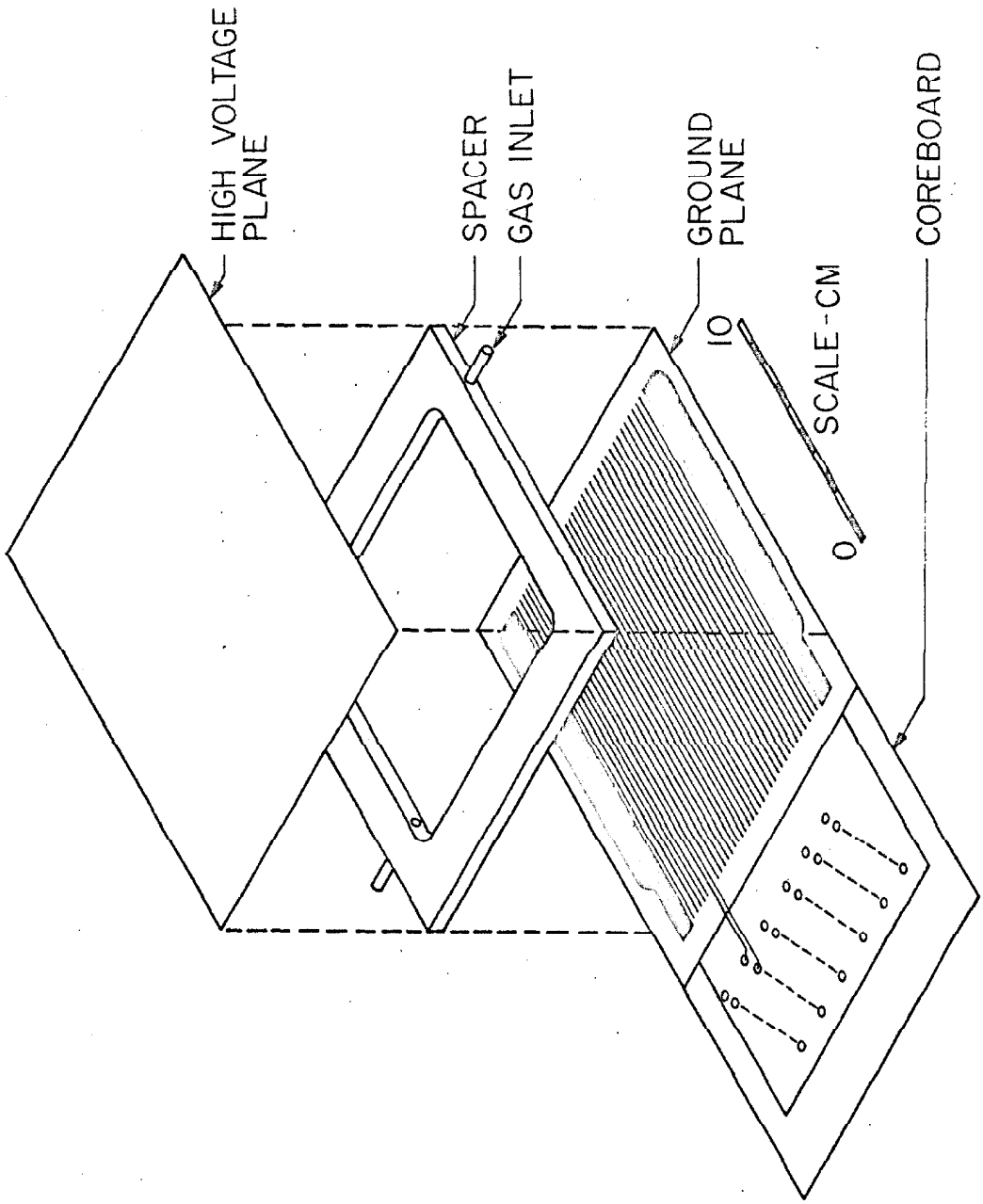

Fig. 2 Exploded view of one chamber module.

addition of these guard strips makes the electric field inside the chamber more uniform and prevents spurious sparks at the edge of the chamber.

The high voltage plane is a sheet of 1/16-inch aluminum covered on the inside with a 0.015-inch layer of nylon. The most important effect of the nylon is the reduction of spark spreading. With the nylon covering the aluminum, approximately 90 percent of all sparks set only one core, and the remaining 10 percent set two adjacent cores. Fewer than 0.1 percent set three adjacent cores. This enables us to resolve two sparks 0.08 inch apart. The nylon provides the only reliable operating conditions known to us for which fewer than 10 percent of the sparks set three adjacent cores.

Because of continuous contamination of the chamber gas from the nylon and the epoxy board, it is necessary to flow gas continually through the chambers. A small gas cylinder, inside the gondola, supplies sufficient gas for 30 hours at a flow rate of 2 ml/sec. To prevent a buildup of pressure in the sealed gondola, the gas is vented to the outside through a 14.7 lb/in^2 pressure relief valve.

Tests in the laboratory with relativistic muons show a typical efficiency of 94 to 97 percent for detecting a single charged particle in any given gap. On approximately 5 percent of the events in each gap, a spurious spark at a random chamber position accompanies a good spark.

C) Electronic System

1) Overall description

After each event, two types of data are recorded digitally on magnetic tape.

(1) Data describing this event.

   (a) Pulse heights from ΔE1 and ΔE2.

   (b) One bit indicating a T1, T2, C triple coincidence.

   (c) Three guard bits; one indicating output from the top guard counter; another indicating any of the side guards; the third for the bottom guard.

   (d) The position of each spark in the chamber.

(2) Related information.

   (a) Accumulated count of single pulses from the guard counters.

   (b) Accumulated count of single pulses from the Čerenkov counter.

   (c) Accumulated count of T1, T2 double coincidences.

   (d) Temperature.

   (e) Time.

Figure 3 is a general block diagram of the electronic system. A triple coincidence among T1, T2, and C triggers the high voltage pulser, which applies 8 kV to the spark chamber. The primary coincidence also activates the control logic and produces one of the inputs to the guard coincidence logic. The busy signal from the control logic blocks the coincidence, preventing any further events from triggering the system until this event has been recorded on the magnetic tape. The control logic also opens the linear gate on the input of each pulse height analyzer, permitting the analysis of the ΔE1 and ΔE2 outputs. Then the control transfers all the data except the

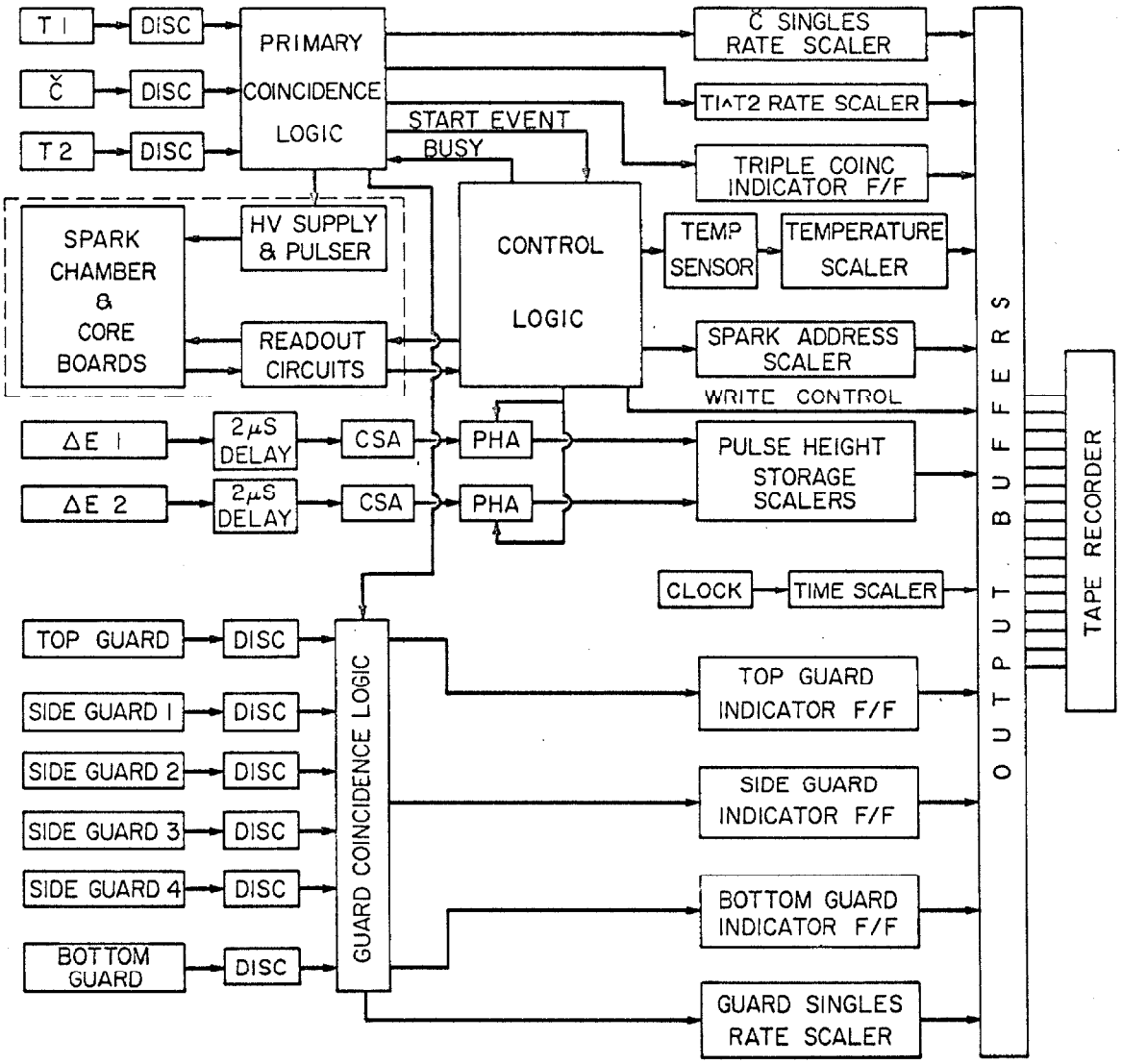

Fig. 3. Electronic block diagram.

DISC = Discriminator

CSA = Charge sensitive amplifier

PHA = Pulse height analyzer

Dashed line indicates components enclosed by the spark noise shield.

spark information through the output buffers onto the magnetic tape. Finally it interrogates the cores and writes the position of each spark onto the tape.

The data are grouped on the magnetic tape into "words" of ninety-six bits, six bits in each of sixteen channels. Two or more such words are used to record each event, the number of words depending upon the number of sparks to be recorded. Most events require two or three words. The "dead time" during which the detector is prevented from recording further events is determined primarily by the time required to write these words on the tape. Each word takes 288 ms; so the minimum dead time associated with writing each event is 576 ms. An additional 9 ms is introduced by the time necessary to interrogate the cores.

During flight the tape recorder runs continuously at 10 inches per minute. It holds approximately 30 hours of tape. During tests of the equipment on the ground the data are recorded on punched paper tape in parallel with, or instead of, the magnetic tape. The paper tape is easily read manually, providing immediate information about the detector operation; or it can be submitted to the 7094 computer for further analysis.

The total power consumption is six watts, provided mainly by eighteen Yardney silver-zinc batteries supplying various voltages up to +28 V. A quarter watt required at -6 V and +35 V is supplied by small nickel-cadmium batteries. The high voltages required by the photomultipliers and the spark chambers are produced by dc-dc converters which operate from the battery power.

2) High voltage pulse

The high voltage pulse is applied to the spark chamber by two sealed spark gaps GP17A (E.G. & G. Inc., Salem, Mass); each spark gap drives four of the chamber modules (Fig. 4). Each chamber module (CM) has its own 1000 pf coupling capacitor. The resistor R determines the decay time constant of the applied pulse. The value of R is adjusted for each module. Too low a value of R results in decreased detection efficiency, while too high a value results in spurious sparks accompanying good sparks. The optimum value of R for various modules is between 200 and 300 ohms. Variations of ± 10 percent from the optimum produce insignificant change in the operation of the chamber.

The GP17A spark gaps are triggered by a 5 kV pulse from a krytron, which is in turn triggered by an avalanche transistor and pulse transformer. This circuitry is essentially the same as that of commercially available high voltage pulsers (such as the HV100 of E.G. & G. Inc.). The electronic delay from the output of the photomultipliers to the appearance of the high voltage on the spark chamber is 140 ± 20 nsec. The variation is due to change in the delay of the GP17A during its life. The rise time (10 percent to 90 percent) of the high voltage signal on the chamber is 20 nsec.

3) Spark chamber read-out

A coreboard with ninety-six ferrite memory cores is attached to each of the eight ground planes of the spark chamber (Fig. 2, page 15). A "write" wire, which is connected to one of the ground strips, threads each core and carries spark current in the direction that sets the core. Two additional wires thread each core -- a "read" wire

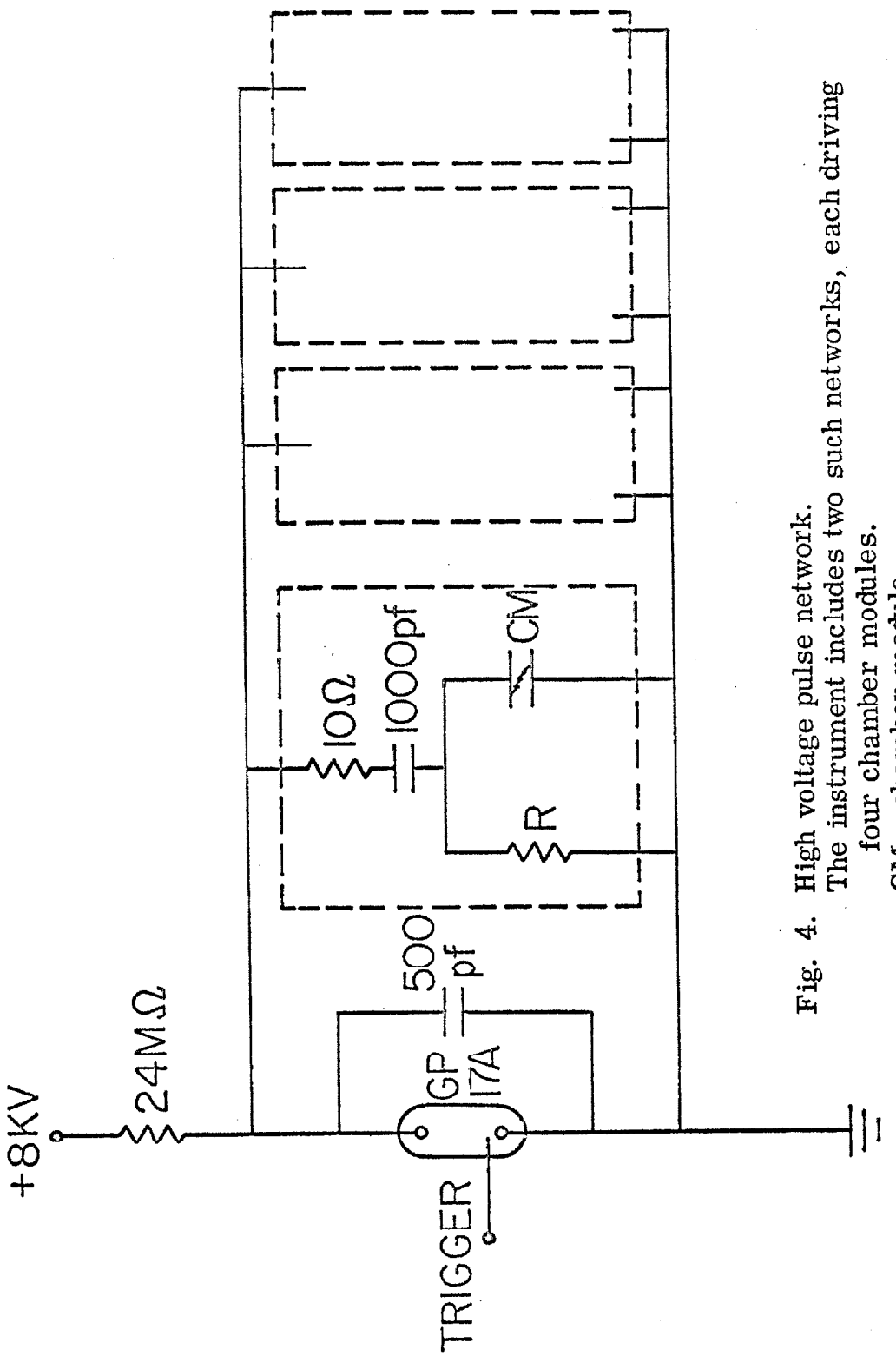

Fig. 4. High voltage pulse network.
The instrument includes two such networks, each driving four chamber modules.
CM - chamber module.
R - adjustable resistor (see text).

which carries a current pulse to reset the core, and a "sense" wire on which a voltage pulse is induced when a core changes state. The cores of each board are arranged in a 6 x 16 matrix (Fig. 5). Six read wires and sixteen sense wires thread the board. The sense wires of the eight coreboards are connected in parallel to sixteen sense discriminators. Each of the read wires on each coreboard is connected to its own read current driver. These forty-eight read current drivers are pulsed in turn, thereby interrogating and resetting sixteen cores at a time. A voltage pulse on a particular sense wire at the time when a given read wire is pulsed, indicates that the core threaded by that pair of wires has been set by a spark.

Interrogation of the cores consists of two steps. (See Fig. 6.)

(1) A single read current driver (R) is pulsed, thereby resetting sixteen cores on one coreboard. If any of the sixteen cores has been set by a spark, resetting it induces a voltage pulse on the sense wire which threads that core. The voltage pulse triggers a sense discriminator (S) whose output is stored temporarily in the 16-bit shift register.

(2) The shift register is examined, one bit at a time, to determine which cores, if any, had been set. The spark address scaler counts the bits as they are examined, thus keeping track of the location of the corresponding core. If a shift register bit in the "on" state is detected, a number representing the location of the corresponding core (i.e., the "spark address") is transferred from the spark address scaler into the output buffer. After all sixteen bits of the shift register have been examined, steps (1) and (2) are repeated with the next read current driver.

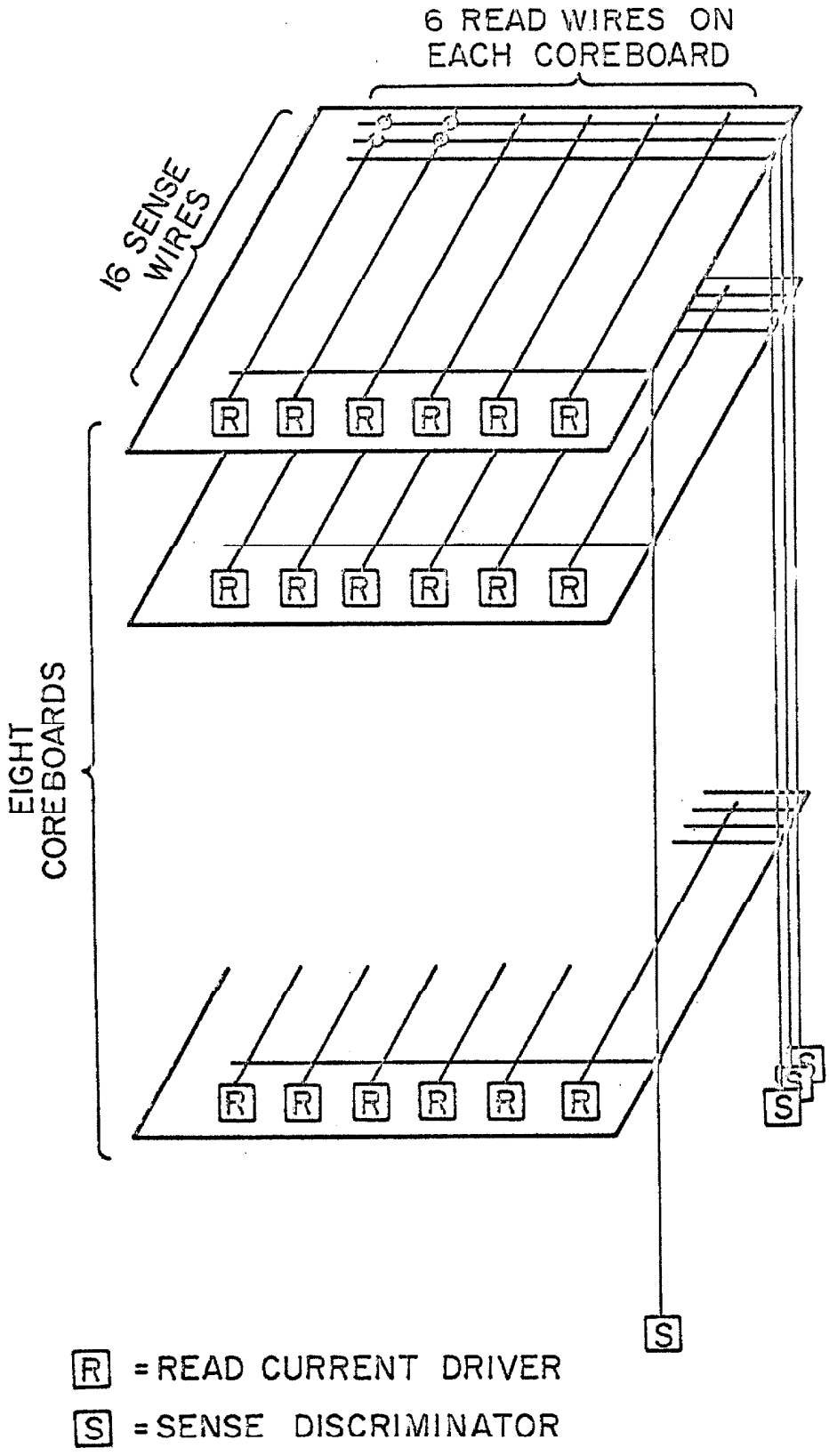

Fig. 5. Memory core arrangement.

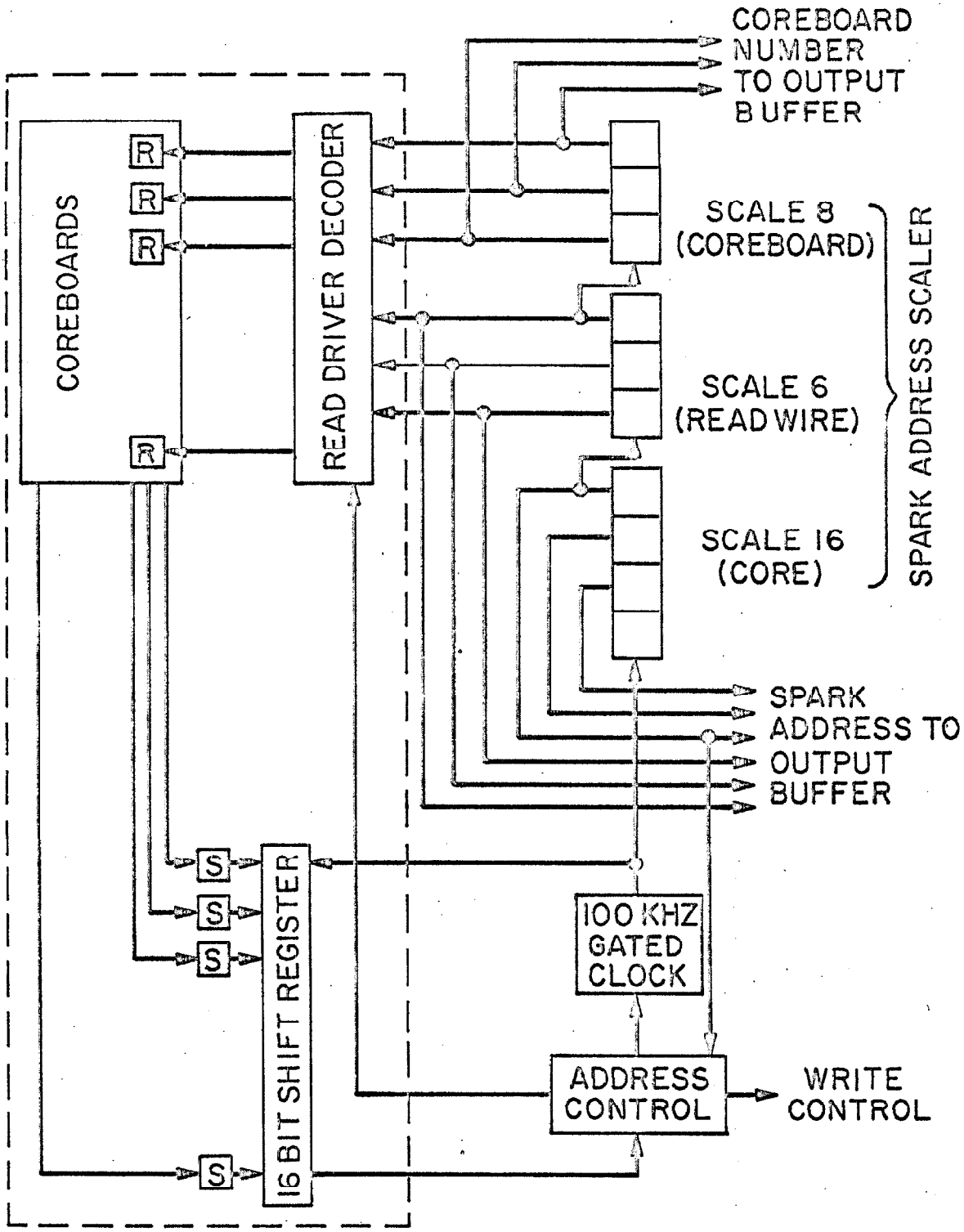

Fig. 6. Core read-out electronics. Dashed line indicates components enclosed by the spark noise shield.

These steps are repeated until each of the forty-eight read wires has been pulsed in turn. The process of core interrogation is interrupted each time two spark addresses have been transferred into the output buffer. The two addresses and the coreboard number are recorded on the magnetic tape, and then the core interrogation continues. (If only one set core is observed on a coreboard, then the board number, the spark address, and an artificial address indicating no second spark are recorded.) In this manner the system is capable of recording any number of spark addresses, two at a time.

Because a single spark may set two adjacent cores, we reduce the total number of bits recorded by building a two-core resolution into the system. The address of a set core is recorded as a number between 0 and 47, so pairs of adjacent cores have the same address. If two adjacent cores are set, only one address is recorded, that of the first of these cores.

After all cores have been interrogated, a switch removes the 35 V power from the read current drivers. The power is switched on after the next event when the system is again ready to interrogate the cores. This procedure insures that no power is on the drivers when a spark occurs in the chamber. This safeguard is necessary in order to prevent the spark noise from triggering the drivers and resetting all the cores.

The cores are EMI 51-114B (Electronic Memories, Inc., Hawthorne, Calif.). They are 0.050-inch o.d. cores with very fast switching. A 20-nsec write signal with as little as 2 amperes peak current sets a core. We use a 1-μsec, 1-ampere pulse with less than 30 nsec rise time to interrogate and reset the cores. With this read signal, a typical sense line signal from a set core is 3 volts peak, 30 nsec full width at half maximum (FWHM). The sense line signal

from a core which has not been set is 0.6 volts peak, 10 nsec FWHM. The sense discriminator integrates the sense pulse before discriminating, and so can easily distinguish these two kinds of signal.

4) Spark noise shielding

A box of 0.040-inch aluminum completely surrounds the spark chamber. It shields the photomultipliers, discriminators, pulse height analyzers, and associated circuits from the radio frequency noise of the sparks. The high voltage pulser and dc-dc converters are located inside the box.

Also mounted inside the box, are the read current drivers, the decoder on the input of these drivers, the sense discriminators, and the shift register on the output of these discriminators. (See Fig. 6.) The signals between these read-out circuits and the circuits outside the box are the dc levels of flip-flop outputs. They penetrate the wall of the box on low pass, feed-through filters. Similarly feed-through filters are on the power lines.

The only unfiltered wire penetrating the box is the coaxial cable carrying the trigger signal from the coincidence circuit to the high voltage pulser. This line cannot be filtered because a fast signal is required to trigger the high voltage with minimum delay. The coincidence circuit is mounted near the hole in the box through which its output cable passes and is securely grounded to the box. This cable is not connected to any other circuit. (A separate coincidence circuit triggers the control logic.)

The grounding is arranged to minimize the length of spark current ground paths and to minimize noise pickup in other circuits. Ground lines carrying spark currents return to the high voltage pulser over the shortest possible path. The pulser and the outputs

of the high voltage power supplies are grounded to a plate which is in turn connected to the box at only one point. All external circuit grounds connect to the box at one point. The coincidence signal cable is separated from the high voltage pulser ground by a pulse transformer.

When the chambers are operated with the box in place no spark noise is detected by any of the external circuits.

III. BALLOON FLIGHTS

The data reported in this thesis are derived primarily from four balloon flights of our electron detector. We launched the balloons from Fort Churchill, Manitoba in June and July, 1967. Table 2 summarizes pertinent flight conditions. On flights C1, C2, and C4 the detector telescope pointed toward the zenith. During flight C3 the detector was inverted to look at the upward moving, splash albedo.

We selected Fort Churchill as the launch location because of its low geomagnetic cutoff rigidity. Contours of constant cutoff rigidity in the Churchill vicinity are shown in Figure 7. Also shown are the trajectories of our four flights. The cutoffs in this figure were calculated using a spherical harmonic expansion of the earth's internal magnetic field (36). These values should be considered as upper limits because external currents are likely to lower the cutoffs. (We shall discuss this effect further in Chapter V.)

In order to minimize the contamination of our measurements by atmospheric secondary electrons, we used the largest available balloons to carry our detector to the highest possible altitude. These are polyethylene balloons holding 10.6 million cubic feet of helium. They floated at an atmospheric depth near 2.0 g/cm^2 for 9 to 12 hours during each flight. Figure 8 shows the altitude curves of our flights.

All the flights occurred during quiet geomagnetic conditions. Figure 9 shows the planetary magnetic index, Kp, during the period of our observations (37). The daily averages of the Mt. Washington neutron monitor over the same period appear in Figure 10 (38). The neutron monitor count rate during all the flights differed by less than

TABLE 2

BALLOON FLIGHTS

Flight number	C1	C2	C3	C4	P1
Launch date (1967)	17 June	2 July	9 July	21 July	7 April
Launch time (a)	10:27	03:58	03:23	03:20	11:27
Begin float (a)	13:40	09:00	09:00	09:30	16:00
Terminate (a)	03:30	17:45	19:25	21:15	21:55
Floating depth (g/cm^2)	2.1-3.4 (b)	2.0	2.3	2.1	5.2
Sensitive time at float (min)	791	504	496	530	346
Orientation	zenith	zenith	nadir	zenith	zenith
Configuration (c)	normal	normal	normal	modified	normal
Kp (d)	3-	0+	1-	1+	1
Mt. Washington neutron monitor (e)	2274	2244	2285	2317	2260

(a) Universal Time.

(b) See Fig. 8.

(c) See page 9.

(d) Mean of three-hour Kp indices during float (37).

(e) Mean of hourly count rate during float (38).

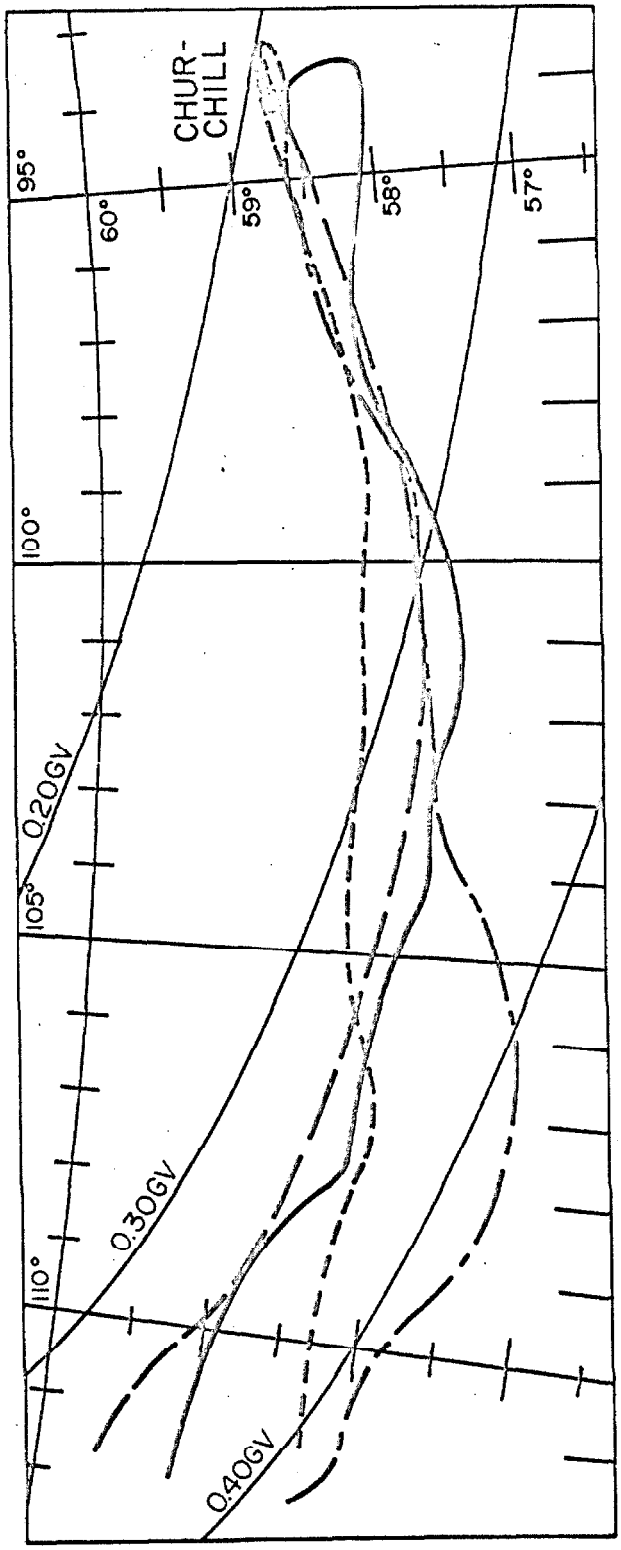

Fig. 7. Trajectories of the balloon flights and contours of constant geomagnetic cutoff rigidity. Cutoffs are derived from the internal geomagnetic field only.

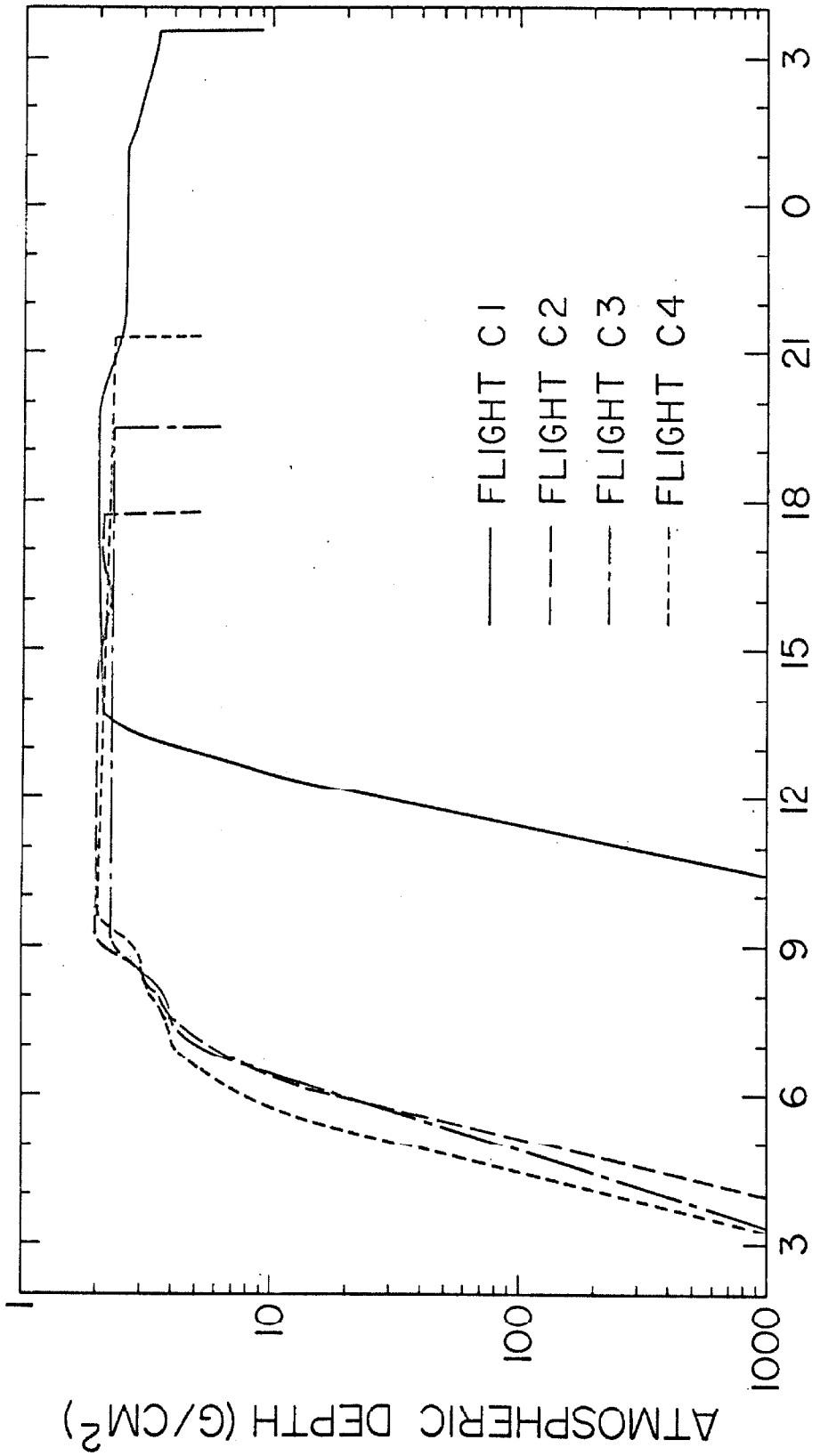

Fig. 8. Altitude curves for flights, C1, C2, C3, C4.

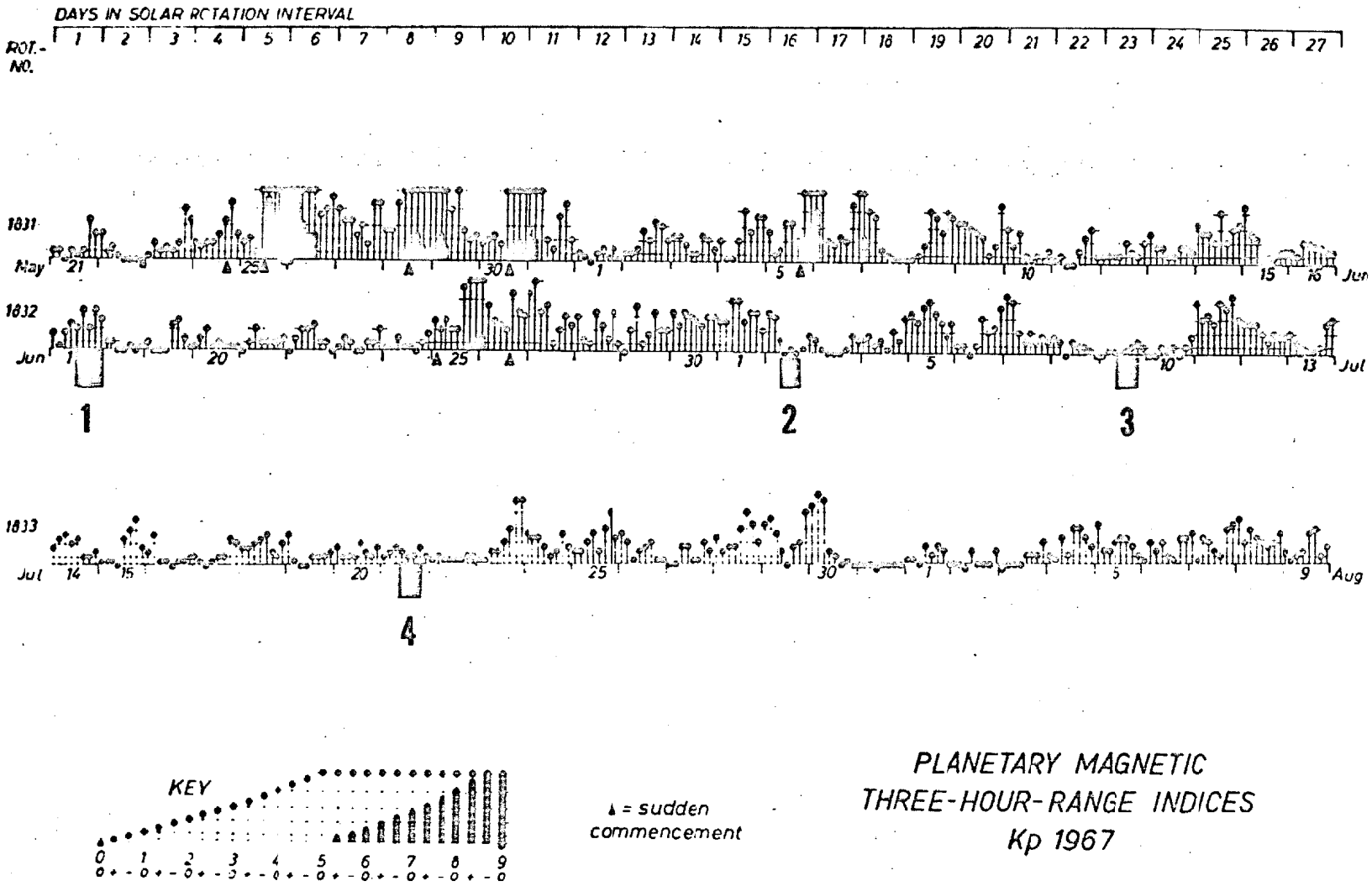

Fig. 9. Planetary magnetic index, Kp, during Summer 1967. Numbered bars indicate flights C1, C2, C3, and C4.

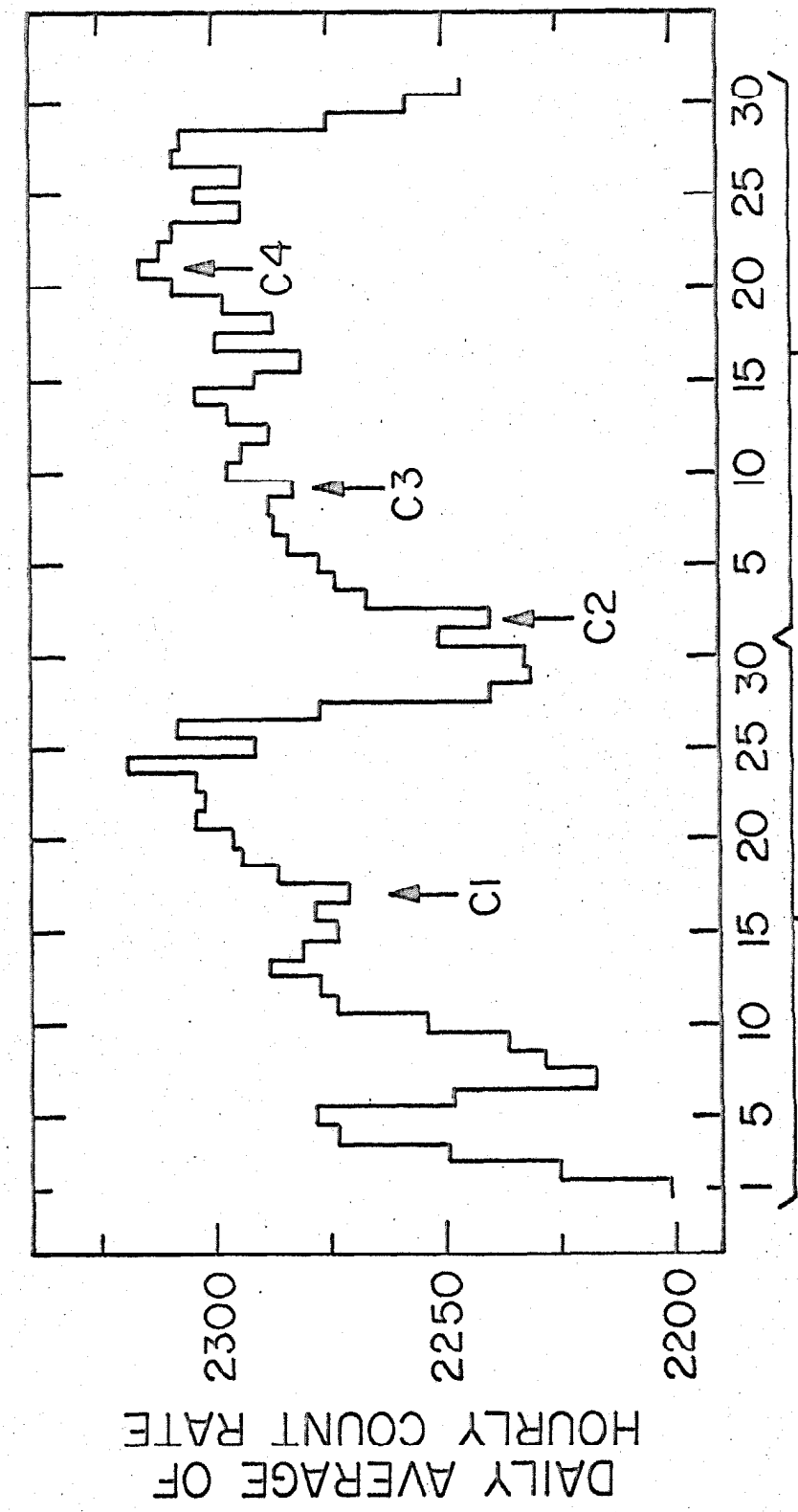

Fig. 10. Mt. Washington neutron monitor count rate. Numbered arrows indicate balloon flights of our detector.

2 percent from that of flight C1. (For comparison, the maximum neutron monitor rate of this solar cycle, in May 1965, was 9 percent higher; and the monthly average in June 1966 was 4.4 percent higher.)

Further evidence that these flights occurred during quiet times comes from the solar proton monitor on the Explorer 34 satellite (39). No solar protons with energy above 30 MeV were detected outside the magnetosphere from 9 June, a week before flight C1, through the end of July. A barely detectable flux of 10 MeV protons, less than 0.2 particles/cm^2 sec sr, was present during flight C1, but none was detected during our other flights.

Our discussion of the albedo measured on flight C3 is aided by data from an additional flight of the same instrument, launched at Palestine, Texas, in April, 1967, (Flight P1, table 2). The vertical geomagnetic cutoff at the location of the detector remained above 3.8 GV throughout the flight, so all observed electrons were well below cutoff. The data from this flight are of limited value because of a balloon failure which resulted in the detector floating at an atmospheric depth of 5.2 g/cm^2 instead of the expected 2 g/cm^2. This lower altitude gave a larger flux of atmospheric secondaries than desired.

IV. DATA ANALYSIS

A) Event selection and detection efficiency

We attribute to electrons those recorded events satisfying the following four criteria:

(1) A triple coincidence, including the Čerenkov counter, is registered.

(2) No guard counter signal accompanies the event.

(3) The pulse height from the counter $\Delta E1$ corresponds to energy loss between $0.5\ I_o$ and $1.7\ I_o$, where I_o is the most probable energy loss of a relativistic singly charged particle.

(4) Either (a) there is no output from $\Delta E2$,
or (b) there is an output from $\Delta E2$ corresponding to energy loss greater than $1.7\ I_o$, and the spark chamber did not show a single straight track.

These criteria eliminate most of the background due to particles other than electrons, but they also eliminate some electrons. The solid curve in Figure 11 shows the electron detection efficiency as a function of energy.

For electrons with energy between 100 MeV and 1000 MeV we determined the efficiency directly, using the monoenergetic external electron beam at the California Institute of Technology synchrotron. At these energies, the rejection of electrons is principally due to the second criterion – guard counter signals. For lower energies, we derive the efficiency from a combination of measurements and calcu-

Fig. 11. Electron detection efficiency vs. kinetic energy at the top of the detector.

Solid curve – efficiency with all selection criteria included.

Dashed curve – efficiency with fourth criterion ignored.

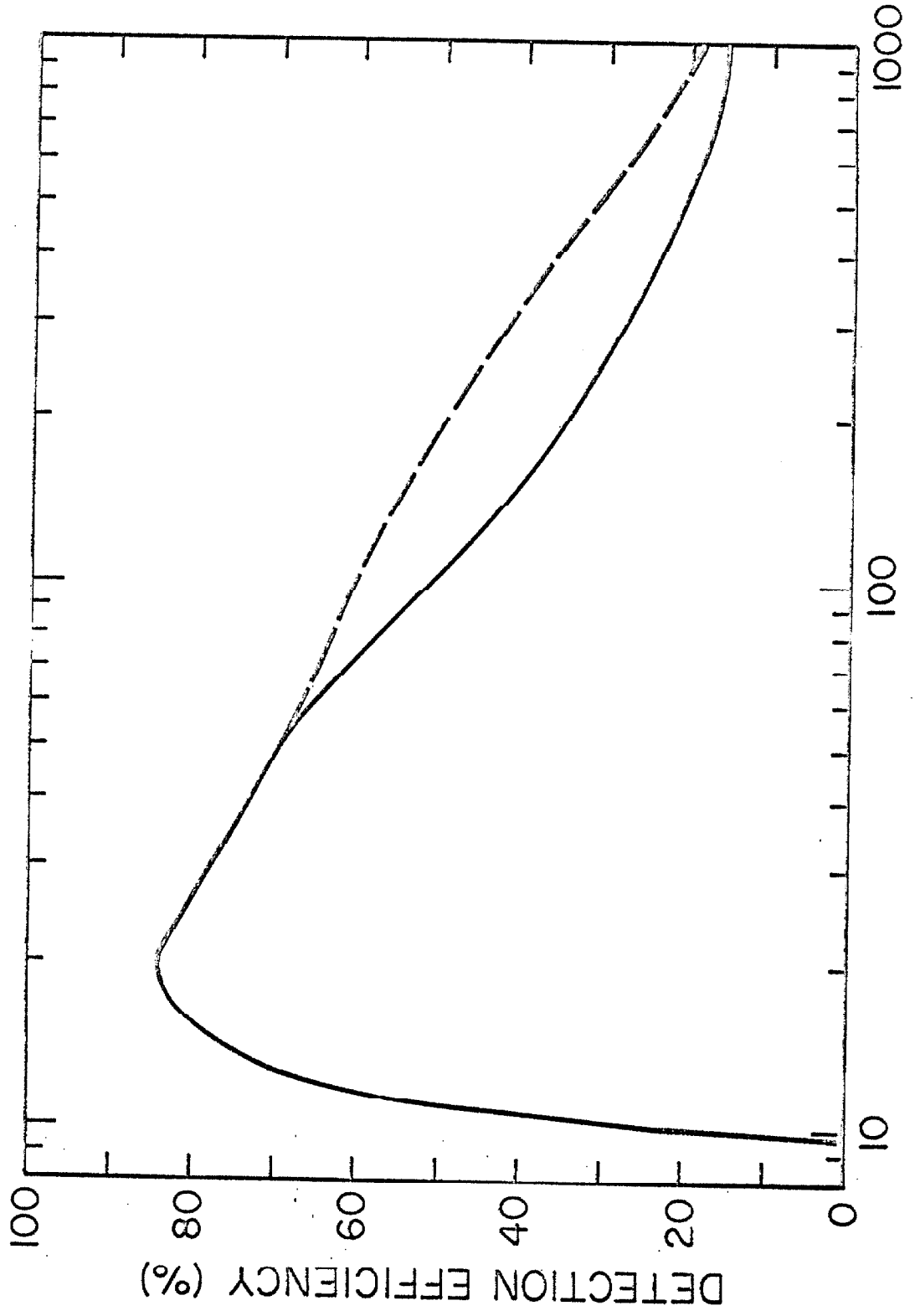
DETECTION EFFICIENCY (%)
0
20
40
60
80
100
10
100
1000
ELECTRON ENERGY (MEV)

Fig. 11

lations, as described in the following paragraphs. We estimate that systematic errors in our final electron fluxes due to errors in the efficiency curve presented here and in section B are less than 10 percent over the entire energy range.

1) Čerenkov counter

The decrease in detection efficiency below 30 MeV is due to the Čerenkov counter response. The mean number of photons, $\overline{N}_\gamma(\beta)$, emitted by a charged particle moving with velocity βc through a medium with index of refraction n, is proportional to $1 - (1/n\beta)^2$; (35). The mean number of photo-electrons, $\overline{N}_e(\beta)$, emitted by the photomultiplier cathode is proportional to $\overline{N}_\gamma(\beta)$. Since $\overline{N}_e(\beta) < 0.1\,\overline{N}_\gamma(\beta)$, the probability that there be exactly N_e photo-electrons emitted on a given event is governed, to a good approximation, by Poisson statistics of $\overline{N}_e$. We assume that the detection efficiency, $\eta(\beta)$, is equal to the probability that at least one photo-electron be emitted. Then

$$\eta(\beta) = 1 - \exp\left[-\overline{N}_e(\beta)\right] = 1 - \exp\left[-\overline{N}_e(1)\left(\frac{n^2}{n^2-1}\right)\left(1 - \frac{1}{n^2\beta^2}\right)\right] \tag{2}$$

Our measurement of $\eta(1) = 0.96 \pm 0.02$ (using electrons with energy above 200 MeV from the synchrotron) enables us to calculate $\overline{N}_e(1) = 3.2$. We then calculate $\eta(\beta)$ using equation (2).

2) Guard counters

At the synchrotron we measured the chance of a guard counter being triggered by incident electrons with energy $\geq$ 100 MeV. We use data from the flights to extend the curve below 100 MeV in the following manner. From the diurnal flux variation, which affects only low energy electrons, we determine that 16 ± 5 percent of electrons which otherwise would be type 1 (see page 40) are eliminated because of guard counter signals. (The diurnal variation is discussed more fully in Chapter V.) We extend the curve of guard counter probability below 100 MeV as a smooth curve which gives the correct value, 16 percent, for the average probability for type 1 electrons.

3) Energy loss counter 1

Using electrons from the synchrotron with energy as low as 30 MeV, we measured the probability of an incident electron giving energy loss outside the range 0.5 I_o to 1.7 I_o. For electrons between 30 and 100 MeV there is no significant energy dependence of this value, 6 ± 1 percent. This is consistent with the theoretical energy loss distribution (40). We assume that this probability is the same between 10 and 30 MeV.

4) Energy loss counter 2

Our measurement of the probability of an electron failing to satisfy the fourth criterion extended down to 30 MeV. At this energy the probability is less than 1 percent, so we ignore it at lower energies.

B) Energy determination

We divide the selected events into four categories.

Type 1: Both the spark chamber and ΔE2 register no particle.

Type 2: ΔE2 registers no particle and the total number of sparks in all chamber gaps is one, two, or three.

Type 3: ΔE2 registers no particle, and the total number of sparks is greater than three.

Type 4: ΔE2 registers a pulse height corresponding to energy loss greater than 1.7 I_o.

These four types correspond approximately to electron energies at the top of the detector of 12 to 50, 50 to 100, 100 to 350, and 350 to 1000 MeV respectively. We calibrated the detector using the monoenergetic external electron beam of the Caltech synchrotron to determine the energy dependence of the probability for producing each type of event. The results for the normal detector configuration are shown in Figure 12. For the modified configuration, the division between type 2 and type 3 events is redefined; instead of dividing between three and four sparks, we divide between two and three. The calibration curves for the modified configuration are shown in Figure 13.

The energy resolution afforded by this division of events is rather coarse. For example, curve 3 in figure 12 has full width at half maximum (FWHM) 200 percent of its peak. The calibration of the detector system at the Caltech synchrotron shows that better energy resolution is possible, ~ 80 percent FWHM at 150 MeV, ~ 100 percent FWHM at 500 MeV. This is achieved by counting the total number of sparks in the electron shower. We cannot achieve

Fig. 12. Probability of an electron producing an event of type 1, 2, 3, or 4 vs. kinetic energy at the top of the detector.
Detector in normal configuration.

Fig. 13. Same as figure 12.
Detector in modified configuration.

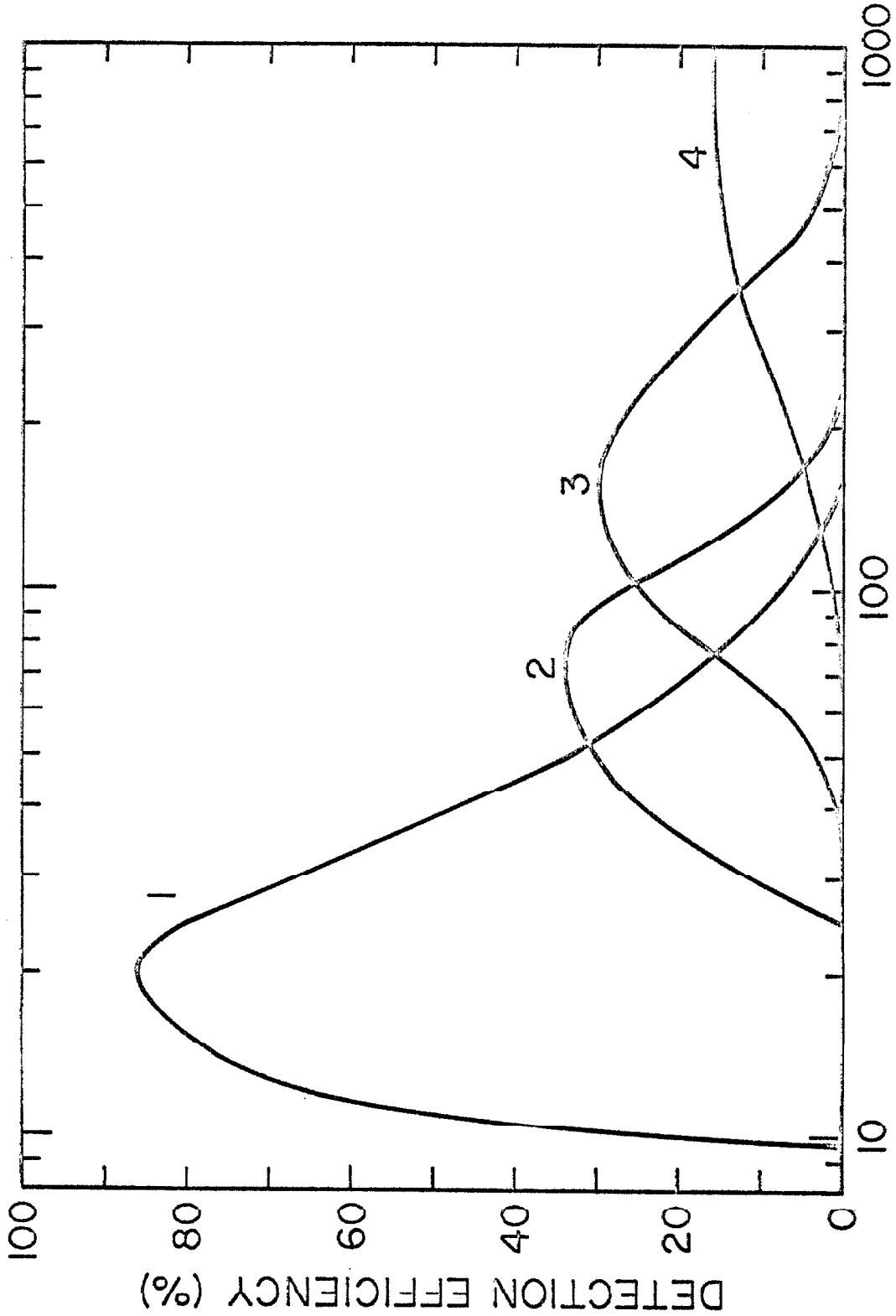
DETECTION EFFICIENCY (%)
100
80
60
40
20
0
10
100
1000
ELECTRON ENERGY (MEV)
1
2
3
4

Fig. 12

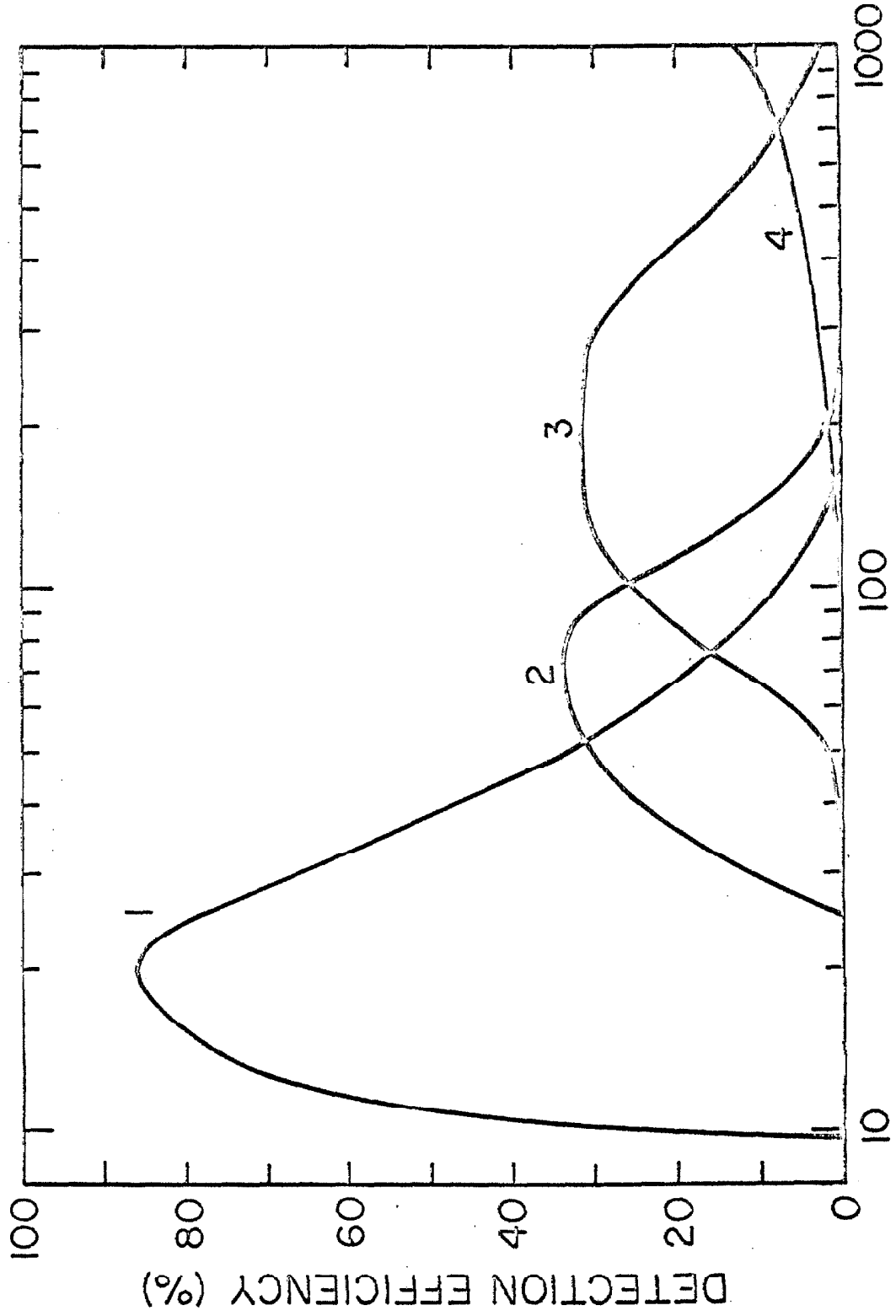
DETECTION EFFICIENCY (%)
100
80
60
40
20
0
10
100
1000
ENERGY (MEV)
1
2
3
4

Fig. 13

this resolution with our cosmic ray data because the chamber efficiency during flight decreased significantly from the efficiency on the ground.

We derive an electron spectrum from the observed number of events of each type with the following iterative unfolding technique. We make a first estimate of the spectrum using the approximate energy interval to which each type of event corresponds. Using this approximate spectrum and the curves of Figure 12 or 13, we calculate the fraction of the observed events of each type which is due to electrons of each energy interval. As an example, Table 3A shows these fractions for the detector in the normal configuration and an assumed electron spectrum of the form $\frac{dJ}{dE} = KE^{-1}$. Next, we divide the observed number of electrons of each type according to these fractions and add to find the total number of events observed with each energy (Table 3B). We then correct the number of events in each energy interval for the detection efficiency in that interval. This efficiency is calculated from Figure 11 and the assumed energy spectrum. Finally, we calculate an electron spectrum from these corrected numbers. If this spectrum does not agree with the spectrum originally assumed, we repeat the previous steps using this newly calculated spectrum as the assumed spectrum. We continue this iterative procedure until the calculated spectrum differs from the assumed spectrum by less than the statistical uncertainty. Usually the process converges after one or two iterations.

C) Systematic uncertainties in electron spectrum

An uncertainty in the resulting electron spectrum arises from the fact that the efficiency of the spark chamber during the flight was

TABLE 3

UNFOLDING ELECTRON SPECTRUM

A) Fraction of events of each type attributed to electrons in a given energy interval

Assumed electron spectrum: $dJ/dE = KE^{-1}$

Type	12-50	50-100	100-350	350-1000 MeV
1[a]	.764	.163	.020	0.0
2	.222	.523	.256	0.0
3	.005	.195	.720	.079
4[b]	0.0	.008	.329	.664

(a) Sum is less than 1.0 because of electrons attributed to the 9.6 to 12 MeV interval.

(b) Distribution shown here assumes zero detection efficiency above 1 GeV. See text, section C.

TABLE 3

UNFOLDING ELECTRON SPECTRUM

B) Number of electrons observed during flight C1 and calculation of trial spectrum

Type	Observed Events[c]	Sensitive time (min)	Events attributed to each energy interval 12-50	50-100	100-350	350-1000 MeV
1	31	175	23.8	5.1	0.6	0.0
2	20	175	4.4	10.5	5.1	0.0
3	39	791	0.2	7.6	28.1	3.1
4	36	791	0.0	0.3	11.8	23.9
Total events in each energy interval[d]			176.6	78.2	65.9	27.0
Detection efficiency %			78.6	60.6	38.5	19.9
Flux (electrons/m^2 sec sr)[c]			38.2 ± 7.2	30.3 ± 7.0	40.3 ± 7.7	31.9 ± 6.1
Differential flux[e] (electrons/m^2 sec sr MeV)			1.00 ± .19	0.61 ± .14	0.161 ± .031	0.049 ± .009
Effective energy (MeV)			26.6	72.1	200	619

[c] Type 1 and 2 events from nighttime part of float. Type 3 and 4 from entire float. (See Part V).

[d] Normalized to 791 minutes.

[e] Uncertainty shown here is statistical error due to number of observed events.

lower than during the synchrotron calibration. This results in an uncertainty in the division of events between type 2 and type 3. During flight, typical efficiency of a single spark chamber gap for detecting the single track of penetrating protons was 80 percent, compared with 95 percent on the ground. This would imply that most events which should give four sparks in the chamber would in fact give three. We therefore calculate each spectrum, first assuming that every event with three sparks should have four sparks, and then assuming that none of these should have four sparks. The electron fluxes calculated for the 100 to 350 MeV interval using these two assumptions differ by 15 percent. We take the intermediate flux and assign a systematic uncertainty of $\pm$ 7 percent to this value. For other energy intervals the difference is less than 5 percent.

An additional uncertainty occurs because we could not measure the detection efficiency for electrons above 1 GeV. Thus an undetermined fraction of the type 4 events is due to these higher energy electrons. This fraction is small because the differential electron spectrum above 1 GeV falls at least as steeply as E^{-1}; and above 2 GeV, at least as E^{-2} (4) (5) (6). A simple extrapolation of the dashed curve of Figure 11 indicates the efficiency falls near zero in the neighborhood of 2 GeV. We calculate the electron spectra, first assuming the efficiency is zero above 1 GeV, and then assuming that the efficiency is constant at the 1 GeV value from 1 GeV to 2 GeV and drops to zero above 2 GeV. These two extreme assumptions give results differing by 30 percent for the electron flux between 350 and 1000 MeV. We take the flux to be between these two values, with a possible systematic error of 15 percent.

D) Dead time correction

In evaluating the event rate during any given time interval, we use the sensitive time t_s, calculated as

$$t_s = t - t_w n_w - t_e n_e \qquad (3)$$

where t = total real time

n_w = number of words recorded on the magnetic tape

t_w = time required to write each word

= 288 ms (Part II, section C1)

n_e = number of events recorded

t_e = time required to interrogate the cores

= 9 ms (Part II, section C1).

Flight C4 had the largest fractional dead time ($t - t_s = 0.256\ t$) because the detector system recorded an event on every double coincidence. For this flight, we can check our dead time calculation. The T1, T2 rate scaler (see Fig. 3, Part II, section C1) counts double coincidences at all times, whether or not an event is being written on the magnetic tape. The double coincidence rate, calculated from the number of recorded events divided by t_s, differs by 0.6 percent from the rate indicated by the rate scaler. This error is negligible for our analysis.

E) Contamination by other particles

Helium nuclei, and other particles with charge greater than one, are completely eliminated by the requirement that $\Delta E1$ show less than $1.7\ I_o$.

Most protons are eliminated by the requirement of a gas Cerenkov signal. The flux of protons with sufficient energy to leave less than $1.7\ I_o$ in $\Delta E1$ (greater than 280 MeV) is 2.0×10^3 m^{-2} sec^{-1} sr^{-1}, but the proton flux above the Cerenkov counter threshold (16 GeV) is only 0.1×10^3 m^{-2} $ster^{-1}$ sec^{-1} (41).

1) Protons above gas Cerenkov threshold

We need consider only the protons which suffer a nuclear interaction in the detector. The protons which do not interact are eliminated because they show a single straight track in the spark chamber. In addition, 90 percent of the protons which do not interact have pulse height in $\Delta E2$ corresponding to less than $1.7\ I_o$, thus failing to satisfy the fourth selection criterion.

With the detector system in its normal configuration, 20 percent of the protons do interact below $\Delta E1$. In the modified configuration of the flight C4 the added lead raises this fraction to 28 percent. These fractions are based upon an inelastic interaction length in lead of 204 g/cm^2 (42). The interacting protons may be indistinguishable from energetic electrons in the spark chamber, but at least 90 percent of them are eliminated by the requirement that no guard counter be triggered. (See Appendix.) In the normal configuration, the remaining interacting protons give a rate less than 0.45 event/hour. These events must all be of type 4. During flights C1 and C2 the observed type 4 rate is 2.7 events/hour. Thus we set an

upper limit of 17 percent to the proton contamination in these events. This leads to an upper limit of 15 percent overestimate in the flux of 350-1000 MeV electrons and 3 percent overestimate between 100 and 350 MeV. Similar limits may be set for flight C4.

The proton rejection would have been significantly better than this if the spark chamber efficiency during the flights had not deteriorated. In that case, we would have required that an electron event show an electromagnetic cascade beginning in the first lead plate. This would limit the contamination to protons which interacted in this plate, $\sim$ 6 percent of the protons, rather than permitting protons which interact anywhere in the detector.

During flight C3, in which the detector pointed toward the nadir and observed splash albedo particles, this source of contamination is absent. The flux of relativistic splash albedo protons is negligible compared to both the primary protons and the splash electrons (43).

2) Protons below the Cerenkov thereshold

Approximately 0.7 percent of the protons with energy between 0.4 and 16 GeV produce a false triple coincidence. (See Part II, section B3.) As with protons above the Cerenkov threshold, we need consider only the 20 percent which interact in the detector. Data from flight C4 allow us to estimate directly the contamination from all particles below the gas Cerenkov threshold. We selected events from flight C4 which were not accompanied by Cerenkov signals but did satisfy the other criteria for electrons. We divided these among the types as if they were electrons. Table 4 summarizes the results. The contamination listed in this table is negligible in all types.

TABLE 4

EVENTS FROM FLOAT PERIOD OF FLIGHT C4

Type	1	2 and 3	4
A) Events satisfying all electron criteria	231	91	12
B) Events satisfying all electron criteria except for Cerenkov signal	487	202	87
C) 0.7% of (B)	3.4	1.4	0.6
D) Contamination $\left(\frac{(C)}{(A)}\right)$	1.5%	1.5%	5%

3) Muons and pions

The contamination calculated in the preceding paragraph includes any contribution from muons or pions below the gas Cerenkov threshold (1.8 GeV for muons, 2.4 GeV for pions). Muons above this energy penetrate the entire detector with negligible chance of a nuclear interaction and so produce no contamination.

The flux of pions above 2.4 GeV is so low that it may be ignored. The production spectrum of charged pions in the atmosphere has been calculated from the known primary cosmic ray flux (44) (45). The integral flux of pions above 2.4 GeV produced in 1 g/cm^2 of atmosphere is 4 particles/m^2 sec sr. However, since the pions decay after traversing much less than 1 g/cm^2, the equilibrium flux is much less than 4 particles/m^2 sec sr. This is negligible compared to the flux of protons above the Cerenkov threshold, 100 particles/m^2 sec sr.

F) Atmospheric secondaries

The analysis described above permits us to calculate the spectrum of electrons incident on the detector system. For the flights in which the detector looked at the zenith, the quantity of physical interest is the electron flux incident at the top of the atmosphere. We must, therefore, subtract the contribution of atmospheric secondary electrons from the observed spectrum.

In the upper 10 g/cm^2 of the atmosphere, the principal source of secondary electrons at energies $\gtrsim$ 20 MeV is the decay of charged pions. These pions originate in interactions of primary cosmic ray nuclei with air nuclei. The resulting secondary electron spectrum may be calculated from the known primary cosmic ray spectrum and

the pion production cross-sections. Two such calculations have been published (44) (45). The calculated electron spectra at 2 g/cm^2 atmospheric depth are shown in Figure 14. Also shown is the spectrum of knock-on electrons (46) and the combined spectrum formed by adding the knock-on electrons to those originating in interactions.

At energies $\lesssim$ 100 MeV the two independently calculated spectra differ by a factor of two to three, although both authors claim an uncertainty of less than 25 percent. Between 200 and 1000 MeV, the two are in good agreement. Part of the discrepancy between the two results appears to lie in the treatment of pions produced by interactions of low-energy protons. Where Perola and Scarsi (44) derive 30 percent of their 10 to 100 MeV electrons from primary particles with rigidity below 2 GV, Verma (45) derives about 10 percent of these electrons from primaries of similar rigidity. In this regard, the Perola and Scarsi results appear to be more reliable. They make more extensive use of available accelerator data on pion production spectra than does Verma. This is especially true for pions from protons below 3 GeV.

The importance of the secondary electron contribution at these energies is clear when we consider the variation of electron flux with atmospheric depth (Fig. 15). The observed rate of type 1 events (electrons of approximately 12 to 50 MeV) decreases almost linearly with atmospheric depth. This indicates that even at 2 g/cm^2 a large fraction of the observed electrons are atmospheric secondaries. Also plotted in Fig. 15 (curves 1 and 2) are the expected event rates derived by folding the type 1 detection probability (Fig. 12) with the secondary electron spectra calculated by Perola and Scarsi and by Verma. We include the knock-on electron contribution

Fig. 14. Kinetic energy spectrum of atmospheric secondary electrons at 2 g/cm^2.

Curve 1 Electrons from interactions, Perola and Scarsi (44).

Curve 2 Electrons from interactions, Verma (45).

Curve 3 Knock-on electrons (46).

Curve 4 Sum of curves 1 and 3.

Curve 5 Sum of curves 2 and 3.

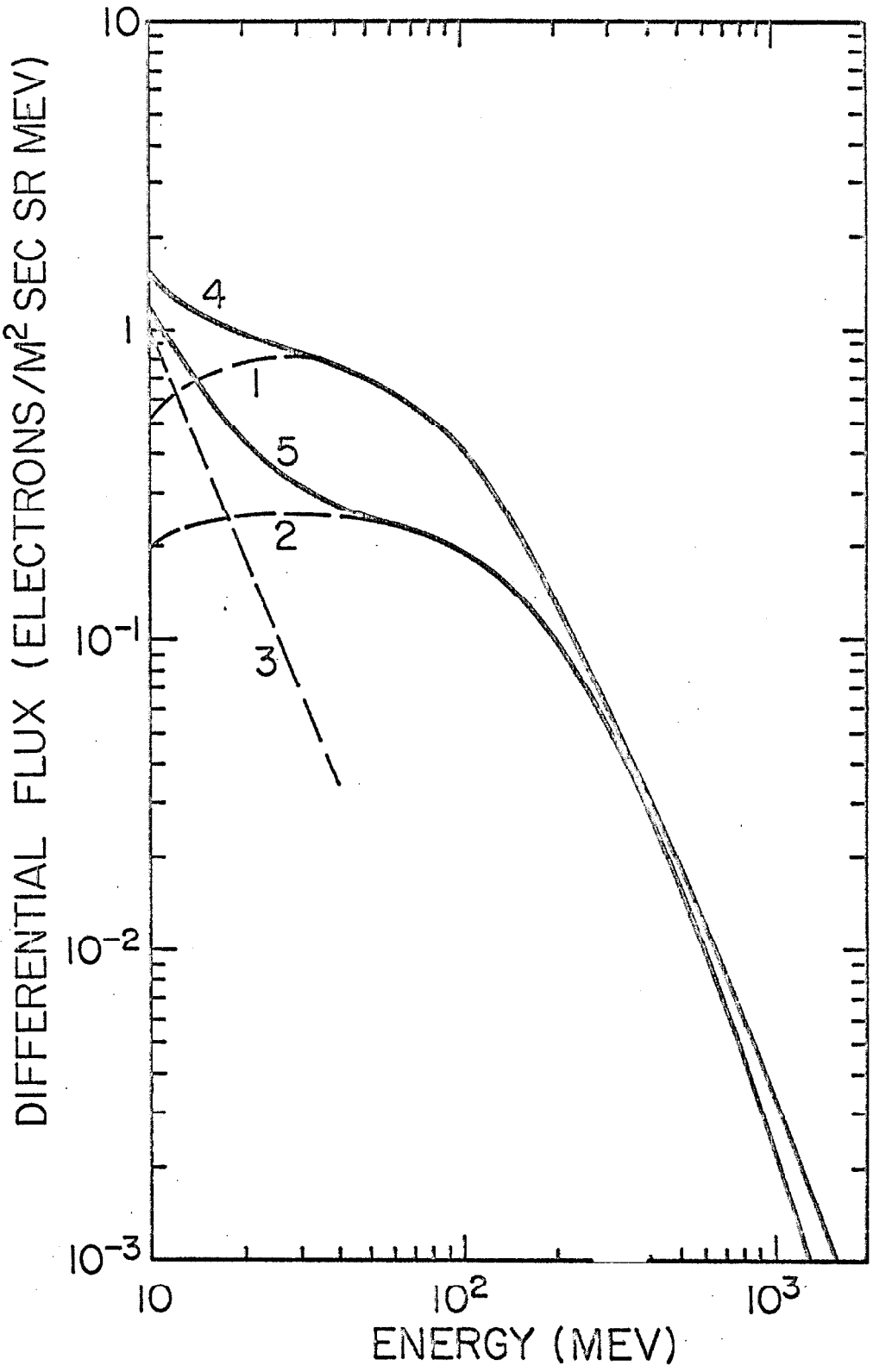
DIFFERENTIAL FLUX (ELECTRONS/M² SEC SR MEV)
10
1
10⁻¹
10⁻²
10⁻³
10
10²
10³
ENERGY (MEV)
1
2
3
4
5

Fig. 14

Fig. 15. Rate of type 1 events vs. atmospheric depth. Data points are combined results of data gathered during ascent of flights C1, C2, and C4 and data gathered during "night" portion of float on flights C2 and C4. (See Chapter V for distinction between "day" and "night" data.) (Ascent of all flights occurred at "night".)

Curve 1 Count rate derived from Perola and Scarsi (44) with addition of knock-on electrons (46).

Curve 2 Count rate derived from Verma (45) with addition of knock-on electrons (46).

Solid line Least squares fit to data, assuming $s(d) = d$.

Curve A Secondary contribution to solid line.

Curve B Primary contribution to solid line.

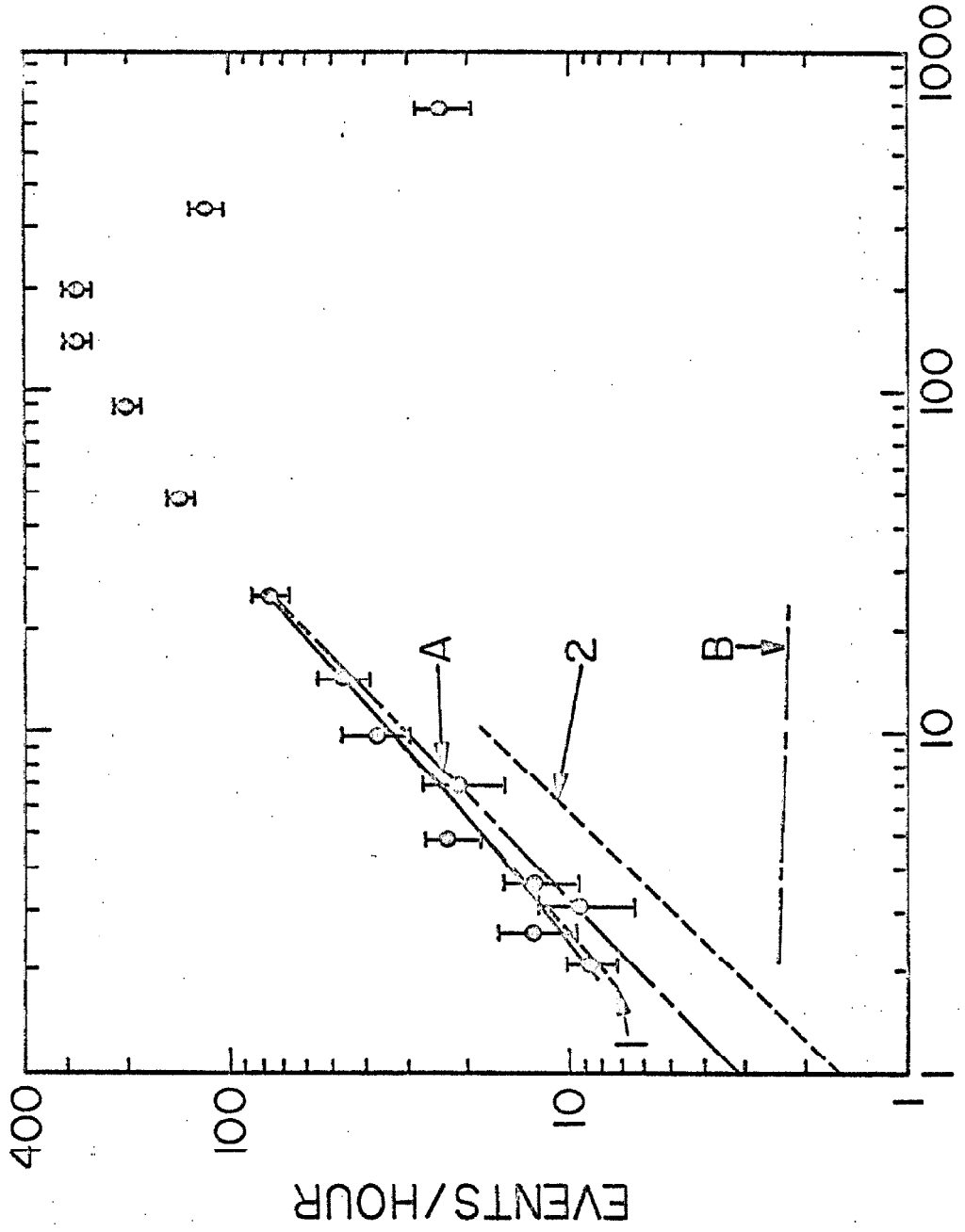
EVENTS/HOUR
400
100
10
1
1000
100
10
1
ATMOSPHERIC DEPTH (G/CM²)
A
2
B

Fig. 15

in these curves. We also make an approximate correction for the difference between the primary proton flux assumed in the calculations and the proton flux at the time of our flights. This correction is a 15 percent decrease in the case of Perola and Scarsi, and a 5 percent decrease in the case of Verma.

Because the two calculated secondary electron fluxes are in disagreement, we make an independent estimate, based upon our data of Figure 15. We derive the secondary flux from our data in the following manner. We take the altitude dependence of the total flux of type 1 electrons, J(d), to be of the form

$$J(d) = a\ s(d) + b\ p(d) \qquad (4)$$

where d is atmospheric depth; the function s(d) describes the depth dependence of the flux of secondary electrons; the function p(d) describes the depth dependence of the flux due to primary electrons; and the coefficients a and b are parameters which we determine by a least-squares fit to the nine data points from 2 to 25 g/cm^2.

The solid curve in Figure 15 is the least-squares fit for J(d) based upon the following assumptions:

1) s(d) varies linearly with depth. This is the depth dependence of the calculated curve 2.

2) p(d) is calculated by assuming a primary electron spectrum of the form E^{-n} with $n = 0.5$. The flux of primary electrons in the energy interval corresponding to type 1 events varies with depth as the incident electrons lose energy in penetrating the atmosphere.

Curves A and B indicate the secondary and primary contributions respectively to the least-squares fit. The solid curve, which is the

sum of A and B, fits the data with a χ^2 of 3.9. The primary electron contribution at 2.1 g/cm^2 resulting from this fit is 2.4 ± 1.5 events/hour, approximately one-fourth of the observed events. This result is not sensitive to the choice of n, the exponent of the primary energy spectrum. It differs from this value by less than 10 percent for any value of n between 0 and 2.

On the other hand, the results of the fit are very sensitive to the assumed depth dependence of the secondary flux. If we take $s(d) = d^{0.9}$ (in agreement with the depth dependence of curve 1), then the least-squares fit gives a primary electron contribution of 0.4 ± 1.6 event/hour, consistent with zero. In this case, the secondary electron contribution to the least-squares fit agrees with curve 1 within 5 percent. This is well within the 20 percent stated accuracy of the calculation from which curve 1 is derived.

If we take the secondary depth dependence as $s(d) = d^m$ and allow m to vary as a third parameter, we find the minimum χ^2, 3.5, for m = 0.85; in this case the primary electrons give -0.8 ± 1.7 event/hour, still consistent with zero.

This analysis leads us to two conclusions regarding electrons in the interval 12 to 50 MeV. First, our observations are in good agreement with the calculations of Perola and Scarsi and in clear disagreement with those of Verma. The contribution of atmospheric secondaries to our observed data falls within 20 percent of curve 1 whether we assume the secondary electron flux to vary linearly with depth or as slowly as $d^{0.85}$. We cannot reconcile our observations with a secondary contribution near curve 2. Secondly, we conclude that our results are consistent with the entire observed flux being atmospheric secondaries. As an upper limit to the primary contribution to type 1 events, we take the result of the least-squares fit assuming linear growth of secondaries, 2.4 ± 1.5 events/hour.

For events of type 2, 3, and 4, the count rate is so low that measurements of the rate during the balloon ascent have very large statistical uncertainty, precluding useful least-squares fitting. We note, however, that at energies above 200 MeV the two calculations agree with one another as well as agreeing with the measured data of L'Heureux (11). Therefore, we shall calculate the spectrum of the total flux at the detector and then subtract the spectrum of atmospheric secondaries calculated by Perola and Scarsi, to derive the primary flux. These spectra are presented in Part V.

V. RESULTS AND DISCUSSION

Our data permit conclusions on three problems in the study of cosmic ray electrons, discussed in the following three sections of this chapter. First, from the data of flight C3, we derive the spectrum of splash albedo electrons near Fort Churchill; and, for comparison, we present a measurement of return albedo electrons at lower latitudes, near Palestine, Texas. Then, using data from flights C1, C2, and C4, we present in section B a description of the diurnal variation of the low energy electron flux. Finally, in section C, we consider the primary electron spectrum.

A) Albedo electrons

1) Background

Primary cosmic ray nuclei entering the earth's atmosphere interact with air nuclei and produce numerous secondary particles. Some of these interaction products move upward and emerge from the atmosphere as "splash albedo." The electron component of the albedo comes from the decay of pions produced in the interactions. The $\pi \rightarrow \mu \rightarrow e$ decay of charged pions is the dominant electron source near the point of interaction. A second electron source is the $\pi^0 \rightarrow 2\gamma$ decay which initiates an electromagnetic cascade. The cascade from a photon of a few GeV energy may contain tens of electrons after penetrating two or three radiation lengths (47). (One radiation length in air is 36.5 g/cm^2 [48].) Thus the cascade source may dominate if the primary interaction can take place at least 30 g/cm^2 from the point of observation. Since the kinematics of the

interactions tend to collimate secondary particles in the forward direction, splash albedo particles are more likely to arise from primary cosmic rays incident at large zenith angles than from those incident near the zenith. Those primaries entering the atmosphere at grazing incidence so that their path would penetrate a few hundred g/cm^2 of air, can develop large cascades which then escape the atmosphere. These cascade showers are considered to be the dominant source of splash albedo electrons (49). As a result, we expect the splash albedo to be most intense at large zenith angles.

Those charged albedo particles with rigidity below the local geomagnetic cutoff cannot escape from the earth. They spiral along magnetic field lines and re-enter the atmosphere in the opposite hemisphere at a geomagnetic latitude nearly equal to the latitude where they originated (50). These particles constitute the "return albedo." The intensities of the splash and the return albedo below the local cutoff are expected to be equal at any point at the top of the atmosphere. This follows from the splash origin of the return albedo and the fact that the primary cosmic ray flux at a given geomagnetic latitude in the northern and southern hemispheres is the same. Treiman (50) has pointed out that the return albedo will tend to be less anisotropic than the splash albedo. Since the splash albedo is most intense at large zenith angles, the vertical splash albedo flux may be lower than the vertical return albedo flux, even though the total splash and return intensities, integrated over all directions, should be the same.

No detailed calculation of the intensity or spectrum of the albedo electrons has been published and only a few observations are available. Bland (49) has made a rough calculation for the purpose of deriving an upper limit to the intensity of return albedo electrons

near 45^{o} geomagnetic latitude. Verma (51) has measured the vertical splash and return albedo near Palestine, Texas, for electrons between 10 and 1100 MeV. He used a counter telescope which measured energy loss and range of incident particles. Schmoker and Earl (52) observed return albedo electrons between 50 and 150 MeV with a cloud chamber detector near Minneapolis and in Texas. At similar latitudes, McDonald and Webber (43) observed fast splash albedo which they attributed to electrons with range greater than 10 g/cm^2. We shall compare these calculations and observations with our results below.

No measurements of splash albedo electrons near Fort Churchill, other than ours, have been reported. Return albedo measurements at those high latitudes are complicated by the diurnal variation of the geomagnetic cutoff. We postpone discussion of the high latitude return albedo to section B, where we consider the diurnal variation.

2) Results

We present first the results of flight C3 with which we observed splash albedo electrons moving vertically upward. Figure 16 displays the altitude dependence of the rate of type 1 events and of types 2 and 3. The data points at 2.3 g/cm^2 atmospheric depth have the smallest statistical uncertainty because they represent averages over the 10.4-hour float period. The total data gathering time for all the other points was only 5.6 hours, the balloon ascent time. We could not plot similar results for events of type 4 because only four such events were observed during the entire flight, three during float and one during ascent.

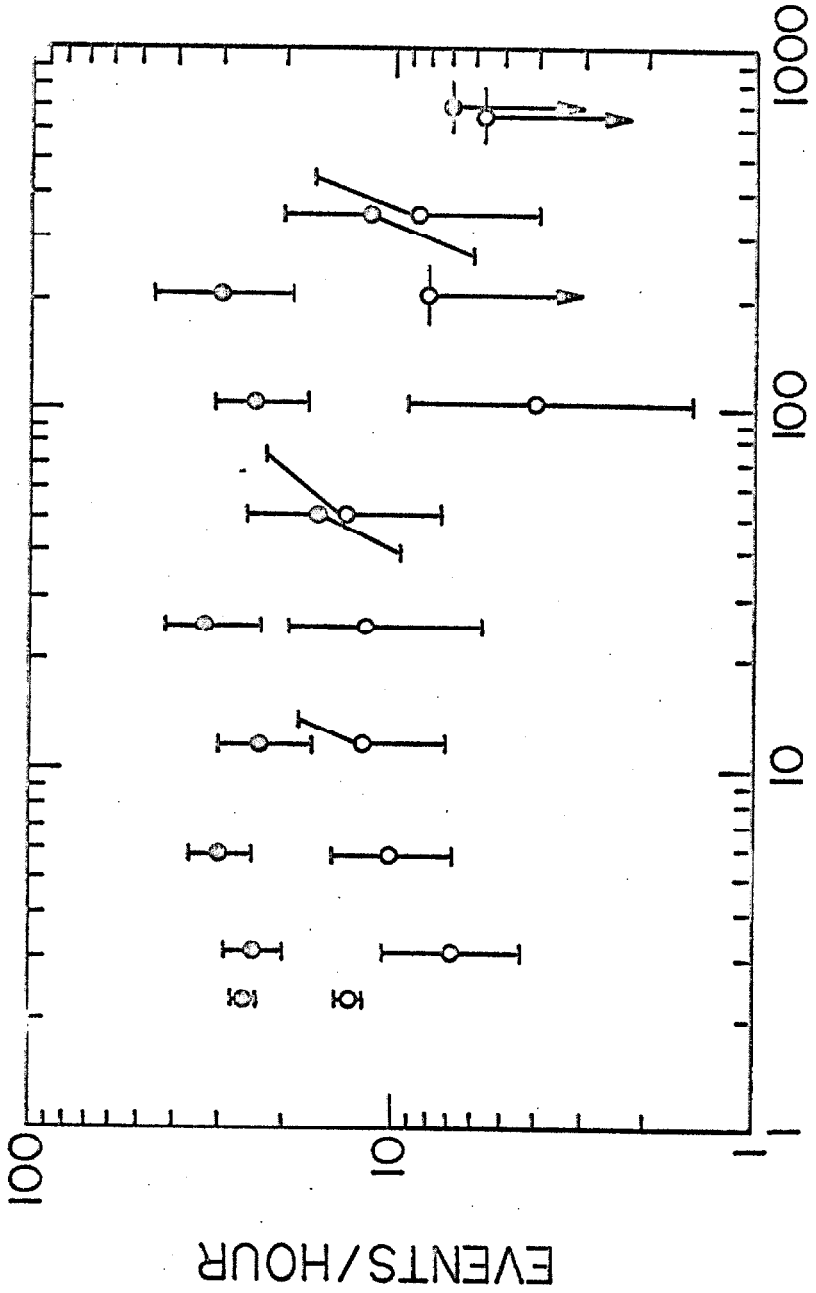

Fig. 16. Event rate vs. atmospheric depth for flight C3.
Solid circles - type 1 events.
Open circles - type 2 and 3 events.

It is apparent from Figure 16 that there is little or no altitude variation of the splash albedo between 2.3 g/cm^2 and 50 or 100 g/cm^2. We shall therefore assume that the electron energy spectrum which we observe at the detector at 2.3 g/cm^2 is the same as the spectrum at the top of the atmosphere. The number of events of each type observed during the float period of flight C3 is shown in Table 5. Applying the analysis described in Part IV, section B, we derive the flux values shown in Table 6A. The solid circles in Figure 17 indicate the differential energy spectrum derived from these measurements. The error limits quoted include statistical and systematic uncertainties.

To simplify comparison between our results and those of other experimenters, Table 6A indicates our fluxes summed over various energy intervals. In Table 6B we summarize the splash albedo results of other observers. We note that in all energy intervals our measured flux lies significantly below that of Verma (51). On the other hand, our flux above 50 MeV is in reasonable agreement with that of McDonald and Webber (43), and our flux above 100 MeV is consistent with the upper limit derived by Deney et al. (53).

Before further considering the splash albedo, we shall present results of the return albedo measurement made in flight P1, from Palestine, Texas. These results permit a more direct comparison with those of other observers because they are derived from data gathered at the same location.

The electrons observed with our detector are well below the geomagnetic cutoff rigidity near Palestine, so the particles we measured on this flight are a mixture of atmospheric secondaries, produced in the 5 g/cm^2 above the detector, and return albedo. No primary electrons could be observed.

TABLE 5

NUMBER OF ELECTRON EVENTS OBSERVED
DURING FLIGHTS C3 AND P1

Flight		C3	P1
Event type	1	212	152
	2	86	42
	3	21	15
	4	3	5
Sensitive time (min)		496	346

TABLE 6

SPLASH ALBEDO ELECTRONS

A) Flux of vertically moving, splash albedo electrons observed in flight C3 (electrons/m^2 sec sr) (Errors include statistical and systematic uncertainties)

Energy interval (MeV)	12 - 50	50 - 100	100 - 350	350 - 1000
Flux	94 ± 16	47 ± 11	27 ± 9	2^{+4}_{-2}
Combined flux, 12 - 100 MeV and 100 - 1000 MeV	141 ± 24		29 ± 10	
Flux between 50 and 1000 MeV	76 ± 16			

TABLE 6

SPLASH ALBEDO ELECTRONS

B) Flux of vertically moving, splash albedo electrons from other observers (electrons/m^2 sec sr)

Ref.	Date	Location	Cutoff[a] (GV)	Energy Interval (MeV)	Flux
51	1965	Palestine, Texas	4.5	10 - 100	467 ± 48
				100 - 300	134 ± 15
				300 - 1100	108 ± 18
43	1956	Iowa City	1.8	$\gtrsim$ 40[b]	84 ± 8
	1956	Minneapolis	1.4	$\gtrsim$ 40[b]	89 ± 8
53	1967	Palestine, Texas	4.5	> 100	<100

[a] Ref. 36.

[b] These electrons were identified only as having range greater than 10 g/cm^2. The corresponding energy is estimated from our own detector calibration at the Caltech synchrotron.

Fig. 17. Differential kinetic energy spectrum of splash albedo electrons.

Solid circles - present experiment, flight C3 Fort Churchill.

Open circles - Verma (51), Palestine, Texas.

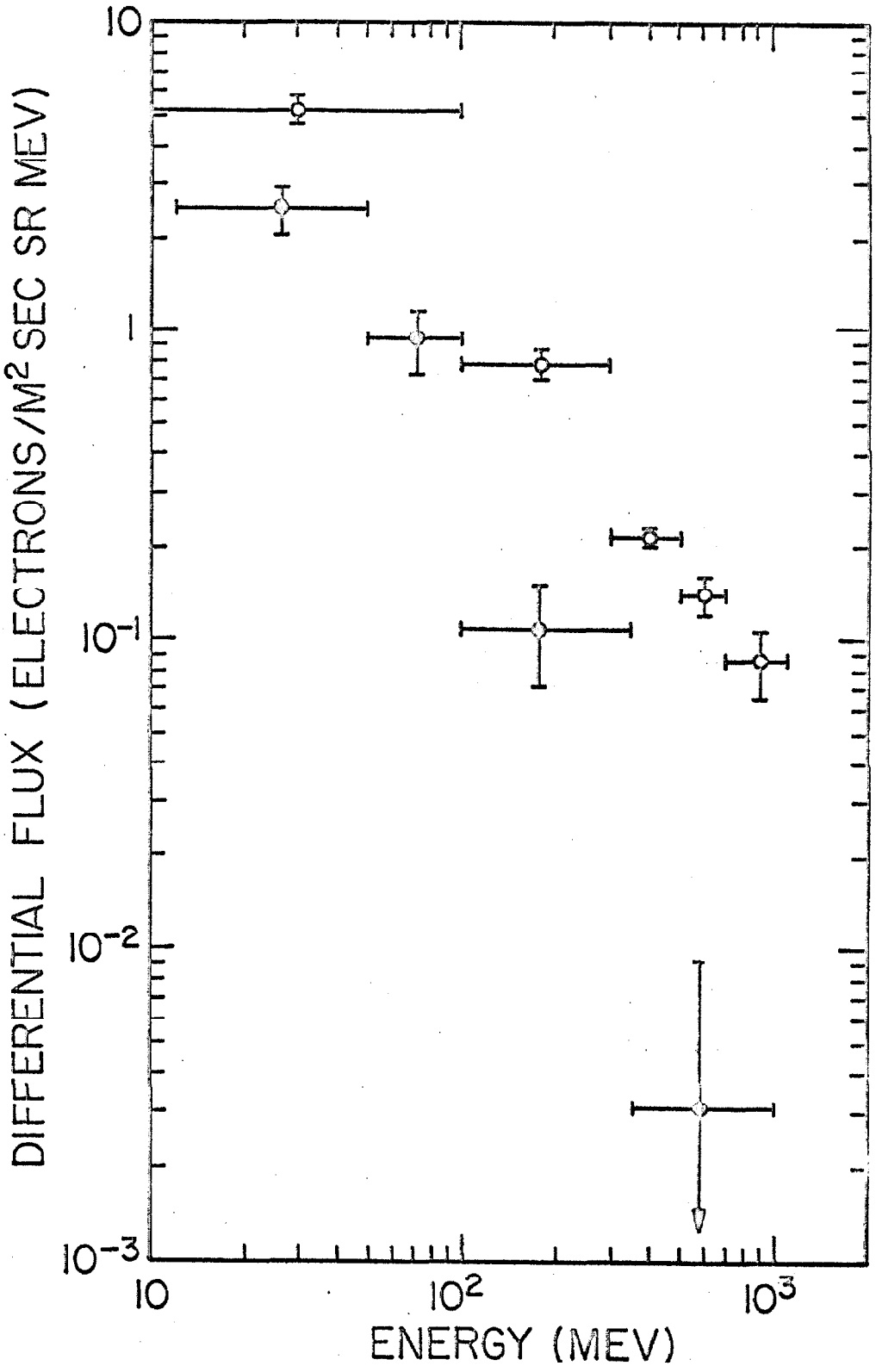
DIFFERENTIAL FLUX (ELECTRONS/M² SEC SR MEV)
10
1
10⁻¹
10⁻²
10⁻³
10
10²
10³
ENERGY (MEV)

Fig. 17

The number of events of each type observed during the float period of flight P1 is listed in Table 5. In Table 7A, line 2, we present the electron fluxes in various energy intervals derived from these events. Also shown, in line 3, is the flux of atmospheric secondary electrons expected at 5 g/cm^2 near Palestine. These secondary fluxes are derived from the calculation of Perola and Scarsi (44) with the addition of knock-on electrons (46). The corresponding differential energy spectra are plotted in Figure 18. The only energy interval with a clear excess over the secondaries is 12 to 50 MeV where the return albedo contribution is 60 ± 26 electrons/m^2 sec sr. For the other intervals, line 5 of Table 7A gives upper limits to the return albedo contribution. These limits represent two standard deviations of statistical uncertainties, plus the systematic uncertainty.

For comparison between the return and splash albedo it is necessary to take account of the energy loss of the return albedo electrons between the top of the atmosphere and the detector. Using calculated values of electron range in air, including energy loss of both ionization and radiation (54), we derive the tabulated energy intervals at the top of the atmosphere. In the last line of Table 7A, we list the splash albedo fluxes from flight C3 in these higher energy intervals. We derive these flux values from those of Table 6A, using the observed differential splash albedo spectrum from Figure 17.

For further comparison, Table 7B lists results from return albedo measurements by other observers. These results are also plotted in Figure 18. Again we note a significant disagreement between our results and those of Verma.

TABLE 7

RETURN ALBEDO

A) Flux of electrons moving vertically downward in flight P1. (electrons/m^2 sec sr)
(Errors include statistical and systematic uncertainties)

1. Energy interval at detector (MeV)	12 - 50	50 - 100	100 - 350	350 - 1000
2. Total observed flux at 5.2 g/cm^2	95 ± 19	29 ± 9	31 ± 14	8^{+8}_{-4}
3. Calculated flux of atmospheric secondaries	35 ± 7	26 ± 5	50 ± 10	17 ± 3
4. Return albedo flux	60 ± 26			
5. Return albedo upper limit	(96)	22	12	6
6. Energy interval at the top of the atmosphere (MeV)	25 - 65	65 - 131	131 - 411	411 - 1149
7. Splash albedo flux from flight C3 in these higher energy intervals	63 ± 11	44 ± 10	13 ± 4	< 5

TABLE 7

RETURN ALBEDO

B) Flux of electrons moving vertically downward, from other observers. (electrons/m^2 sec sr)

Ref.	Date	Location	Cutoff (GV)	Atmospheric depth (g/cm^2)	Energy Interval (MeV)	Flux
51	1965	Palestine, Texas	4.5	4.0	10 - 100 100 - 300 300 - 1100	162 ± 16 90 ± 30 68 ± 10
52	1962	San Angelo, Texas	5.0	6	45 - 150	140 ± 70
52	1962 & 63	Minneapolis	1.4	4-5	45 - 150	180 ± 60

Fig. 18. Differential kinetic energy spectrum of downward moving electrons below geomagnetic cutoff. Data points indicate total observed flux, including return albedo and atmospheric secondaries. Solid curve indicates calculated spectrum of atmospheric secondaries at 5 g/cm^2 atmospheric depth. Dashed curves indicate quoted uncertainty in this calculated spectrum ($\pm$ 20%).

Solid circles - present experiment, flight P1, Palestine, Texas, 5 g/cm^2.

Open circles - Verma (51), Palestine, Texas, 4 g/cm^2.

Solid line diamond - Schmoker and Earl (52), San Angelo, Texas, 6 g/cm^2.

Dashed line diamond - Schmoka and Earl (52), Minneapolis, Minn., 4-5 g/cm^2.

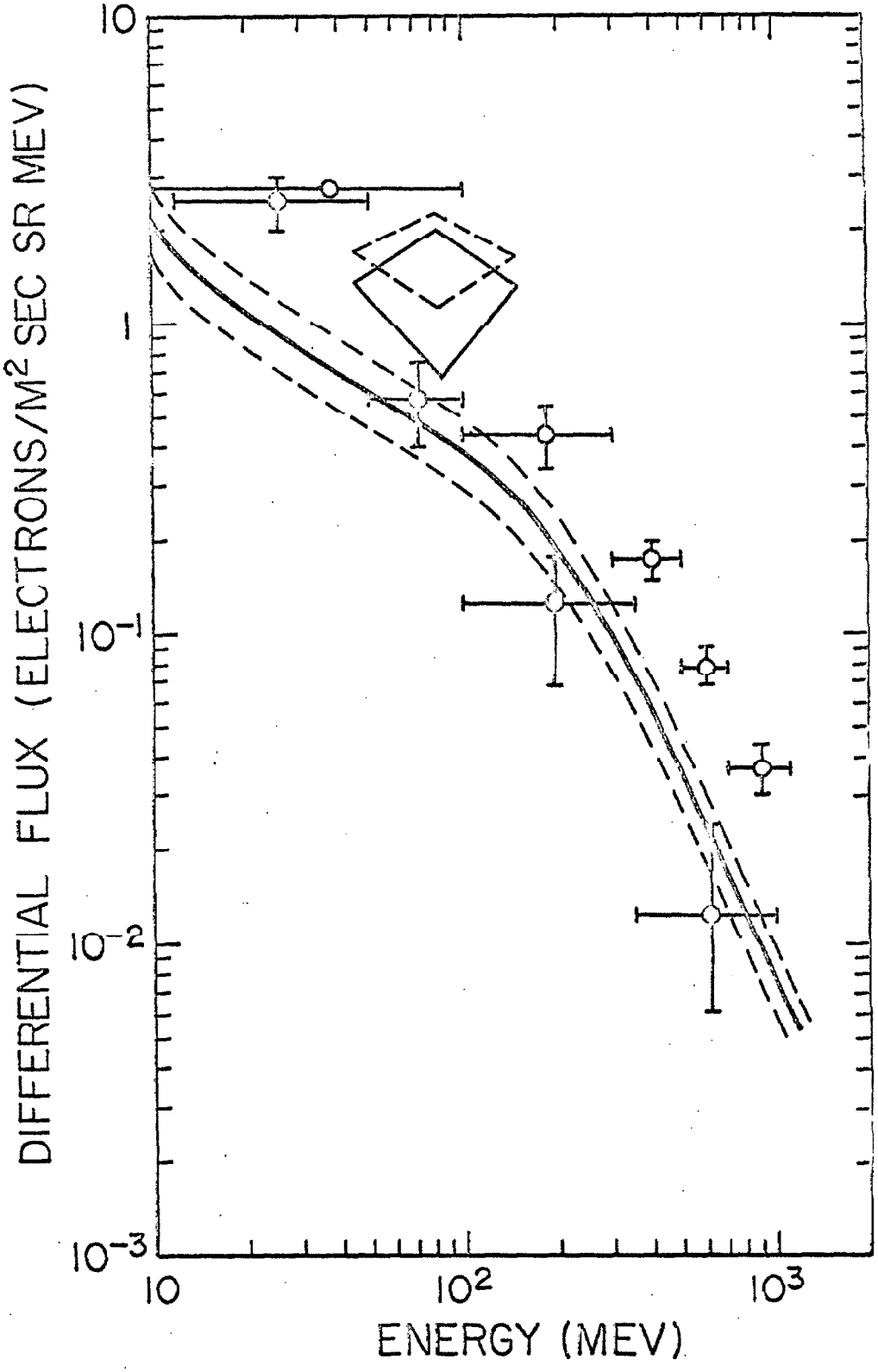
DIFFERENTIAL FLUX (ELECTRONS/M² SEC SR MEV)
10
1
10⁻¹
10⁻²
10⁻³
10
10²
10³
ENERGY (MEV)

Fig. 18

3) Discussion

We first compare our return albedo measurement near Palestine, Texas, with Verma's. His measurement was made on two balloon flights also launched at Palestine, and the float altitude of his flights (4.0 g/cm^2) was not very different from that of ours (5.2 g/cm^2).

The two-year time difference between Verma's flights and ours can account for only a small part of the difference in results. From 1965, when his data were taken, to the time of our flights the Mt. Washington neutron monitor count rate decreased by 9 percent. The corresponding decrease in the flux of cosmic ray protons and helium nuclei above the geomagnetic cutoff at Palestine (4.5 GV) is 10 percent. (This number is based upon regression curves of data from the last solar cycle, reference 55.) The corresponding decrease in the albedo intensity must be $\leq$ 10 percent. This upper limit follows because the change in primary flux is largest at the lowest energy while the electron production by electromagnetic cascades is larger at higher primary energies. A 10 percent reduction in Verma's flux between 10 and 100 MeV would bring it within the quoted error of our result. For energies above 100 MeV, however, the difference between his results and ours remains significant.

We must therefore conclude that there is a systematic error in either Verma's or our measurements. His flux would be high if some component of the background radiation could cause events which simulate electrons. In this regard, we note that the geometry of his detector system is similar to ours: two telescope counters define an incident beam, and below the telescope is a stack of lead plates with detectors interspersed. There are, however, two

significant differences between his system and ours. Although he has side and bottom guard counters, similar to ours, he has no top guard counter. Also, he has no directional element in his telescope, comparable to our Čerenkov counter. Thus his system is more sensitive than ours to radiation which enters the detector outside the acceptance cone and interacts in the lead, producing a particle moving up through the telescope.

Another possible source of systematic error is in the determination of the detection efficiency - in particular, the probability that an incident electron causes a shower which triggers a guard counter. We do not believe our efficiency determination is in error. We measured the efficiency at the Caltech synchrotron both before and after our flights and derived consistent results. Furthermore, in the energy interval between 350 and 1000 MeV, our return albedo flux is at least a factor of four below Verma's, while in the same energy interval, our primary flux measurements at Churchill in 1967 are less than a factor of two below published measurements for 1966; and this factor may be due to modulation. (See Section C.)

We may also compare our return albedo measurement with the results of Bland (49). He has published a rough calculation of the return albedo flux at 4 g/cm^2 atmospheric depth, 45^o geomagnetic latitude. His result, as an upper limit to the flux of electrons above 100 MeV, is 14 electrons/m^2 sec. If the electrons are isotropic over the upper hemisphere, this would correspond to 2.2 electrons/m^2 sec sr. This flux is consistent with our upper limit, 18 electrons/m^2 sec sr, after subtracting atmospheric secondaries. Verma, on the other hand, derives a corresponding value of 94 ± 25 electrons/m^2 sec sr.

We turn next to our measurement of the splash albedo near Fort Churchill. Both the location and the time of the measurement by McDonald and Webber near Minneapolis (43) enable us to compare their result with ours. The geomagnetic cutoff at Minneapolis, 1.4 GV, corresponds to a proton energy of 750 MeV. The difference between this cutoff and that near Churchill, < 350 MV, is not significant for the production of albedo electrons. (The pion production cross-section in air is nearly independent of incident proton energy above 800 MeV but falls sharply below 800 MeV, reaching zero near 300 MeV (44). Also, the flux of protons between 300 and 750 MeV is less than 20 percent of the flux above 750 MeV.) At the time of the Minneapolis flight, the Mt. Washington neutron monitor count rate was 2302, 0.7 percent higher than during our flight C3. This corresponds to a 6 percent difference in the primary proton flux (55) and less than 6 percent in the albedo flux. The albedo flux measured by McDonald and Webber, 84 ± 8 electrons/m^2 sec sr, is in good agreement with our flux above 50 MeV, 76 ± 16 electrons/m^2 sec sr.

We cannot attempt to draw any conclusion about the latitude dependence of the splash albedo from comparison of our results with Verma's because of the instrumental differences previously noted. We shall, however, compare our own return albedo measurement near Palestine with our splash albedo observation near Churchill (lines 4 - 7 of Table 7A).

Between 65 and 131 MeV the Churchill splash albedo exceeds the Palestine return albedo by at least 50 percent. In the other energy intervals, no clear difference between the two observations can be proven, although a 50 percent excess at Churchill is consistent with the data. We expect that the vertically moving splash albedo should be less than or equal to the return albedo flux. Therefore, the

Churchill excess indicates that primary cosmic rays below 4.5 GV contribute significantly to the production of splash albedo electrons, at least at electron energies below 130 MeV. Since the flux of primaries below 4.5 GV undergoes strong modulation over the solar cycle, we predict that the splash albedo at high latitudes would show a similar strong variation during the eleven-year cycle.

This conclusion could be verified by observation of the high latitude splash albedo over a period of several years. Also, direct observation of the splash albedo with the same detector at various latitudes would be useful.

B) Diurnal variation

1) Background

A diurnal variation in the flux of low energy electrons was first observed by Jokipii, L'Heureux, and Meyer (29). Their results were based upon five balloon flights of an electron detector, launched from Fort Churchill during 1965 and 1966. Near 0600 local time on each flight they observed an increase in the flux of electrons between 10 and 220 MeV. The daytime flux was higher than the nighttime flux by at least a factor of two. Above 220 MeV the electron intensity showed no temporal variation.

These authors explain this increase as the effect of a diurnal change in the geomagnetic cutoff. They suggest that at night the cut-off is near or below their detector threshold, and during the day it is significantly higher than this, perhaps near 200 MV. As a result, the electrons observed at night are primary particles (plus atmospheric secondaries produced above the detector). During the day, the primary electrons are replaced by return albedo. The difference

between the day and night fluxes reflects the difference between the intensities of return albedo and primary electrons.

The diurnal cutoff variation may be explained by considering a realistic model of the earth's magnetic field. (For a recent review of the observed properties of the magnetosphere, see reference 56.) The salient features of the model for our discussions are:

a) termination of the geomagnetic field on the sunlit side of the earth by a blunt surface, about 10 earth radii (R_e) from the center of the earth at the subsolar point;

b) confinement of the field on the night side of the earth within an approximately cylindrical "tail" with radius about 20 R_e and axis in the anti-solar direction;

c) presence within the tail of a current sheet in, or parallel to, the plane of the ecliptic, extending into the tail from a line about 10 R_e from the earth.

A model field based upon these properties of the geomagnetic field has been constructed by Williams and Mead (57). The field lines in their model are shown in Figure 19. Both the tilt of the geographic axis with respect to the ecliptic plane and the tilt of the geomagnetic dipole with respect to the geographic axis are ignored; only the dipole term of the internal field is included. The surface of the earth in this model may be divided into three zones. At low dipole latitudes, $\leq 68^{\circ}$, the field lines are simply connected, essentially dipole lines on both the day and night sides of the earth. At high latitudes, $\geq 80^{\circ}$, the field lines are unlike dipole lines at any time of day or night; they sweep far back into the tail. At intermediate latitudes, 68° to 80°, the field line which intersects the surface of the earth at any point changes character as the earth rotates. On the day side the line is

Fig. 19. Geomagnetic field lines in the model of Williams and Mead (57). Units along the axis are earth radii. Field lines are labeled by the geomagnetic latitude at which the lines intersect the surface of the earth.

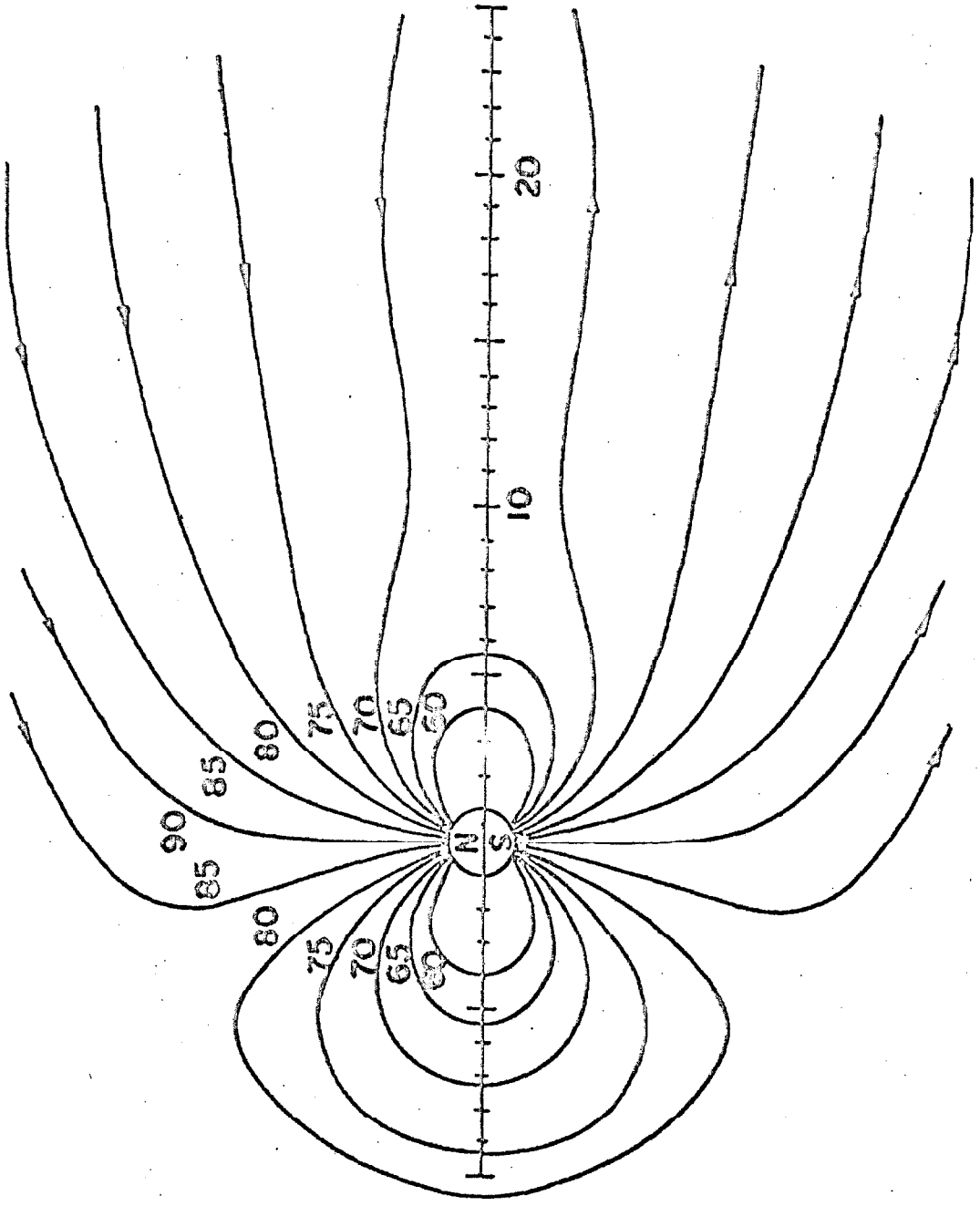

Fig. 19

simply connected, similar in shape to the lines at lower latitudes; but on the night side it extends far into the tail, like the high latitude field lines.

On the basis of both theory (58) (59) and observations (60), there is reason to believe that interplanetary particles have essentially free access to the magnetospheric tail. Once inside the tail, they can travel along the field lines to the surface of the earth. Thus, points on the surface intersected by field lines from the tail should have no geomagnetic cutoff. Splash albedo may readily escape from the magnetosphere, and primary particles are free to impinge on the atmosphere. On the other hand, points at the foot of simply closed field lines have cutoffs similar to the values calculated on the basis of the earth's internal field only. In the intermediate latitude zone, the cutoff at any point would change from zero to near the internal field value as the earth rotates, carrying the point from the night to the day side.

The diurnal variation of geomagnetic cutoffs, as described above, was first suggested by Reid and Sauer (61). Subsequently, Taylor (62) and Gall, Jimenez, and Camacho (63) computed cutoffs at various latitudes and local times by numerical integration of charged particle orbits in the Williams and Mead model magnetosphere, or a similar model. We shall compare their results with our observations below, in Section B3.

The calculations of Gall et al. show that in addition to the depression of the vertical cutoff at midnight, the magnetospheric tail also depresses the noon cutoff. The depression at noon is not as large as at midnight, so a diurnal variation in the cutoff does occur, as described above. The depression of the daytime cutoff is due to particles entering the magnetospheric tail on a trajectory

which carries them around to the daytime side of the magnetosphere before striking the earth. (See Figure 3 of reference 63.) Such particles reach the day side of the earth even though their rigidity is so low that they could not reach the earth by penetrating the sunward side of the magnetosphere. Conversely, splash albedo particles of the same rigidity from the day side of the earth drift around the earth onto tail field lines and then escape, without returning to the earth.

Experimental evidence for the diurnal variation of geomagnetic cutoffs at rigidities ≥ 50 MV has also been derived from satellite observations of low energy protons (30) (31). The electron measurements allow us to extend these studies to lower rigidities, below 20 MV.

The observations of the diurnal electron flux variation by Jokipii et al. suffered from a complete lack of energy resolution between 10 and 220 MeV. Also, their detector was never at float altitude late enough in the evening to observe the transition from daytime to nighttime flux. Our results, presented below, have better energy resolution than those of Jokipii et al. and include an observation of the evening step in addition to three observations of the morning step. Another observation of the evening transition has recently been reported by Webber (16) and shall be included in our later discussion. An important aspect of our data, unlike those of earlier observers, is that we have measurements of both the diurnally varying, downward-moving flux and of the splash albedo. These data were gathered with the same detector, near the same location, within one month, and so permit a direct comparison. The results of this comparison lend strong support to the above explanation of the diurnal variation.

2) Results

The clearest evidence of a diurnal flux variation occurs for our events of type 1, electrons of approximately 12 to 50 MeV. The first three curves of Figure 20 display the rate of these events during the float periods of flights C1, C2, and C4. These are the flights in which the detector was oriented toward the zenith. The dashed curves indicate the atmospheric secondary contribution, based upon the calculations of Perola and Scarsi (Curve 1 of Figure 15 in Part IV). Variations in the secondary flux reflect changes in the balloon altitude.

The first two intervals plotted for flight C1 represent data gathered during the last seventy minutes of ascent. They are included in this plot to indicate the morning transition, which fortuitously occurred just as the balloon reached float altitude. This is the latest recorded occurrence of the morning step, and this flight is the first to record both a morning flux increase and an evening decrease. In the data of flights C2 and C4 the morning step is also apparent, occurring earlier and less sharply than in C1. Flights C2 and C4 were terminated before the evening transition.

For comparison, the bottom curve in Figure 20 gives the rate of type 1 events observed during flight C3, when the detector was oriented toward the nadir to observe splash albedo. This plot displays no transition comparable to the steps during the other flights. We expect no transition because the primary cosmic rays responsible for the albedo electrons have rigidity above 0.8 GV, substantially higher than the internal field geomagnetic cutoff along our flight trajectories.

In Figures 21, 22, and 23 we plot the time dependence of the event rate for each of the four types of electron events. The

Fig. 20. Type 1 event rate vs. local time at the detector, during flights C1, C2, C4, and C3.

Solid line - observed event rate. Error bars indicate typical statistical errors.

Dashed line - calculated rate due to atmospheric secondary electrons.

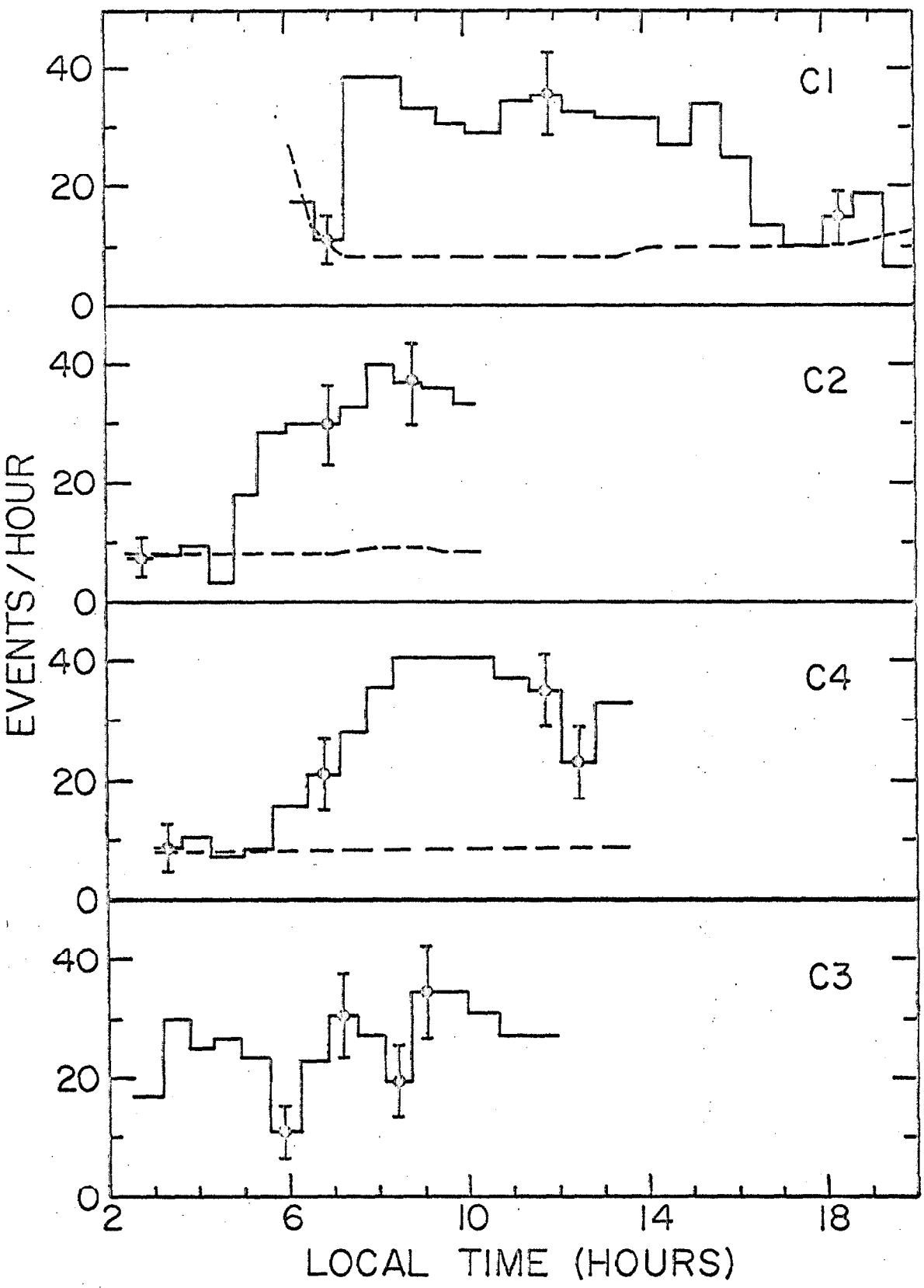

Fig. 20

Fig. 21. Flight C1. Rate of electron events of type 1, 2, 3, 4 and proton events (type P) vs. local time at the detector. Typical statistical errors are shown.

Fig. 22. Flight C2. See caption of Figure 21.

Fig. 23. Flight C4. See caption of Figure 21. In addition events of type 0 are plotted. These events satisfy the criteria of type 1 except for the lack of a Čerenkov counter signal.

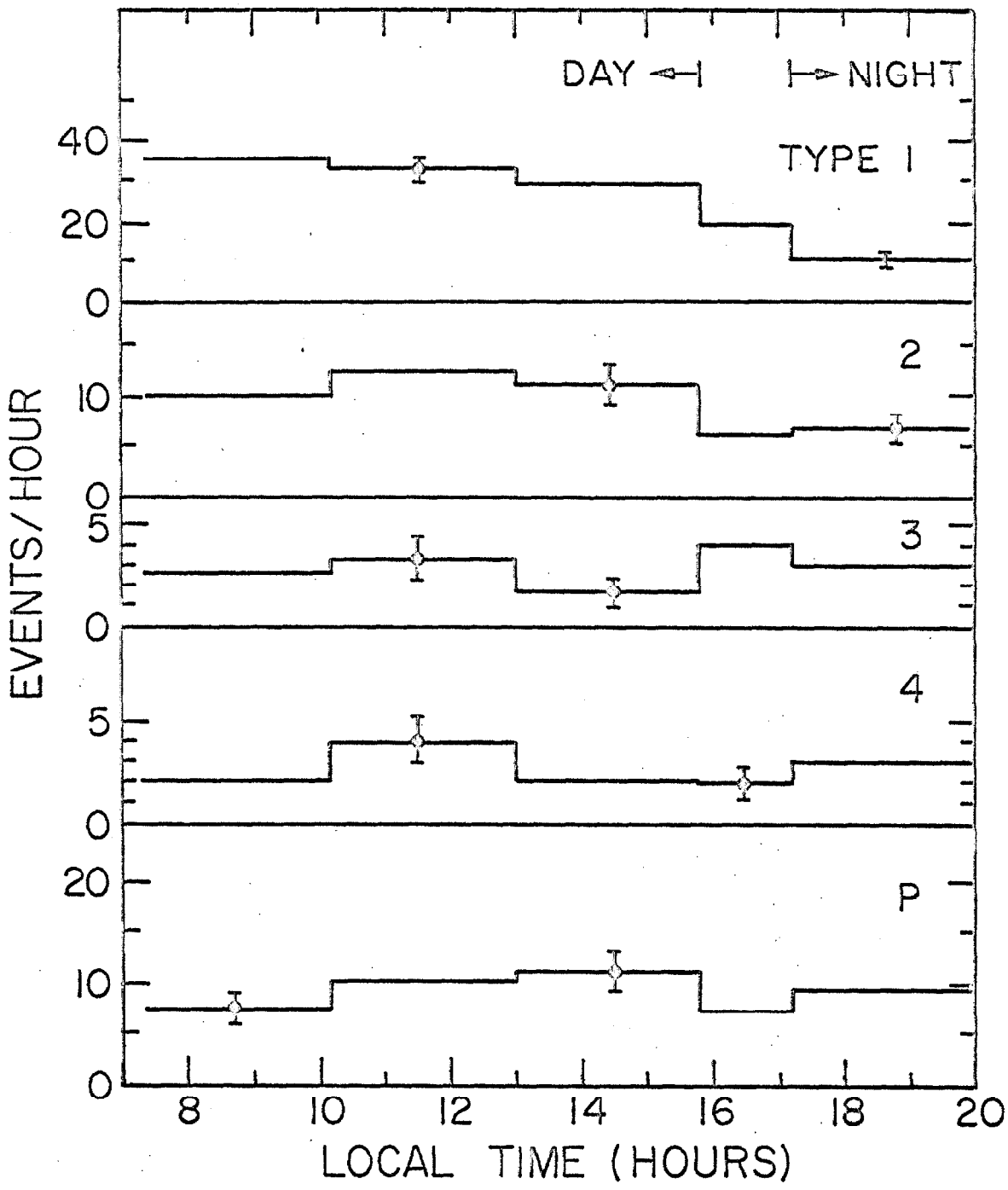
DAY
NIGHT
TYPE 1
2
3
4
P
EVENTS/HOUR
40
20
0
10
0
50
0
5
0
5
0
20
10
0
8
10
12
14
16
18
20
LOCAL TIME (HOURS)

Fig. 21

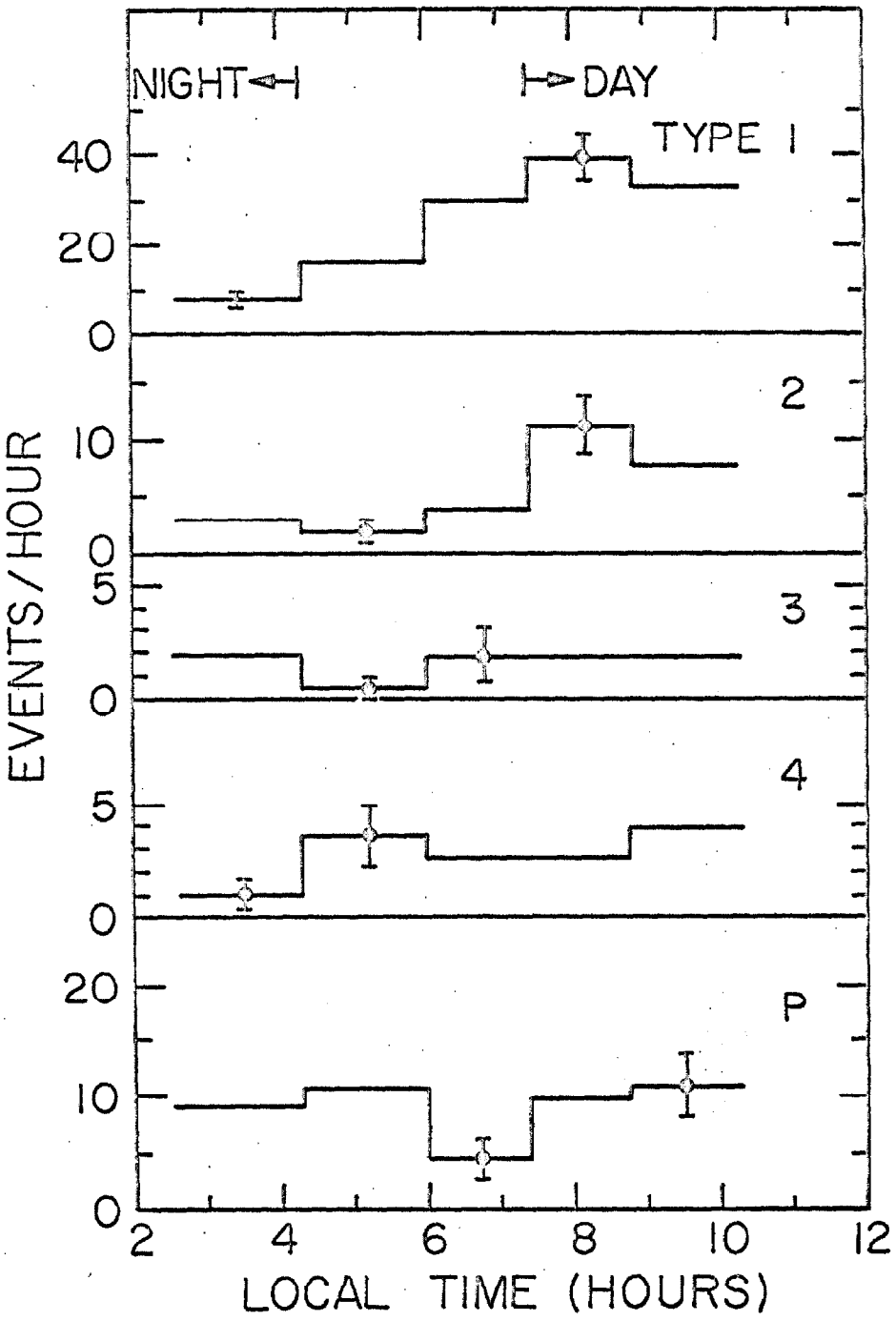
NIGHT
DAY
TYPE 1
2
3
4
P
EVENTS/HOUR
40
20
0
10
0
5
0
5
0
20
10
0
2
4
6
8
10
12
LOCAL TIME (HOURS)

Fig. 22

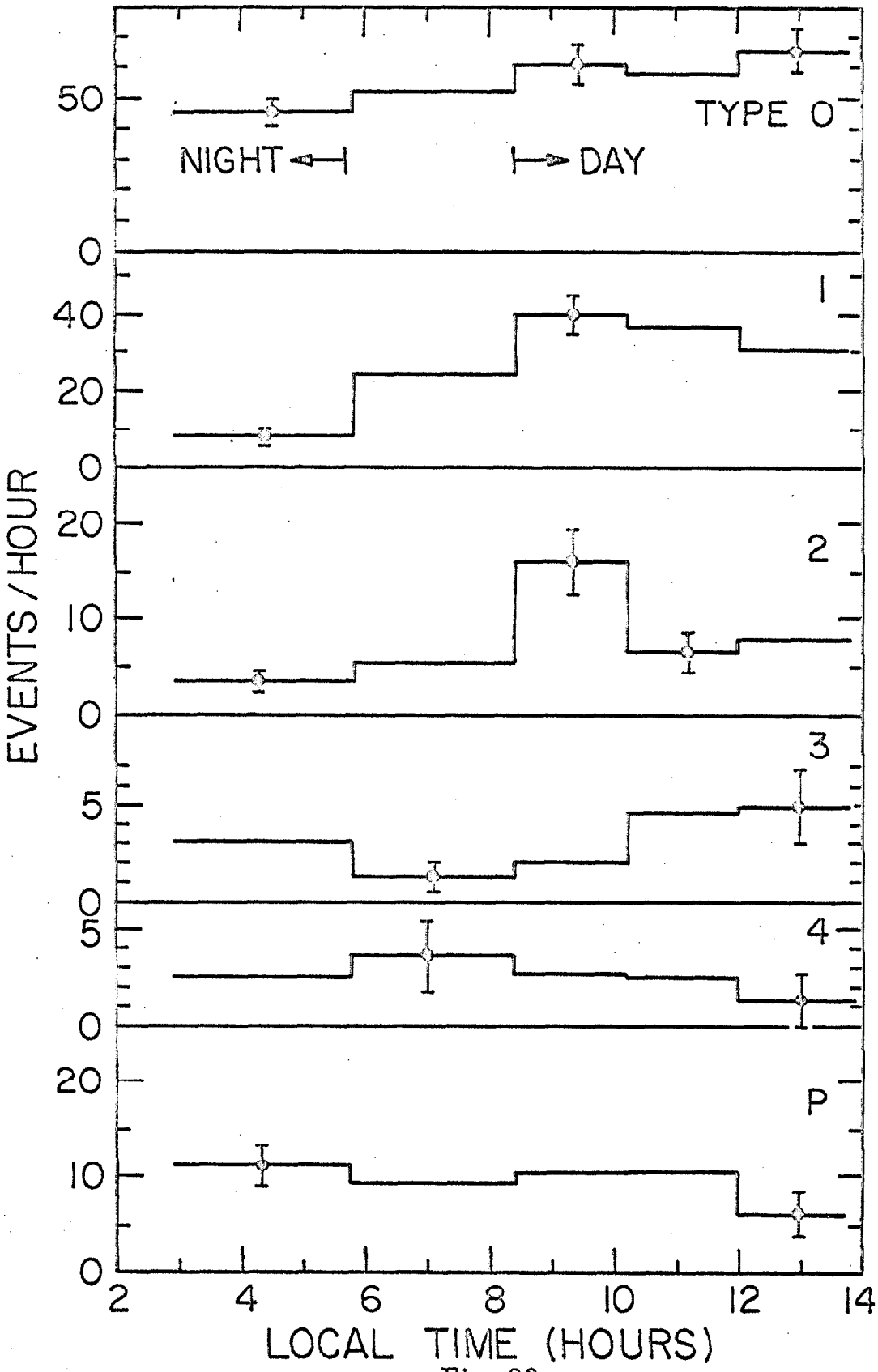

Fig. 23

counting statistics for type 2 events are not as good as for type 1 and the flux variation is not as large, but an evening transition is apparent during flight C1 and a morning transition in C2. There may be a similar transition in C4, but it is not as obvious.

The event rates for types 3 and 4 display no significant diurnal flux variation. This fact, as well as the lack of a flux transition in flight C3, indicates that the transitions in the flux of low energy electrons observed on flights C1, C2, and C4 are not instrumental effects. Additional evidence that the detector response did not vary during the flights comes from the observed flux of very high energy protons. The bottom plot, labeled P, in Figures 21, 22, and 23 displays the rate of events satisfying the following criteria:

a) Čerenkov counter signal accompanies the event.

b) Both energy loss counters register a pulse height corresponding to energy loss between 0.5 and 1.7 I_o.

c) No guard counter signal accompanies the event.

d) The spark chamber contains a single straight track.

These events record protons above 16 GeV which do not interact in the detector. Because of their very high rigidity, we expect the flux of these protons to display no temporal variation.

In Figure 23, we also plot, as type 0, events satisfying all criteria for type 1 except for the lack of a Čerenkov signal. These are electrons of approximately 4 to 12 MeV - i.e., they have sufficient energy to penetrate the telescope counters, but their energy is below the Čerenkov counter's effective threshold. We expect a larg fraction of these events to be due to atmospheric secondary gamma

which pair-produce or Compton-scatter in the first lead plate and produce an upward-moving electron that triggers the telescope. Because of the large background, it is difficult to derive a meaningful absolute electron flux from these events. However, we expect the background to be constant, so the change in count rate observed between 0600 and 0800 local time indicates that the diurnal variation does occur for electrons whose energy at the detector is below 12 MeV.

Table 8 summarizes the observed rates for each type of event. We tabulate rates for night and day intervals, as well as for the entire float periods. The arrows at the top of Figures 21, 22, and 23 indicate the data used for the night and day parts of this tabulation. These data were selected to include only time intervals when both type 1 and type 2 event rates were within one standard deviation of their mean night or day values. The rates shown in Table 8 verify our previous qualitative statements, that events of types 0, 1 and 2 have a clear diurnal variation, while events of types 3, 4, and P have no statistically significant variation.

3) Discussion

Our data permit a direct comparison between the diurnally varying flux of downward-moving electrons and the splash albedo electrons near the same location. The mean daytime type 1 rate in flights C1, C2, and C4 is 35 ± 1.5 events/hour. Subtracting our best estimate of the atmospheric secondary contribution (Fig. 20) leaves 26.8 ± 1.5 events/hour as the rate due to electrons incident at the top of the atmosphere. This value is in good agreement with the corresponding splash albedo rate 25.6 ± 1.8 events/hour. The

TABLE 8

EVENT RATES

(Rates are expressed as events/hour. Only statistical uncertainty is indicated)

Event Type	Interval (a)	Flight C1	C2	C4	C3
0	N			45.1 ±4.4	
	D			59.4 ± 3.6	
1	N	10.7 ± 1.9	8.1 ± 2.0	8.7 ± 1.9	-
	D	33.0 ± 1.9	39.0 ± 3.6	36.4 ± 2.9	-
	F	-	-	-	25.6 ± 1.8
2	N	6.9 ±1.5	3.1 ±1.2	3.5 ±1.2	-
	D	11.4 ±1.1	9.6 ±1.8	10.2 ±1.4	-
	F	-	-	-	10.4 ± 1.1
3(b)	N	3.1 ±1.0	2.0 ±1.0	3.0 ± 1.1	-
	D	2.7 ±0.6	2.0 ±0.8	3.9 ± 1.0	-
	F	3.0 ±0.5	1.7 ±0.4	3.1 ± 0.6	2.5 ±0.6
4(b)	N	3.1 ±1.0	1.0 ±0.7	1.3 ±0.7	-
	D	2.7 ±0.6	3.3 ±1.0	1.2 ±0.5	-
	F	2.7 ±0.5	2.7 ±0.6	1.4 ±0.4	0.36±0.21
P	N	9.6 ±1.8	9.2 ±2.2	11.3 ±2.2	-
	D	9.8 ±1.1	10.6 ±1.9	9.2 ±1.5	-
	F	9.5 ±0.8	9.3 ±1.1	9.8 ±1.1	-

(a) N - night interval
D - day interval
F - entire float period, including night, day, and intermediate intervals.

(b) Note that in flight C4 the calibration for events of type 3 and 4 are different from corresponding calibrations for other flights. See Figures 12 and 13, in Part IV.

agreement supports the model described in Section B1, in which the high daytime flux of electrons is return albedo.

Further support for the model comes from the observation that the nighttime flux is significantly lower than the splash albedo. As shown in Part IV, Section F, the nighttime type 1 event rate is consistent with the rate expected from atmospheric secondaries alone; an upper limit to the contribution from electrons incident at the top of the atmosphere is 3.9 events/hour. By assuming there are no primary electrons, 3.9 events/hour gives an upper limit to the return albedo. Thus the return albedo at night is less than 15 percent of the splash albedo, and in fact may be zero. This lack of return albedo at night over a wide range of local times provides strong support for the model in which the nighttime flux (after subtracting atmospheric secondaries) is the full primary flux. We know of no mechanism by which both return albedo and primaries can be excluded from the observations. The lack of return albedo indicates that the splash albedo escape from the earth; primary particles must be able to travel similar trajectories in the opposite direction and reach the earth.

We derive an upper limit to the nighttime cutoff rigidity in the following manner: We treat the events of type 1 as being electrons with energy between 12 and 50 MeV at the detector. This interval corresponds to 17 to 57 MeV at the top of the atmosphere. We assume that the daytime count rate, after subtracting atmospheric secondaries, represents the flux of return albedo between 17 and 57 MeV, while the corresponding nighttime count rate represents return albedo between 17 MeV and E_n, the electron energy corresponding to the nighttime cutoff. Let $j(E)$ be the differential energy

spectrum of return albedo; r_d and r_n are the daytime and nighttime count rates for events of type 1 (after subtracting secondaries). Then

$$\frac{\int_{17}^{E_n} j(E)dE}{\int_{17}^{57} j(E)dE} = \frac{r_n}{r_d} \qquad (5)$$

We take $j(E) = KE^{-1}$ in accordance with the splash albedo spectrum below 100 MeV (Fig. 17). This gives

$$E_n = (17\ \text{MeV}) \exp\left[\frac{r_n}{r_d} \ln \frac{57}{17}\right] \qquad (6)$$

taking $r_d = 26.8$ events/hour and $r_n \leq 3.9$ events/hour, we derive $E_n \leq 20$ MeV.

We may further lower this estimate for the nighttime cutoff by considering the type 0 events (Fig. 23). The change in count rate indicates that the nighttime cutoff lies somewhere in or below the interval 4 to 12 MeV. Since 12 MeV at the detector corresponds to 17 MeV at the top of the atmosphere, we conclude that the nighttime cutoff rigidity is below 17 MV.

To estimate the daytime cutoff energy, E_d, we assume that the daytime energy spectrum has a discontinuity at E_d', the electron energy at the detector corresponding to E_d at the top of the atmosphere Electrons with energy above E_d' are above the cutoff at all times, day and night, so we take the spectrum above E_d' to be the

same as the nighttime spectrum derived in Section C. Below E'_d the daytime spectrum is the sum of return albedo and atmospheric secondaries. We estimate the return albedo spectrum as equal to our splash albedo spectrum of Section A, (Fig. 17). We then calculate, for various values of E_d, the ratio of daytime to nighttime count rates for each type of electron event. We find that the observed day/night ratio for type 3 events, 1.05 ± 0.28, is inconsistent with the calculated ratio if $E_d > 110$ MeV. On the other hand, the observed day/night ratio of type 2 events in flights C2 and C4, 3.25 ± 0.95, is inconsistent with the calculated ratio if $E_d < 70$ MeV. We thus estimate that the geomagnetic cutoff rigidity during the day lies between 70 and 110 MV.

In Figure 24 we compare the cutoff rigidities derived above with those of other experiments and calculations. The daytime cutoffs observed in this experiment and by Stone and Webber are in qualitative agreement with Gall's calculation, showing a sharp decrease in the daytime cutoff near 70° latitude. However, these experimental data show that this decrease occurs near 68° rather than 70° as calculated by Gall. Our nighttime cutoff upper limit, which is valid at latitudes as low as 67°, is in qualitative agreement with Gall but extends about 2° lower in latitude than her calculations predict. Our nighttime result is consistent with those of other experimenters, and is also consistent with the calculation of Reid and Sauer and that of Taylor.

We do not consider that the discrepancy between the observed cutoffs and those calculated by Gall is serious. Similarly, the discrepancies among the various calculations are not serious. Each of these calculations uses a highly idealized model of the

Fig. 24. Geomagnetic cutoff rigidity vs. geomagnetic dipole latitude The curves represent calculated vertical cutoff rigidities (R_c).

Curve 1 - internal field, $R_c = 14.9 \text{ GV} \cos^4 \lambda$.

Curve 2 - noon cutoff, Gall et al. (63).

Curve 3 - midnight cutoff, Gall et al.

Curve 4 - midnight cutoff, Reid and Sauer (61).

The crosses indicate the noon and midnight cutoffs calculated for particles incident parallel to the local field lines, Taylor (62). Experimental results (Open symbols represents daytime cutoffs; solid symbols, nighttime cutoffs.)

Circles - this work.

Triangles - Stone (30).

Diamonds - Paulikas et al. (31).

Squares - Webber (16).

The calculations assume that the internal field of the earth is a simple dipole; the latitude shown is the dipole latitude. Our experimental points are plotted at a latitude, λ, defined by $R_c = 14.9 \text{ GV} \cos^4 \lambda$ where R_c is the cutoff calculated on the basis of the real internal field (36). This is equivalent to the definition of latitude used by the other experimenters.

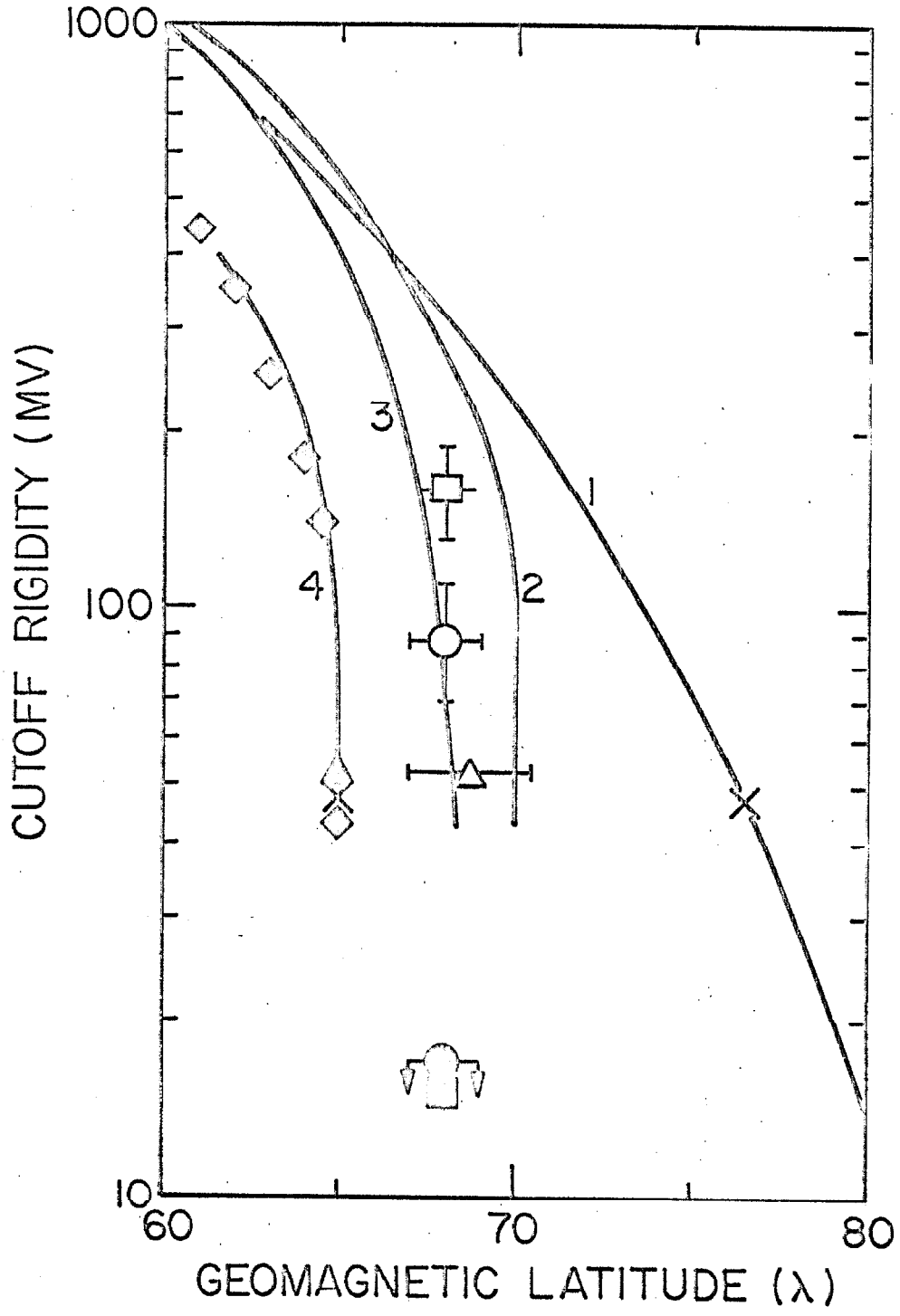
1000
100
10
CUTOFF RIGIDITY (MV)
60
70
80
GEOMAGNETIC LATITUDE (λ)
1
2
3
4

Fig. 24

magnetosphere in which the earth's internal field is taken as a simple dipole; the dipole axis and the geographic axis are both assumed to be perpendicular to the ecliptic plane. Different values of the position and field strength of the neutral sheet are used in each calculation, and the true values of these parameters are not yet accurately known. We must conclude that the qualitative agreement between the measured and calculated cutoff behavior supports the basic properties of the model.

Further qualitative agreement with the model comes from consideration of the times at which the flux transition occurs. In Figure 25 we indicate the trajectories of flights C1, C2, and C4 in a coordinate system of geomagnetic latitude vs. local time. Along each trajectory we indicate when the type 1 event rate was within one standard deviation of its day or night value (from Fig. 20). It appears that the geomagnetic cutoff remains below 20 MV later in the morning at higher latitudes. This is qualitatively reasonable because at sufficiently high latitudes ($> 70^{o}$ in Gall's model) the cutoff would remain below 20 MV at all times. It would not be appropriate to make any detailed, quantitative conclusions from the results in Figure 25. In most cases the counting statistics introduce at least a half hour uncertainty in the time of a flux change. Furthermore, the three flights occurred over a period of a month, and changes in the detailed configuration of the magnetosphere during that time could produce some of the differences which we observe between flights.

Referring back to Figures 21, 22, and 23, we note an additional feature of the transition time. The rate of type 2 events drops to its nighttime value earlier in the evening and returns to the daytime value later in the morning than does the rate of type 1 events. This

Fig. 25. Latitude and local time of nighttime and daytime count rates for events of type 1. Latitude is defined by $R_c = 14.9 \text{ GV} \cos^4 \lambda$ where R_c is the vertical cutoff based upon the earth's internal field only (36).

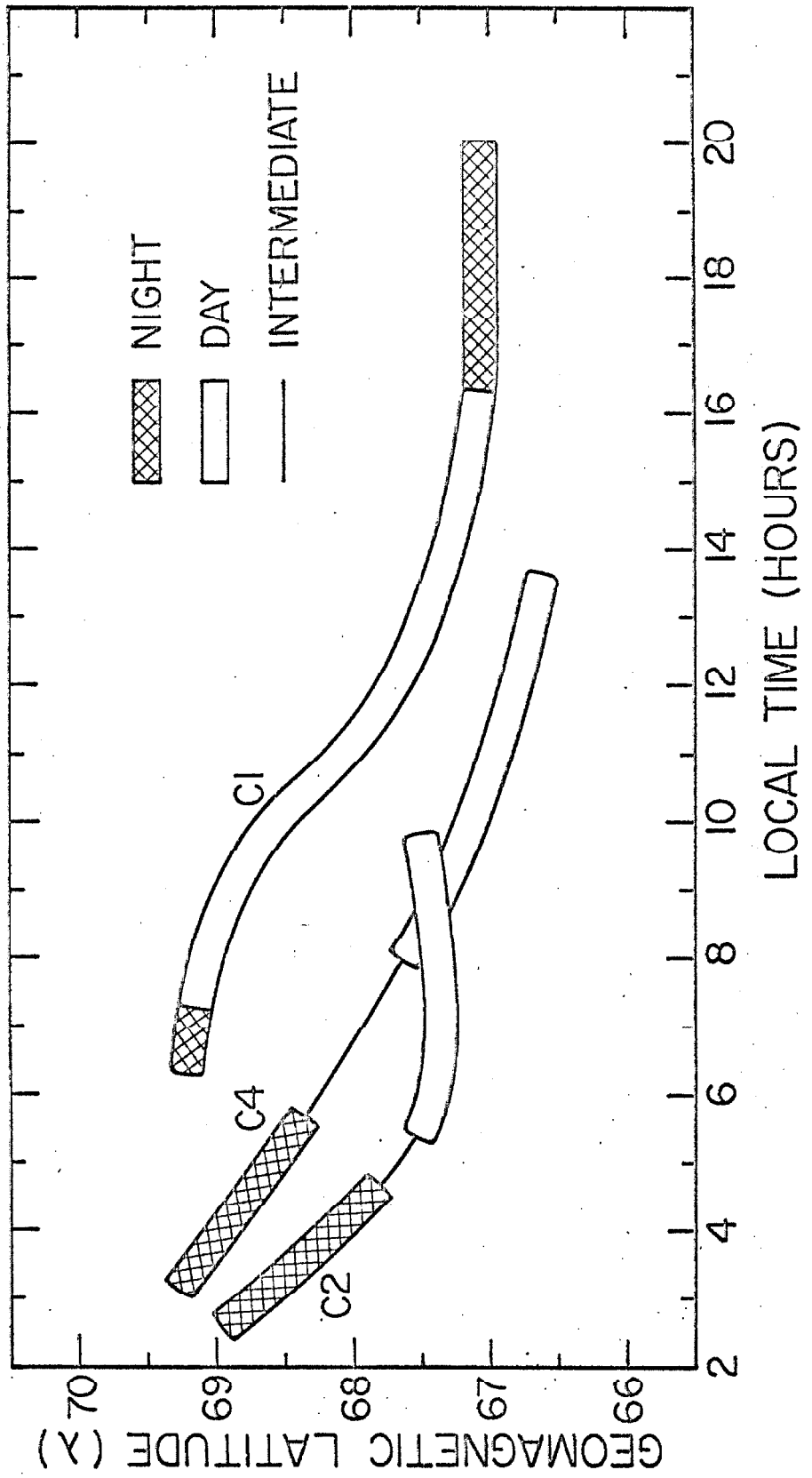
NIGHT
DAY
INTERMEDIATE
C1
C4
C2
GEOMAGNETIC LATITUDE (λ)
70
69
68
67
66
2
4
6
8
10
12
14
16
18
20
LOCAL TIME (HOURS)

Fig. 25

feature indicates that the change in cutoff from below 20 MV to near 90 MV occurs over a period of from one to three hours. Gall et al. (63) have calculated the variation of geomagnetic cutoff with time at 67.8^{o} latitude. As previously noted, their noon and midnight cutoff rigidities do not agree quantitatively with our observations; however, we again have qualitative agreement, because their calculations show that the change in cutoff rigidity occurs gradually over a period of several hours.

C) Primary electrons

1) Background

Our results regarding the primary electrons will have bearing upon the questions of solar modulation and of the origin of the electrons. These questions have been discussed extensively in the literature. (See Part I and references cited therein.) In this section we confine ourselves to a brief description of the published work which directly affects our later discussion.

Solar modulation of cosmic ray protons and alpha particles has been extensively studied. (See review by Webber, reference 23.) At present no model has been worked out to explain fully all features of the time variation of protons and alpha particles; but there is reasonable agreement with the diffusion-convection model, originally proposed by Parker (64). In this model the differential rigidity spectrum $j(R;t)$ observed at the earth at some time, t, is related to the spectrum $j_o(R;t)$ outside the region of solar modulation by

$$\frac{j(R;t)}{j_o(R;t)} = \exp\left[-\frac{\eta(t)}{f(R,\beta)}\right] \qquad (7)$$

where R is the particle rigidity, β is the particle velocity in units of the speed of light, and $\eta(t)$ is a parameter depending upon the solar wind velocity and interplanetary magnetic field irregularities but independent of the properties of the modulated particles. The quantity which has been most extensively measured is the change in $j(R;t)$ with time, during the solar cycle. This change is related to $\Delta\eta$, the change in $\eta(t)$, between two times of observation.

$$\frac{j(R;t_1)}{j(R;t_2)} = \exp\left[-\frac{\Delta\eta}{f(R,\beta)}\right] \tag{8}$$

In the simplest form of the theory,

$$f(R,\beta) = \begin{cases} R\beta & \text{for } R > R_o \\ R_o\beta & \text{for } R < R_o \end{cases} . \tag{9}$$

This model gives agreement with much of the proton and helium data for $R_o \approx 0.5$ GV.

The applicability of this modulation model to electrons is open to question. There is nothing in the theory which distinguishes particles except by their velocity and rigidity; so one would expect that if it fits protons and alpha particles, the theory would also fit electrons. However, the experimental evidence for electrons is, at present, contradictory. For electrons between 0.25 and 1.05 GV, L'Heureux, Meyer, Verma, and Vogt (65) found no modulation from 1960 to 1966; they set an upper limit of 60% on the fractional change of electron intensity during this period. The proton and helium data between 1960 and 1965 (23) fit the diffusion-convection

model with $\Delta\eta \approx 0.8$ GV and $R_o \approx 1$ GV; but modulation with these parameters would produce an increase by near 120% in the electron flux below 1 GV, in disagreement with the results of L'Heureux, et al. This disagreement implies that the modulation of electrons is significantly weaker than that of protons and alpha particles. On the other hand, between 1965 and 1966 Webber (66) claims to find significant electron modulation in the interval from 100 to 2000 MeV, with both electrons and protons satisfying $\Delta\eta = 0.17$ GV, $R_o = 0.5$ GV.

Comparison between our observation in 1967 and those of other observers in previous years may give some indication regarding modulation of electrons. Also, we derive a constraint upon the total modulation of low energy electrons, as described below.

In addition, we compare our observed electron spectrum with the calculated spectrum of galactic secondary electrons (22) - i.e., electrons originating in collisions between cosmic ray nuclei and the interstellar gas. The comparison involves an estimate of the total electron modulation, which is related to η, not merely $\Delta\eta$. Ramaty and Lingenfelter (28) estimate $\eta \approx 0.4$ at solar minimum, 1965. They derive this value by comparing observed fluxes of deuterium and helium-3 with calculated fluxes, assuming that these nuclei originate in the interactions between cosmic ray nuclei and the interstellar gas. Independent estimates of η are derived by comparing the observed electron spectrum at energies $\gtrsim 200$ MeV with the observed non-thermal galactic radio noise. Depending upon what radio data are selected for comparison, values of η near solar minimum of 0 to 0.5 GV (25), 0.65 GV (26), and 0.6 to 0.75 GV (27) have been calculated. Between solar minimum (in 1965) and the time of our observations, we estimate $\Delta\eta \approx 0.3$ GV. (This

value is derived from proton data over a similar period before solar minimum [23].) Thus η at the time of our observations is probably between 0.6 and 1.0 GV. This uncertainty in η gives a corresponding uncertainty in the total modulation. Furthermore, the form of the modulation below several hundred MV is not certain; i.e., the value of R_o in the expression for the total modulation is uncertain; and for low energy electrons a change of R_o from 0.5 GV to 0.3 GV would have about the same effect as a change in η from 0.6 GV to 1.0 GV.

The uncertainty in the total modulation of electrons, especially at energies below a few hundred MeV, makes it difficult to draw quantitative conclusions regarding the electron source at these energies. Our data, however, do provide constraint upon the absolute modulation and the sources.

2) Results

We shall accept the explanation of the diurnal flux variation described above (Section B). For those types of electron events which display a diurnal variation, types 1 and 2, we shall use only the nighttime data. For the events of type 3 and 4, which display no significant diurnal variation, we shall use data gathered over the entire float period of each flight. The observed event rates are listed in Table 8, Section B. We apply the analysis described in Part IV to derive the flux of electrons observed at the detector, including primaries and atmospheric secondaries. The results are listed in lines 2, 3, and 4 of Table 9. The float altitudes of flights C2 and C4 agreed within 0.1 g/cm^2, and the calculated electron fluxes in the two flights are in close agreement. Therefore, the

TABLE 9

PRIMARY ELECTRONS

(Results are derived from the nighttime data of type 1 and type 2 events, and data from the entire float period of type 3 and type 4 events.) (Errors include statistical and systematic uncertainties.) (Fluxes in electrons/m^2 sec sr)

1. Energy interval at detector (MeV)	12 - 50	50 - 100	100 - 350	350 - 1000
2. Total flux at detector. Flight C1	39 ± 12	31 ± 11	38 ± 15	23 ± 11
3. Flight C2	27 ± 10	17 ± 9	25 ± 12	26 ± 15
4. Flight C4	31 ± 10	15 ± 7	20 ± 8	22 ± 13
5. Flights C2 and C4	29 ± 8	16 ± 7	23 ± 10	24 ± 12
6. Atmospheric secondaries at 2 g/cm^2 (C2 & C4)	28 ± 6	23 ± 5	31 ± 6	8 ± 2
7. Primary electrons Flights C2 and C4				16 ± 14
8. Upper limit to primary electrons Flights C2 and C4	20	9	13	(35)
9. Atmospheric secondaries (mean during C1)	41 ± 9	33 ± 7	37 ± 7	10 ± 2
10. Upper limit to primary electrons Flight C1	21	23	20	(31)
11. Energy interval at top of atmosphere(MeV)	17 - 57	57 - 112	112 - 374	374 - 1060

results of these two flights have been combined, yielding the fluxes tabulated in line 5. In Figure 26, we plot the differential energy spectra derived from these data. Also plotted in this figure is the calculated spectrum of atmospheric secondaries at the float altitude of flights C2 and C4.

In line 6 of Table 9 we list the atmospheric secondary fluxes for flights C2 and C4. We note that below 350 MeV our total observed flux is consistent with the flux expected from atmospheric secondaries only; i.e., our results below 350 MeV are consistent with the complete absence of primary electrons. In line 8 we list upper limits to the primary electron fluxes. These limits represent two standard deviations of statistical uncertainty, plus the systematic uncertainty. Similar subtraction of atmospheric secondaries for flight C1, which had a lower average float altitude, are indicated in lines 9 and 10. The last line of Table 9 gives the energy interval at the top of the atmosphere to which the calculated primary fluxes correspond. This adjustment of energy intervals takes into account the energy loss of primary electrons in penetrating 2.1 g/cm^2 of air.

The observed flux of electrons between 50 and 350 MeV appears to be higher on flight C1 than on flights C2 and C4, even after accounting for the difference in atmospheric secondaries. The deviation lies, however, at the edge of the experimental uncertainty. More accurate results would be required to confirm a short term flux variation.

3) Discussion

In Figure 27 we plot, as solid symbols, the differential fluxes derived from our data. Also plotted are the results of other recent

Fig. 26. Differential kinetic energy spectrum of downward-moving electrons above geomagnetic cutoff. Data points indicate total observed electron flux at detector during float. For those types of events displaying a diurnal variation only nighttime data are used. (Vertical error bars indicate combined statistical and systematic uncertainty.)

Circles - flight C1, 2.1 to 3.4 g/cm^2.

Squares - flights C2 and C4, 2.1 g/cm^2.

Solid curve indicates atmospheric secondaries at depth of flights C2 and C4 based upon calculations of Perola and Scarsi (44). Adjustments are included for knock-on electrons and for the difference between the proton flux at the time of our flights and that for which the calculations were made.

Dashed curves indicate ± 20% uncertainty band about the calculated secondary spectrum.

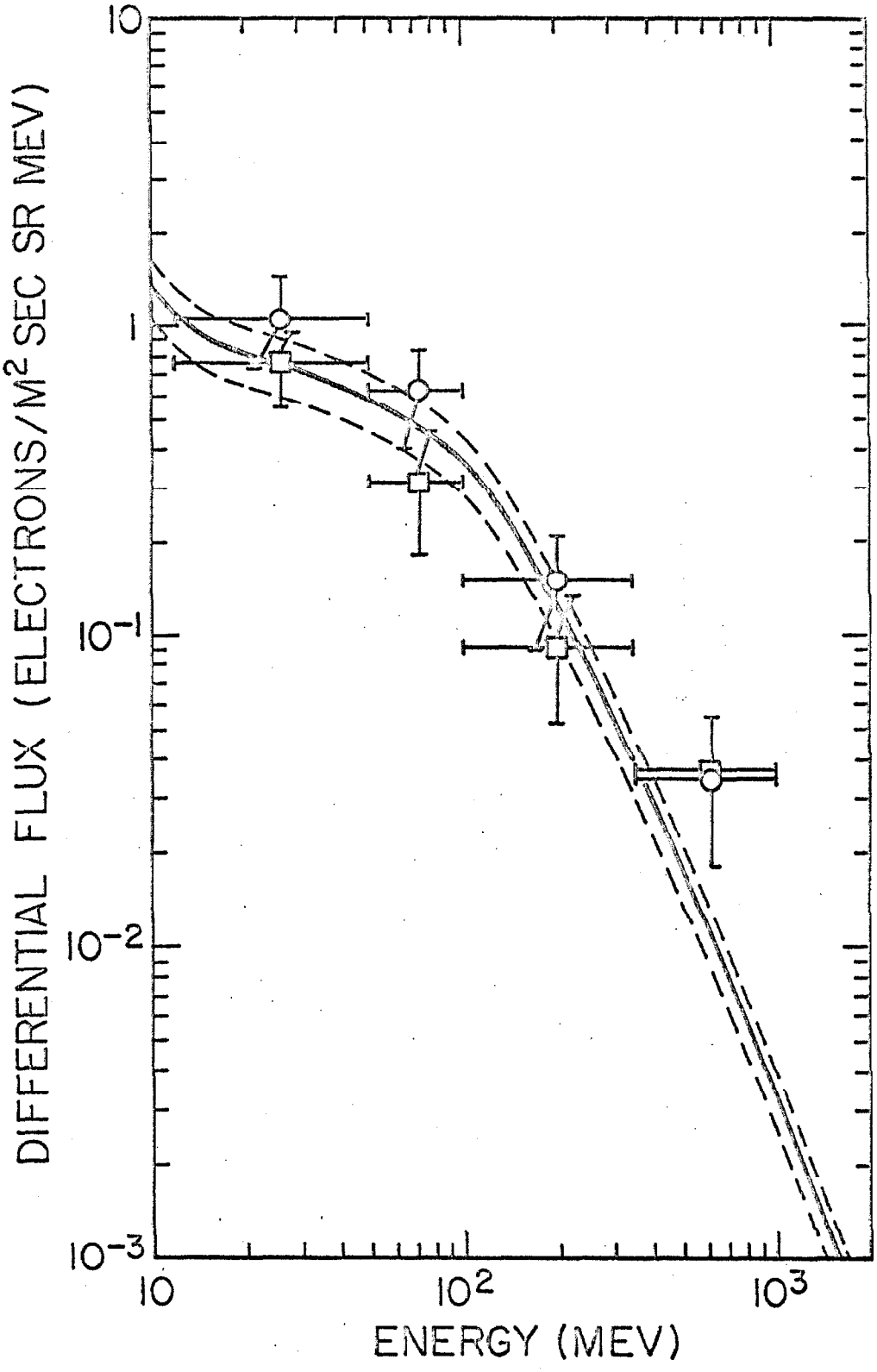
DIFFERENTIAL FLUX (ELECTRONS/M² SEC SR MEV)
10
1
10⁻¹
10⁻²
10⁻³
10
10²
10³
ENERGY (MEV)

Fig. 26

Fig. 27. Differential kinetic energy spectrum of primary electrons.

Solid data points - this experiment, June and July, 1967

Squares - flights C2 and C4
Circles - flight C1 where different from C2 and C4.

Diamonds - Webber, July, 1966, (16).

Crosses - L'Heureux and Meyer, June 1966 (4).

Large rectangle - Jokipii, L'Heureux, and Meyer, June 1966 (29).

Open squares - Fan, Gloeckler, Simpson, and Verma, June 1965 - March 1966 (14).

Open circles - Cline, Ludwig, and McDonald, Jan. 1964 (12).

Open triangles (point up) - Fanselow, 1965 (9).

Open triangles (point down) - Simnet, 1967 (10).

Solid curve - calculated interstellar spectrum of galactic secondary electrons (22).

Dashed curves - solid curve, modulated according to diffusion-convection model, equations 7 and 9.

Curve 1 - $\eta = 0.6$ GV $R_o = 0.5$ GV

Curve 2 - $\eta = 1.0$ GV $R_o = 0.5$ GV

Curve 3 - $\eta = 0.6$ GV $R_o = 0$

Curve 4 - $\eta = 1.0$ GV $R_o = 0$.

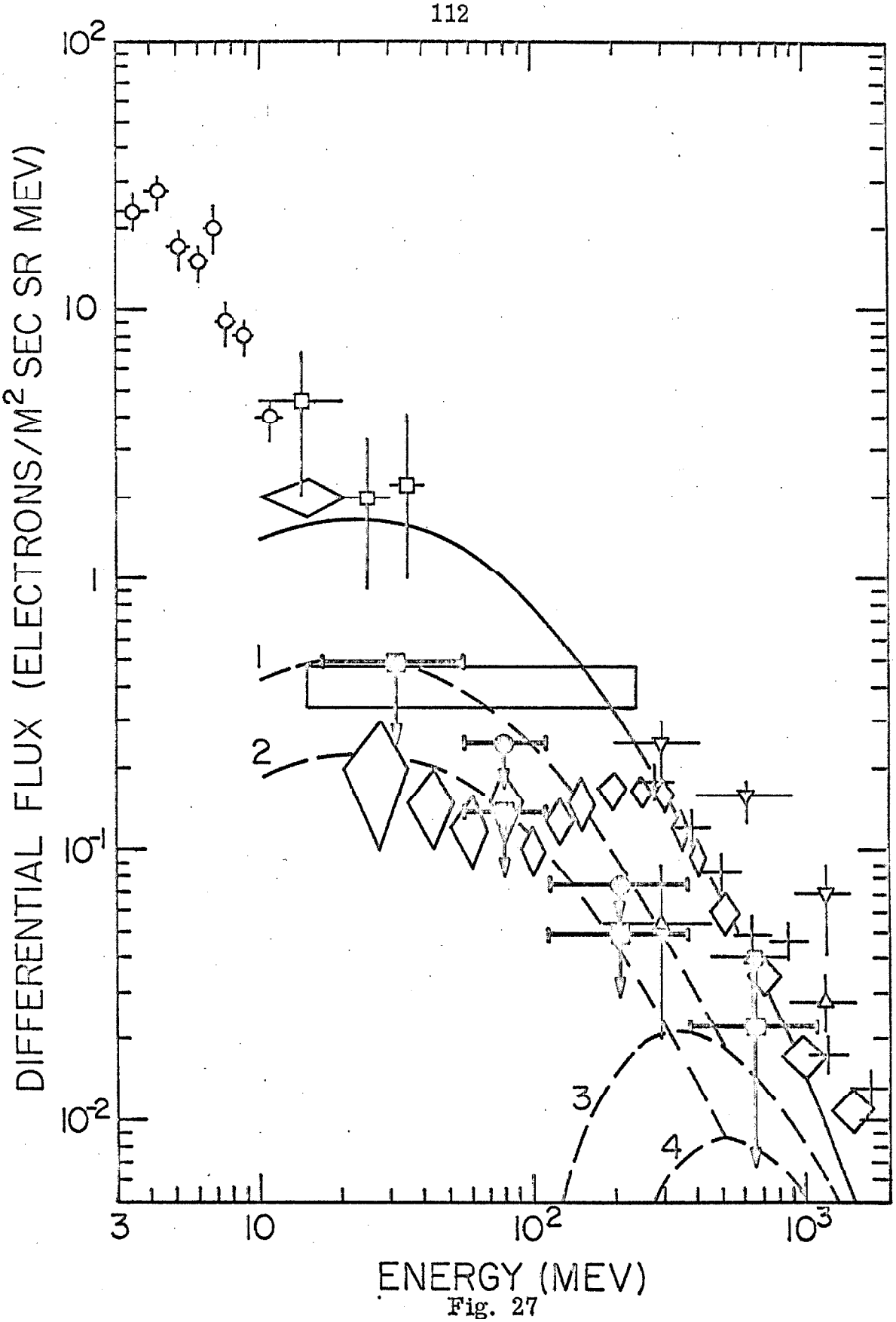
DIFFERENTIAL FLUX (ELECTRONS/M² SEC SR MEV)
ENERGY (MEV)
10²
10
1
10⁻¹
10⁻²
3
10
10²
10³
1
2
3
4

Fig. 27

electron measurements and the calculated spectrum of galactic secondary electrons. In plotting results of other observers, we omit any data point which includes electrons with energy below 110 MeV unless it is derived from nighttime observations only.

Above 100 MeV the flux of primary electrons which we observed in 1967 is significantly lower than the 1966 flux reported by Webber (16) and by L'Heureux and Meyer (4). This difference would indicate significant modulation of electrons between the middle of 1966 and the middle of 1967. Between 112 and 374 MeV, the upper limit to the primary flux of flights C2 and C4 is a factor of 3 below the flux measured by Webber. Between 374 MeV and 1060 MeV, our best estimate of the flux is nearly a factor of 2 below that of Webber and of L'Heureux and Meyer. Our results would be consistent with these other observations if the diffusion-convection model correctly described electron modulation with $\Delta\eta \approx 0.3$ GV from mid-1966 to mid-1967 and $R_o \approx 0.3$ GV. This modulation of electrons is larger than would be expected from observed modulation of protons. (The neutron monitor count rate changed by about 4% between 1966 and 1967. For a similar change in neutron monitor rate prior to the solar minimum of 1965, the change in proton flux [23] fits the diffusion-convection model with $\Delta\eta \approx 0.2$ GV.)

On the other hand, our results are in agreement with Fanselow's results from 1965 (9), while Simnet's results from 1967 are significantly higher than those of any other observer (10). Thus caution is necessary when attempting to draw conclusions about the modulation by comparing results of different observers. It would be preferable to study the modulation with a single detector system over several years to minimize the chance of systematic errors contributing to the apparent modulation.

Figure 27 shows that below 112 MeV our upper limits for the primary flux are consistent with the values reported by Webber. Our

results disagree with those of Jokippi et al., but the difference lies primarily in the correction for atmospheric secondaries. They used the atmospheric secondary corrections calculated by Verma (45) rather than those of Perola and Scarsi (44). As we have discussed in Part IV, Section F, Verma's calculations yield too low a flux of secondary electrons below 100 MeV.

There is, however, a large discrepancy between the flux we observe in the 17 to 57 MeV interval and the flux reported by Fan, Gloeckler, Simpson, and Verma (14). Their best flux estimate between 20 and 40 MeV lies above our upper limit by a factor of four. It is not likely that this difference can be accounted for entirely by solar modulation even though their data were taken a year and a half before ours. Webber's data, taken a few months after theirs, is a factor of ten below their result. The data reported by Fan et al. were taken on an IMP satellite, outside the magnetosphere, so their results are free of atmospheric secondaries and effects of the geomagnetic field. Both Webber's data and ours are derived from nighttime observations with a balloon-borne detector near Fort Churchill. The difference between the satellite data and the balloon data could be explained if the present understanding of the diurnal variation were incorrect, and the nighttime flux were somehow lower than the interplanetary flux. We believe this to be quite unlikely. As pointed out in Section B, the nighttime flux is significantly lower than the splash albedo flux, indicating a lack of return albedo at night. We know of no mechanism by which both return albedo and primaries can be excluded from the observations. The lack of return albedo implies that primary electrons must be able to reach the detector from interplanetary space. The detector with which Fan et al. derive their electron flux was designed to detect low-energy protons and

helium nuclei. Derivation of the electron flux requires subtraction of a large background of events of undetermined origin. It is possible that part of the background is not fully eliminated by their subtraction method.

We turn finally to the implications of our observations below 100 MeV on the question of the origin of the electrons and the absolute solar modulation. The solid curve in Figure 27 displays the interstellar spectrum of galactic secondary electrons calculated by Ramaty and Lingenfelter (22). The calculation requires assumptions about the amount of interstellar material traversed by the cosmic rays and the volume in which the electrons are stored. A similar calculation by Perola, Scarsi, and Sironi (19) indicates that the flux of galactic secondary electrons between 10 and 100 MeV can vary by an order of magnitude as the galactic parameters are varied over range of possible values. In the following discussion we shall accept the Ramaty and Lingenfelter calculations as the best available estimate of the galactic secondaries.

The dashed curves in Figure 27 indicate the spectrum of galactic secondaries near the earth under the assumption of various forms of modulation. The solid curve must be treated as a lower limit to the interstellar electron spectrum because there may be additional electrons from other sources. Since the upper limit to our electron flux lies a factor of three below this curve, we conclude that there must be significant modulation of these low-energy electrons - a reduction in flux by at least a factor of three. If the absolute modulation were proven smaller than this, then our data would imply that some of the galactic parameters used in Ramaty and Lingenfelter's calculation were seriously in error.

If the actual modulation is approximately as indicated by curves 1 or 2 in Figure 27, then the low energy electron flux observed near the earth can be accounted for entirely by galactic secondary electrons. This would contrast with the result at energies $\gtrsim$ 500 MeV, where primary acceleration of electrons clearly dominates (20). At present, however, we cannot eliminate the possibility that the absolute modulation of electrons is significantly stronger than that of curve 2, and the contribution of primary accelerated electrons is significant, even at low energies.

Experiments now being conducted to measure the positron/electron ratio at these energies and to measure the long-term variation of the electron flux will further clarify the mechanism of production and solar modulation of electrons.

VI. CONCLUSIONS

Data gathered in a series of high altitude balloon flights lead to several conclusions regarding cosmic ray electrons.

1) Two published calculations of the flux of atmospheric secondary electrons give contradictory results for electrons with energy $\lesssim$ 100 MeV, although they agree above 200 MeV. We compare these calculations with our observations of the altitude dependence of the low energy electron flux. Our results give good agreement with the calculations of Perola and Scarsi (44) and clear disagreement with those of Verma (45). This determination of the atmospheric secondary flux is important for primary electron measurements because the secondaries account for at least half of the observable electrons below 100 MeV, even at the highest attainable balloon altitudes.

2) In one of the balloon flights we pointed our detector toward the nadir. This flight gave the first direct observation of the splash albedo electrons near Fort Churchill. Knowledge of the electron albedo is of interest for some experiments in which it forms a background which must be subtracted. Also, this direct measurement of the splash albedo is very important for our understanding of the diurnal variation of the low energy electron flux near Fort Churchill.

3) We observed the diurnal variation in the flux of downward-moving electrons at energies $\lesssim$ 100 MeV. Comparison between our observations of the diurnally varying flux and our splash albedo measurements gives strong support to the model which explains the low flux of electrons incident at night as primaries and the higher daytime flux as return albedo. This explanation of the diurnal variation is essential to the final part of the thesis, in which we examine

the flux of primary electrons. Our observations also enable us to set an upper limit of 17 MV on the nighttime cutoff near Fort Churchill and to estimate the daytime cutoff as 70 to 110 MV. Our results are in reasonable agreement with calculations of the cutoffs in a model magnetosphere.

4) Finally, we compare the calculated interstellar flux of galactic secondary electrons with our results for the primary electrons incident on the earth, (i.e., the interplanetary electrons). The fact that the interplanetary electron flux is significantly lower than the calculated interstellar flux at energies $\lesssim$ 100 MeV indicates that either there is significant solar modulation of cosmic ray electrons, or some of the parameters used in the calculation of the galactic secondaries require large modification.

APPENDIX

Proton interactions in the detector

In this appendix we estimate the probability that an interacting proton with energy above the gas Čerenkov counter threshold (16 GeV) will produce at least one secondary particle which triggers a guard counter. We find that at least 90 percent of these interacting protons do trigger a guard counter and so fail to contaminate our electron observation. This result is used in Part IV, Section E1.

We are interested in the probability that a charged secondary particle be emitted from the interaction with sufficient energy to escape from the lead plates and with a sufficiently large angle to the direction of the incident particle that it penetrate a guard counter rather than the counter ΔE2. (See Figure 1 in Part II.) Although most of the material in our detector is lead, data on the secondary products from high energy interactions in lead is not available; so we shall base our estimate upon measurements of the angular and energy distribution of secondary particles from interactions of protons in nuclear emulsions. The tracks of secondary particles observed in emulsion are divided into two categories -- "shower tracks," whose grain density is less than 1.4 times minimum, and "heavy tracks," whose grain density is greater than 1.4 times minimum. In some analyses the heavy tracks are further subdivided as "black" if their range in emulsion is less than 2.7 mm, or "grey" if their range is greater (67). By these definitions, particles producing shower tracks may include protons with energy greater than 375 MeV and pions above 60 MeV. Grey tracks

correspond to protons between 25 and 375 MeV; and black tracks, to protons and alpha particles below 25 MeV/nucleon.

We assume that all shower track particles have sufficient energy to escape the lead stack and ask what fraction of them are emitted at an angle which directs them to a guard counter rather than ΔE2. We assume that all incident protons are travelling along the axis of the detector and that 40 percent of those which interact do so in the center of the first lead plate; and 20 percent, in the center of each of the following lead plates. (See Table 10.) In line 4 of the table we indicate, for each lead plate, the minimum angle, θ_o, which a shower track must make with respect to the direction of the incident proton in order to reach a guard counter. Line 5 gives the fraction of all shower tracks whose angle, θ, with respect to the incident proton direction, is greater than θ_o. We derive these fractions from the angular distribution of shower tracks due to interactions of 28 GeV/c protons as measured by Jain et al. (68). These authors give the angular distribution of shower tracks from events in three categories -- those with N_h (the number of heavy tracks) = 0 or 1, $2 \leq N_h \leq 7$, and $N_h > 7$. The fraction of all interactions with nuclei other than hydrogen falling into each of these categories is 16 percent, 43 percent, and 41 percent, respectively (69). Combining the three angular distributions of Jain et al., weighted according to these fractions, gives the results in line 5 of Table 10. Line 6 lists the fraction of all shower tracks which originate in a given plate and travel in a direction which intersects a guard counter. Summing across this line, we find that 46 percent of all shower tracks penetrate a guard counter. We note that this percentage is a lower limit because we assumed that all incident protons travel along the detector axis. The shower tracks tend to

TABLE 10

FRACTION OF SHOWER TRACK SECONDARIES WHICH STRIKE A GUARD COUNTER

(1)	Lead plate number	1	2	3	4
(2)	Lead plate thickness (g/cm^2)	11.6	5.8	5.8	5.8
(3)	Fraction of interactions which occur in given plate	.4	.2	.2	.2
(4)	Minimum angle for hitting guard counter (θ_o)[a]	20^o	30^o	35^o	50^o
(5)	Fraction of shower tracks with $\theta \geq \theta_o$[a]	.59	.43	.38	.24
(6)	Line 3 x line 5	.24	.09	.08	.05

(a) θ and θ_o are angles between the momenta of the incident particle and a secondary particle.

be collimated toward the direction of the incident particle trajectory, so protons incident off the detector axis would have a higher fraction of shower particles travelling toward a guard counter.

We assume that the directions at which the various shower particles leave an interaction are uncorrelated. (Experimental data have not been published to either support or contradict this assumption; but if we picture the interaction of a proton with the nucleus as a nuclear cascade in which the incident particle and the secondaries make several collisions in passing through the nucleus, then it is likely that no strong correlation exists.) We also assume that the angular distribution used above is independent of the number of shower tracks, N_s. (This assumption is valid for collisions with $N_h > 6$ at 6.2 GeV (70), but no data concerning the variation of angular distribution in collisions with large N_h has been published at higher energies.) Then the probability, $P_s(0, N_s)$, that no shower track penetrate a guard counter on an event with N_s shower tracks, is given by Poisson statistics with mean $0.46\, N_s$,

$$P_s(0, N_s) = \exp(-0.46\, N_s) \tag{10}$$

Jain et al. (68) give the probability $p(N_s)$ that exactly N_s shower tracks be produced by interaction of a 28 GeV/c proton. Then the probability, P_{0s}, that an interacting proton produce no shower particle which penetrates a guard counter is given by

$$P_{0s} = \sum_{N_s} p(N_s)\, P_s(0, N_s) \tag{11}$$

We find P_{0s} = 18 percent, for 28 GeV/c incident protons.

The angular distribution of grey tracks from interactions of 24 GeV protons has been reported by Bognanowicz et al. (67). These authors divide the grey tracks into three groups with grain density or range corresponding to protons of 25 to 50 MeV, 50 to 205 MeV, and 205 to 375 MeV. We assume that protons below 50 MeV do reach a guard counter, regardless of the angle of emission; protons between 50 and 205 MeV reach a guard counter provided they are emitted at sufficiently large angle that, after leaving the lead plate where they were created, their trajectory does not intersect any other lead plate, i.e., $60^{o} < \theta < 120^{o}$; protons above 205 MeV penetrate any lead in their path and strike a guard counter provided they are emitted at angle $\theta > \theta_{o}$, as for shower tracks. Using the angular distributions of reference A1 in this manner, we find that 43 percent of all grey tracks strike a guard counter.

In collisions of 25 GeV protons with silver and bromine nuclei in emulsion, there is a strong correlation between the number of heavy tracks, N_h, and the number of shower tracks, N_s, (71). The mean number of heavy tracks, $\overline{N}_h(N_s)$, for a given number of shower tracks is approximately given by

$$\overline{N}_h(N_s) = 2 + 1.1\, N_s \qquad (12)$$

The mean number of grey tracks is $0.4\, N_h$ (67). Again assuming Poisson statistics and taking $N_g = 0.4\, N_h = 0.4\, \overline{N}_h(N_s)$, we find the probability, $P_g(0, N_s)$, of no grey track penetrating a guard counter on an event with N_s shower tracks as

$$P_g(0, N_s) = \exp[-0.43 N_g] \exp[-0.17(2 + 1.1 N_s)] \quad (13)$$

Finally, the probability, P_0, that no grey track or shower track penetrate a guard counter is

$$P_0 = \sum_{N_s} p(N_s) P_s(0, N_s) P_g(0, N_s) \quad (14)$$

We assume that equation 13 holds at 28 GeV even though it is derived for 24 and 25 GeV protons. Then using $p(N_s)$ from reference 68, we find $P_0 = 7$ percent, for 28 GeV incident protons. Similar calculation for 19.8 GeV incident protons, using $p(N_s)$ from reference 72 gives $P_0 = 11$ percent.

Averaged over the proton energy spectrum above the Čerenkov threshold, we estimate $P_0 \leq 10$ percent. As noted above, we have made assumptions during the derivation which give an upper limit to P_0. In addition, the basic assumption that data from nuclear emulsions can be valid for lead also leads to an upper limit for P_0. Lead nuclei, with about twice as many nucleons as in silver or bromine, are likely to have larger intranuclear cascades and so produce more grey and shower tracks than the lighter nuclei. (For the shower tracks, however, the variation with atomic weight, A, is weak. The mean number of shower tracks $\overline{N}_s$ varies like $A^{0.14 \pm 0.03}$ [71].)

We thus set a lower limit of 90 percent on the fraction of interacting protons above the gas Čerenkov threshold which do trigger a guard counter. A more stringent limit could be set by carrying out extensive numerical integrations, or a Monte Carlo calculation, to

account for the angular distribution of incident protons and the distribution of position of interactions in the detector. We feel that these extensive calculations would not be justified without more accurate experimental data regarding the angular distributions and energy spectra of secondary particles from interactions in lead. Furthermore, the simple calculation above is sufficient to limit the uncertainty in our electron measurement due to proton contamination to a value smaller than the statistical uncertainty.

REFERENCES

1. K. O. Kiepenheuer, Phys. Rev. 79, 738 (1950).
2. P. Meyer and R. Vogt, Phys. Rev. Letters 6, 193 (1961).
3. J. A. Earl, Phys. Rev. Letters 6, 125 (1961).
4. J. L'Heureux and P. Meyer, Can. J. Phys. 46, S892 (1968).
5. J. A. M. Bleeker, J. J. Burger, A. J. M. Deerenberg, A. Scheepmaker, B. N. Swanenburg, and Y. Tanaka, Can. J. Phys. 46, S522 (1968).
6. W. R. Webber and C. Chotkowski, J. Geophys. Res. 72, 2783 (1967).
7. K. C. Anand, R. R. Daniel, and S. A. Stephens, Phys. Rev. Letters 20, 764 (1968).
8. C. J. Bland, G. Boella, G. Degli Antoni, C. Dilworth, L. Scarsi, G. Sironi, B. Agrinier, Y. Koechlin, B. Parlier, and J. Vasseur, Nuovo Cimento 55B, 451 (1968).
9. J. L. Fanselow, Astrophys. J. 152, 783 (1968).
10. G. M. Simnett, Goddard Space Flight Center Preprint X-611-68-108, (1968).
11. J. L'Heureux, Astrophys. J. 148, 399 (1967).
12. T. L. Cline, G. H. Ludwig, and F. B. McDonald, Phys. Rev. Letters 13, 786 (1964).
13. T. L. Cline and F. B. McDonald, Can. J. Phys. 46, S761 (1968).

14. C. Y. Fan, G. Gloeckler, J. A. Simpson, S. D. Verma, Astrophys. J. 151, 737 (1968).

15. M. H. Israel and R. E. Vogt, Phys. Rev. Letters 20, 1053 (1968).

16. W. R. Webber, J. Geophys. Res. 73, 4905 (1968).

17. V. L. Ginzburg and S. I. Syrovatski, The Origin of Cosmic Rays (MacMillan Co., New York, 1964), pp. 340-352.

18. R. Ramaty and R. E. Lingenfelter, J. Geophys. Res. 71, 3687 (1966).

19. G. C. Perola, L. Scarsi, G. Sironi, Nuovo Cimento 52B, 455 (1967), and 53B, 459 (1968).

20. R. C. Hartman, R. H. Hildebrand, and P. Meyer, J. Geophys. Res. 70, 2713 (1965).

21. R. C. Hartman, Astrophys. J. 150, 371 (1967).

22. R. Ramaty and R. E. Lingenfelter, Phys. Rev. Letters 20, 120 (1968).

23. W. R. Webber, in Proceedings of the Tenth International Conference on Cosmic Rays, Part A, ed. by J. R. Prescott (University of Calgary, Calgary, Canada, 1967), pp. 146-193.

24. J. J. O'Gallagher, Astrophys. J. 150, 675 (1967).

25. S. D. Verma, Astrophys. J. 152, 537 (1968).

26. K. C. Anand, R. R. Daniel, S. A. Stephens, Nature 217, 25 (1968).

27. W. R. Webber, University of Adelaide preprint ADP 43, (1968).

28. R. Ramaty and R. E. Lingenfelter, Can. J. Phys. 46, S627 (1968).

29. J. R. Jokipii, J. L'Heureux, and P. Meyer, J. Geophys. Res. 72, 4375 (1967).

30. E. C. Stone, J. Geophys. Res. 69, 3577 (1964).

31. G. A. Paulikas, J. B. Blake, and S. C. Freden, J. Geophys. Res. 73, 87 (1968).

32. T. Murayama, Planet. Space Sci. 15, 1169 (1967).

33. P. S. Frier and C. J. Waddington, J. Geophys. Res. 70, 5753 (1965).

34. W. Galbraith and W. S. E. Williams, ed., High Energy and Nuclear Physics Data Handbook (Rutherford Lab., Chilton, England 1964) p. VI-11.

35. J. V. Jelley, Cerenkov Radiation (Pergammon Press, New York, 1958), pp. 5, 22.

36. M. A. Shea, D. F. Smart, and J. R. McCall, Can. J. Phys. 46, S1098 (1968).

37. J. V. Lincoln, J. Geophys. Res. 73, 3094 (1968).

38. J. A. Lockwood, Univ. of New Hampshire, private communication.

39. Environmental Data Service, ESSA, Solar and Geophysical Data, IER-FB-282, pp. 158-169 (1968).

40. B. Rossi, High Energy Particles, (Prentice-Hall, Englewood Cliffs, N. J., 1952), pp. 29-35.

41. W. R. Webber, in Proceedings of the Ninth International Conference on Cosmic Rays, ed. by A. C. Strickland (Institute of Physics and the Physical Society, London, 1965) Vol I, p. 351.

42. R. W. Williams, Rev. Mod. Phys. 36, 815 (1964).

43. F. B. McDonald and W. R. Webber, Phys. Rev. 115, 194 (1959).

44. G. C. Perola and L. Scarsi, Nuovo Cimento 46, 718 (1966).

45. S. D. Verma, Proc. Indian Acad. Sci. 66, 125 (1967).

46. K.-P. Beuermann, to be published, 1968.

47. B. Rossi, op. cit., Chapter 5.

48. A. H. Rosenfeld, ed., Data Booklet on High Energy Physics (UCRL, Berkeley, 1968), p. 22.

49. C. J. Bland in Space Research V ed. by D. G. King-Hale, (North Holland Publishing Co., Amsterdam, 1965), 618.

50. S. B. Treiman, Phys. Rev. 91, 957 (1953).

51. S. D. Verma, J. Geophys. Res. 72, 915 (1967).

52. J. W. Schmoker and J. A. Earl, Phys. Rev. 138, B300 (1965).

53. C. L. Deney, M. F. Kaplon, and P. W. Lommen, Bull. Am. Phys. Soc. 13, 63 (1968).

54. M. J. Berger and S. M. Seltzer, Tables of Energy Losses and Ranges of Electrons and Positrons (NASA SP-3012, Washington, D. C., 1964), 125.

55. W. R. Webber, in Handbuch der Physik, Vol. 46/2, ed. by K. Sitte (Springer, Verlag, Berlin, 1967), 190, 191.

56. N. F. Ness in Solar-Terrestrial Physics, ed. by J. W. King and W. S. Newman, (Academic Press, London, 1967) pp. 57-89.

57. D. J. Williams and G. D. Mead, J. Geophys. Res. 70, 3017 (1965).

58. F. C. Michel, Planet. Space Sci. 13, 753 (1965).

59. J. W. Dungey, Phys. Rev. Letters 6, 47 (1961).

60. S. M. Krimigis and J. A. Van Allen, J. Geophys. Res. 72, 4471 (1967).

61. G. C. Reid and H. H. Sauer, J. Geophys. Res. 72, 197 (1967).

62. H. E. Taylor, J. Geophys. Res. 72, 1593 (1967).

63. R. Gall, J. Jimenez and L. Camacho, J. Geophys. Res. 73, 1593 (1968).

64. E. N. Parker, Phys. Rev. 110, 1445 (1958).

65. J. L'Heureux, P. Meyer, S. D. Verma and R. Vogt, Can. J. Phys. 46, S896 (1968).

66. W. R. Webber, J. Geophys. Res. 72, 5949 (1967).

67. J. Bogdanowicz, P. Ciok, Z. Galster, T. Saniewska, and P. Zielinski, Nucl. Phys. 40, 270 (1963).

68. P. L. Jain, H. C. Glahe, G. N. Srivastava, and P. D. Bharadwaj, Nuovo Cimento 21, 859 (1961).

69. G. Cvijanovich, et al., Nuovo Cimento 20, 1012 (1961).

70. H. Winzeler, B. Klaiber, W. Koch, M. Nikolic, C. M. Schneeberger, Nuovo Cimento 17, 8 (1960).

71. H. Meyer, M. W. Teucher, and E. Lohrmann, Nuovo Cimento 28, 1399 (1963).

72. W. Enge, Z. Physik 185, 456 (1965).